



Wir schaffen Wissen – heute für morgen

Fundamentals and Applications of X-Ray Diffraction

With emphasis on Powder X-ray Diffraction

Dr. Marco Taddei (marco.taddei@psi.ch)

Characterization of Catalysts and Surfaces (529-0611-00L) – Prof. Jeroen A. van Bokhoven

Part 1: Fundamentals

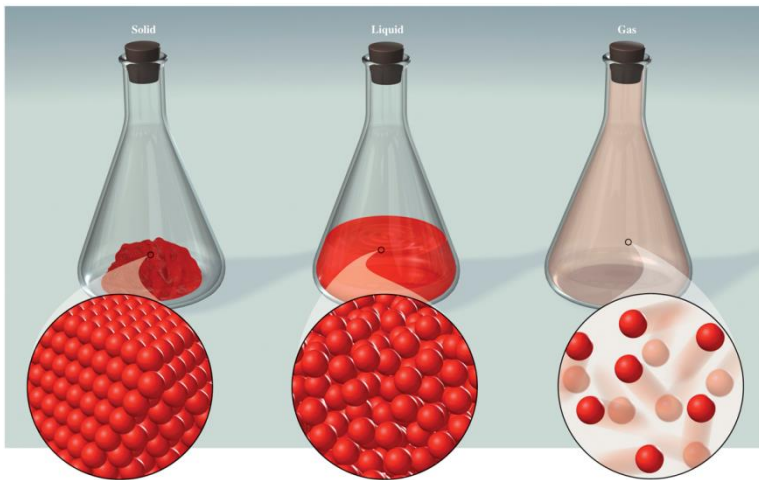
- Fundamentals of Crystallography
- Fundamentals of X-Ray Diffraction
- Experimental Overview
- Diffraction by Polycrystalline Solids

Part 2: Applications in Heterogeneous Catalysis

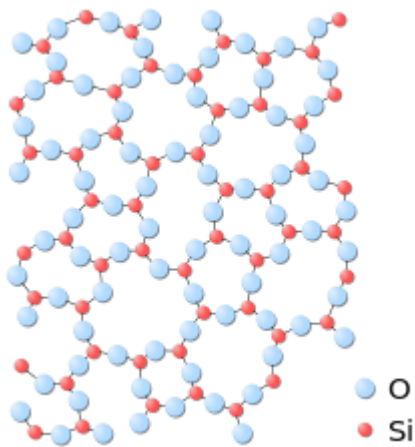
- Selected Examples

Part 1: Fundamentals

Fundamentals of Crystallography



Isotropic solids



Silicon and oxygen atoms in glass are randomly positioned. Amorphous materials can be considered as solids with liquid-like structure.

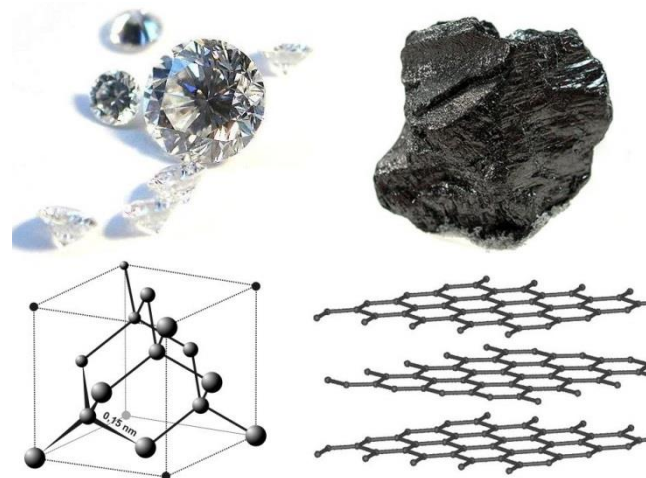
State of matter	Fixed volume	Fixed shape	Order	Properties
Gas	No	No	None	Isotropic ^a
Liquid	Yes	No	Short-range ^b	Isotropic
Solid (amorphous)	Yes	Yes	Short-range ^b	Isotropic
Solid (crystalline)	Yes	Yes	Long-range ^b	Anisotropic ^c

^a A system has same properties in all directions.

^b Short-range order is over a few atoms. Long-range order extends over $\sim 10^3$ to $\sim 10^{20}$ atoms.

^c A system has different properties in different directions.

Anisotropic solids



Diamond has a cleavage plane and is therefore more fragile in some orientations than others.

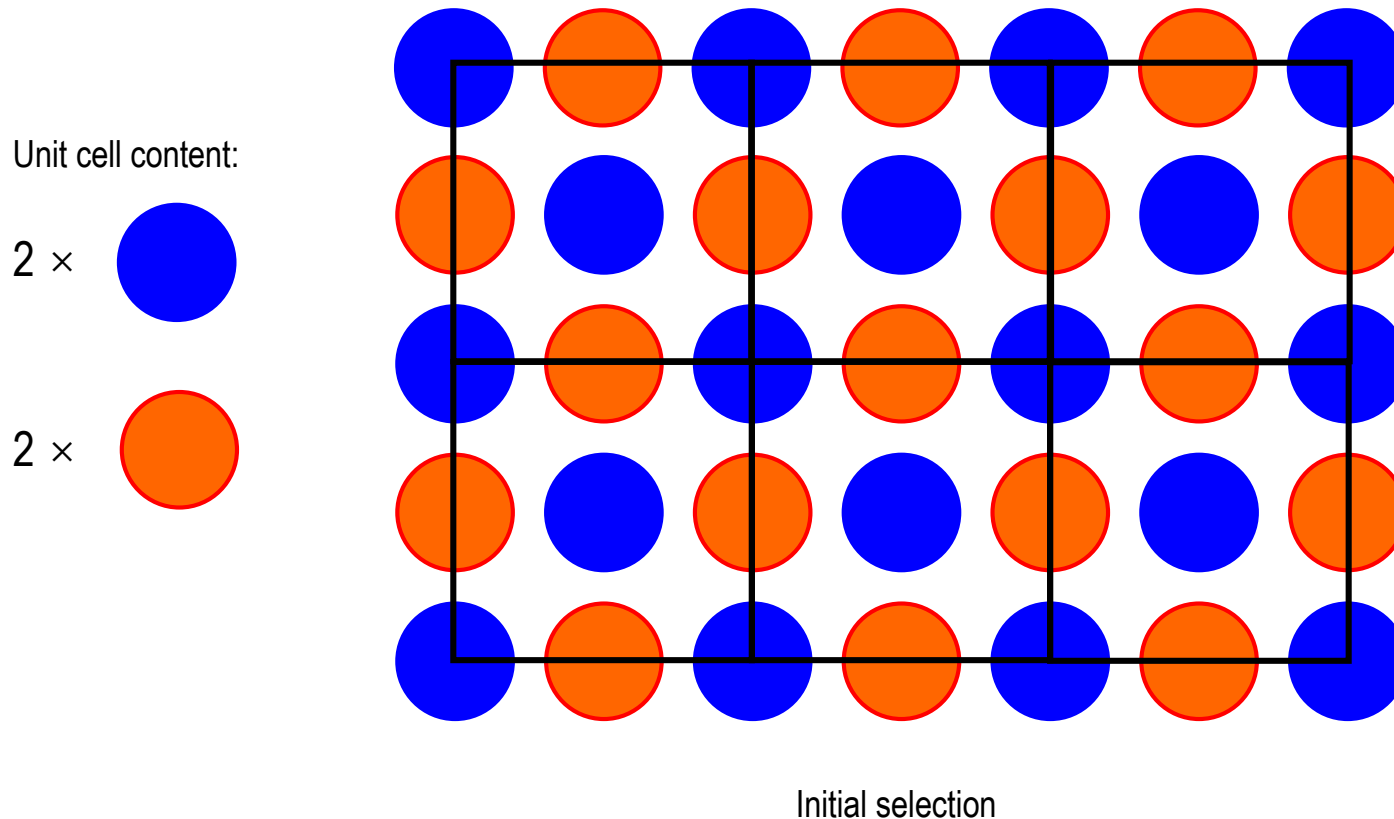
Graphite is a good electron conductor along the layers and an insulator in the direction perpendicular to the layers.

A crystal is a solid where the atoms form a periodic arrangement. Periodic structure of an ideal crystal is best described by a **lattice**.

The smallest repetitive unit in a lattice is termed **unit cell**.

The crystal structure generates from **translation** of the unit cell in one, two, or three dimensions.

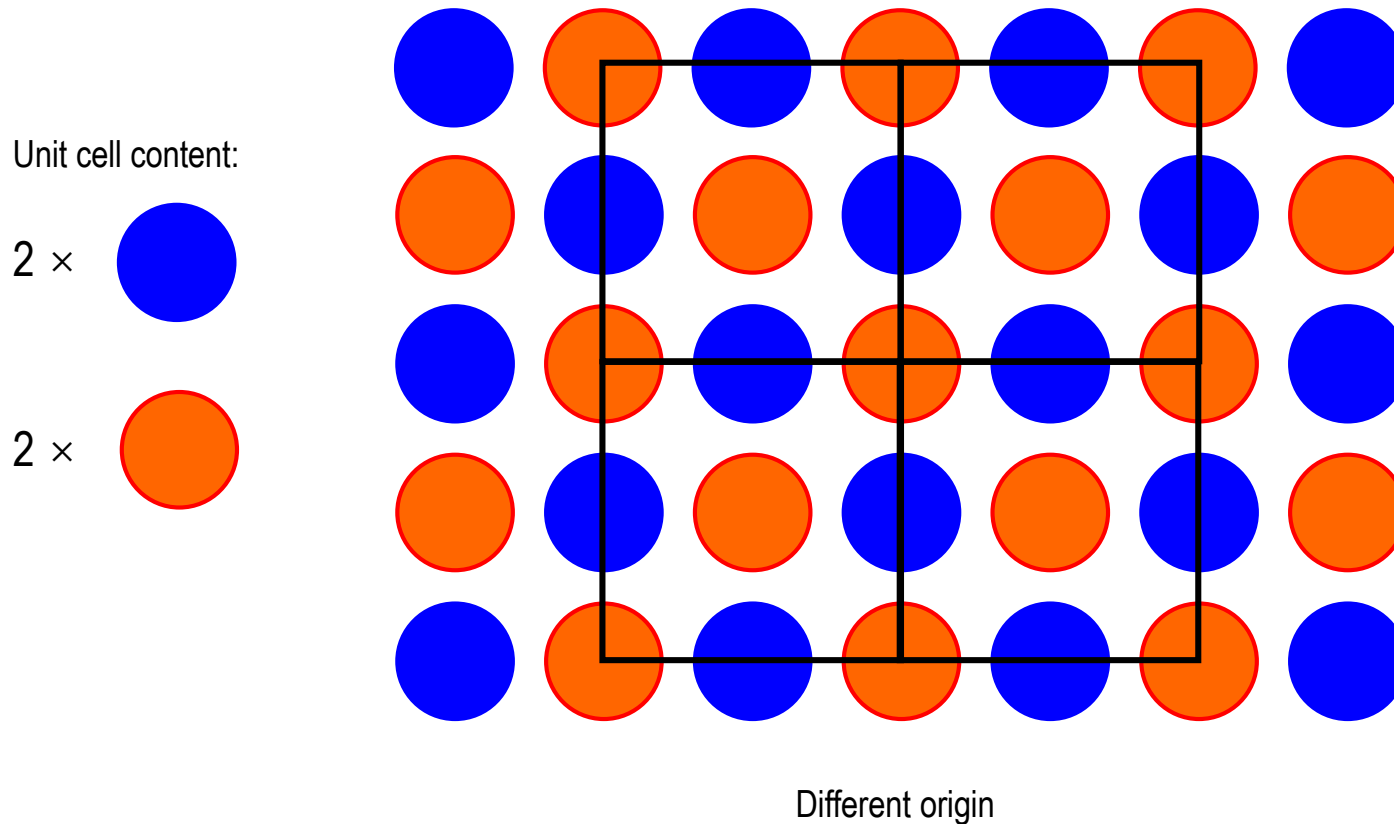
As long as the crystal structure is correctly described the selection of the unit cell is **arbitrary**.



A crystal is a solid where the atoms form a periodic arrangement. Periodic structure of an ideal crystal is best described by a lattice. The smallest repetitive unit in a lattice is termed **unit cell**.

The crystal structure generates from **translation** of the unit cell in one, two, or three dimensions.

As long as the crystal structure is correctly described the selection of the unit cell is **arbitrary**.

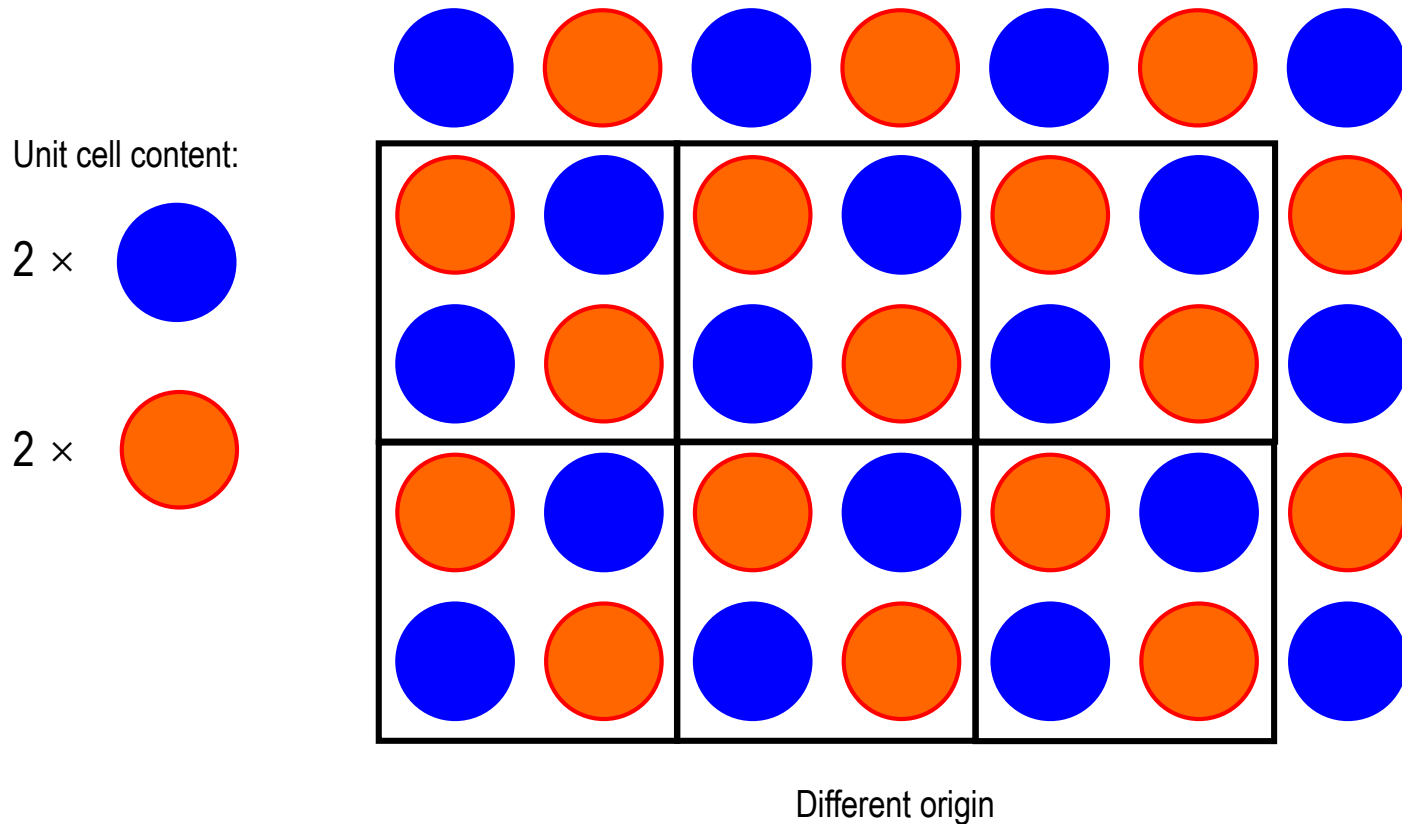


Fundamentals of Crystallography

A crystal is a solid where the atoms form a periodic arrangement. Periodic structure of an ideal crystal is best described by a lattice. The smallest repetitive unit in a lattice is termed **unit cell**.

The crystal structure generates from **translation** of the unit cell in one, two, or three dimensions.

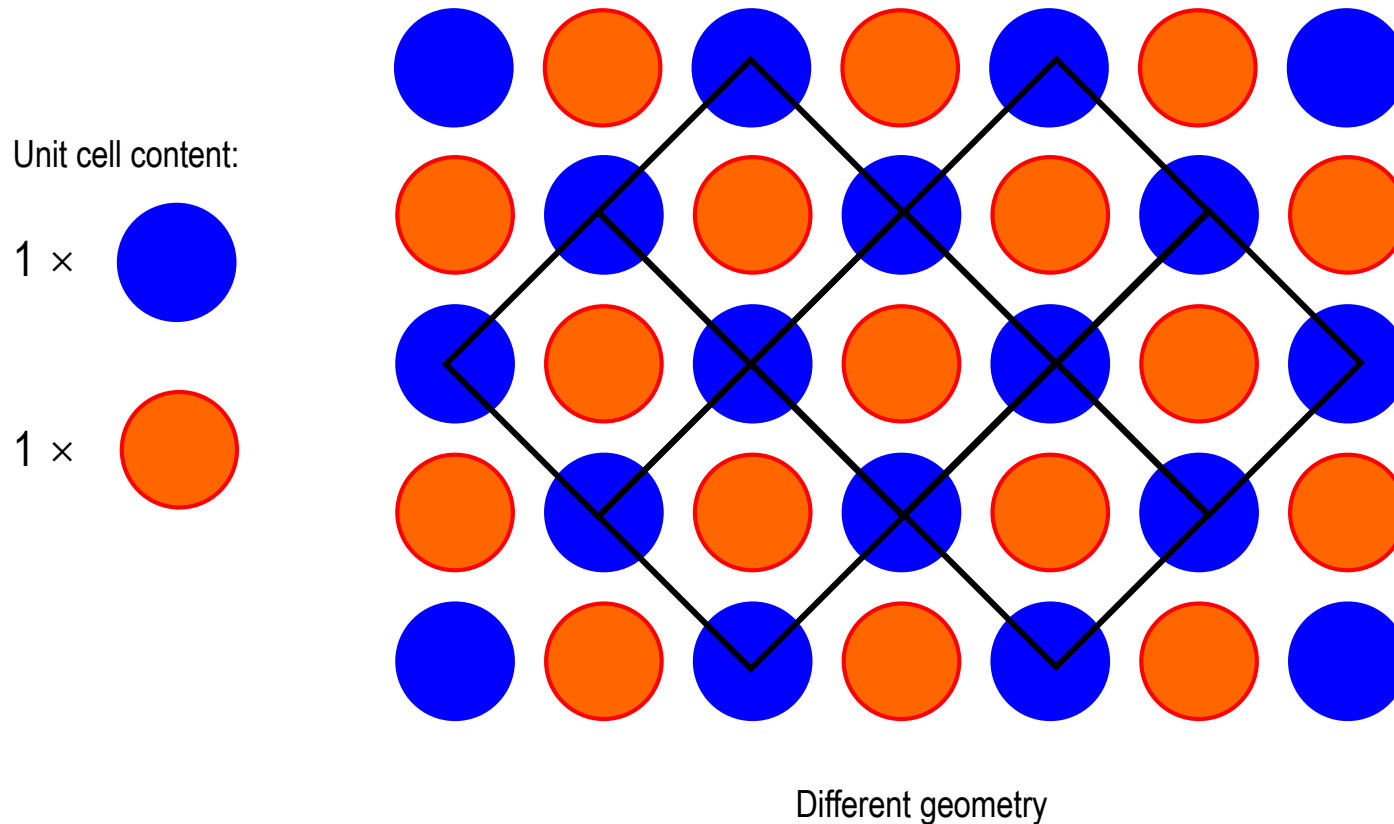
As long as the crystal structure is correctly described the selection of the unit cell is **arbitrary**.



A crystal is a solid where the atoms form a periodic arrangement. Periodic structure of an ideal crystal is best described by a lattice. The smallest repetitive unit in a lattice is termed **unit cell**.

The crystal structure generates from **translation** of the unit cell in one, two, or three dimensions.

As long as the crystal structure is correctly described the selection of the unit cell is **arbitrary**.

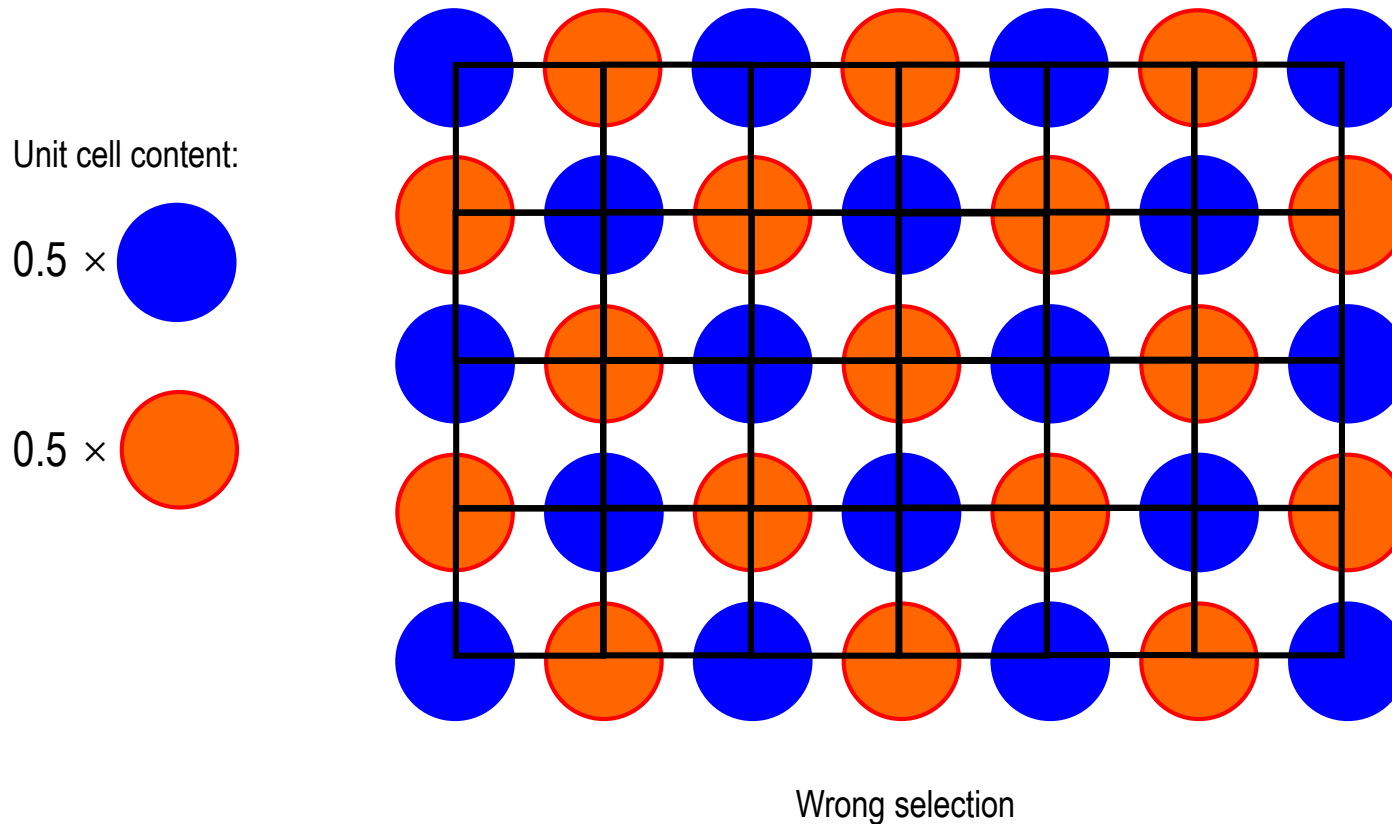


Fundamentals of Crystallography

A crystal is a solid where the atoms form a periodic arrangement. Periodic structure of an ideal crystal is best described by a lattice. The smallest repetitive unit in a lattice is termed **unit cell**.

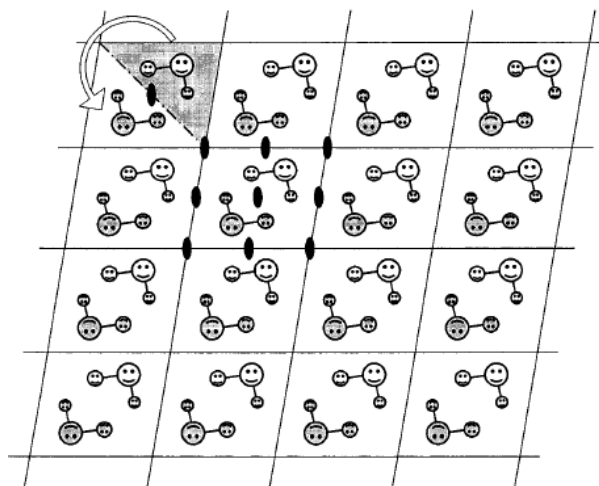
The crystal structure generates from **translation** of the unit cell in one, two, or three dimensions.

As long as the crystal structure is correctly described the selection of the unit cell is **arbitrary**.



Usually, unit cells contain more than one molecule or group of atoms that are converted into each other by simple geometrical transformations, called **symmetry operations**.

The independent part of the cell is called **asymmetric unit**.

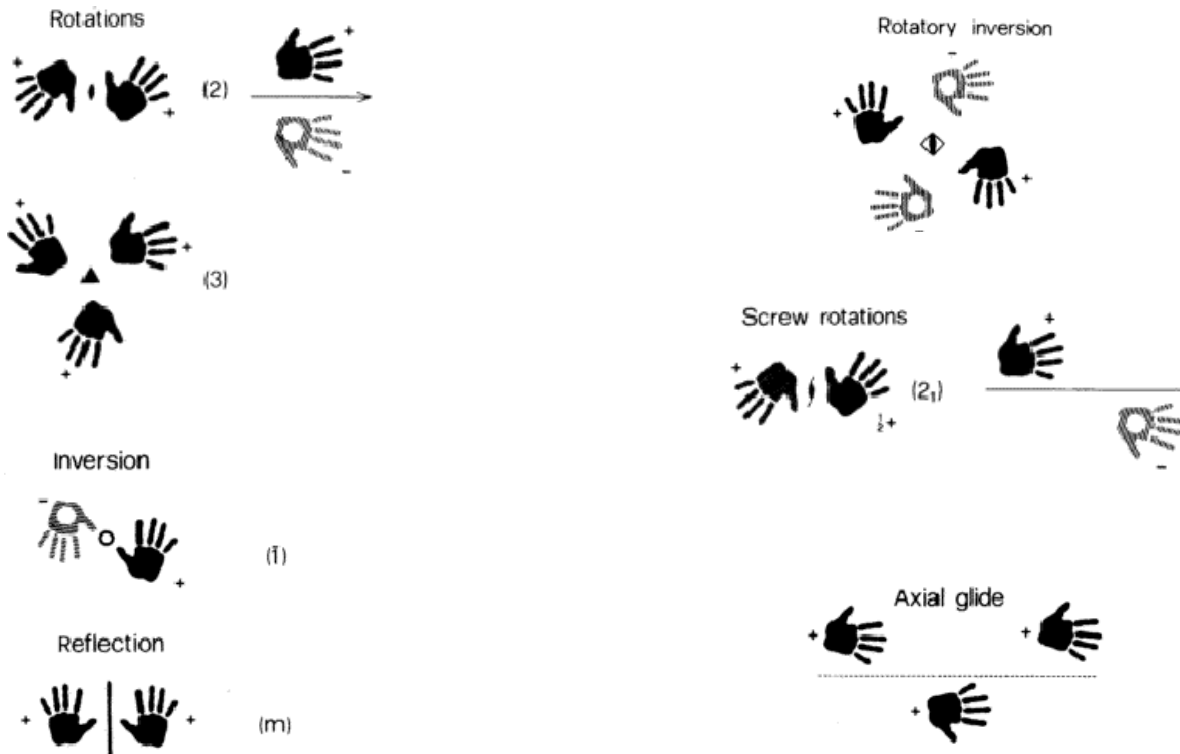


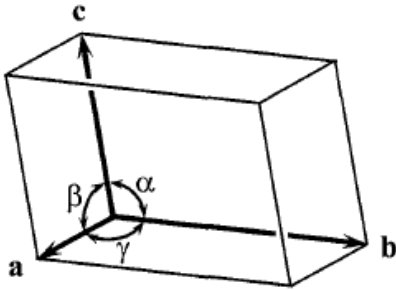
The positions of the atoms constituting the asymmetric unit cell must be defined, while those of all of the other atoms in the unit cell can be derived by transforming the asymmetric unit by means of symmetry operations.

A unit cell can contain from one up to 192 asymmetric units, depending on the number and type of symmetry operations existing in it.

There are four types of simple symmetry operations (elements): **rotation** (axis), **inversion** (center), **reflection** (mirror plane), and **translation** (vector).

Simple symmetry elements can be combined to create new complex elements, such as **inversion axis** (rotation + inversion), **screw axis** (rotation + translation), **glide plane** (reflection + translation).





The shape of a 3D unit cell is defined by three non-coplanar vectors, meaning that there are six scalar quantities to be taken into account, termed **lattice parameters**: a , b , c , α , β , γ .

There are seven possible combinations of lattice parameters, which define just as many **crystal classes**.

Crystal class	Axis system
Cubic	$a = b = c, \alpha = \beta = \gamma = 90^\circ$
Tetragonal	$a = b \neq c, \alpha = \beta = \gamma = 90^\circ$
Hexagonal	$a = b \neq c, \alpha = \beta = 90^\circ, \gamma = 120^\circ$
Rhombohedral	$a = b = c, \alpha = \beta = \gamma \neq 90^\circ$
Orthorhombic	$a \neq b \neq c, \alpha = \beta = \gamma = 90^\circ$
Monoclinic	$a \neq b \neq c, \alpha = \gamma = 90^\circ, \beta \neq 90^\circ$
Triclinic	$a \neq b \neq c, \alpha \neq \beta \neq \gamma \neq 90^\circ$



Decreasing symmetry

Inside every crystal class, a various number of possible crystallographic **space groups** can be identified, which feature different combinations of symmetry operations.

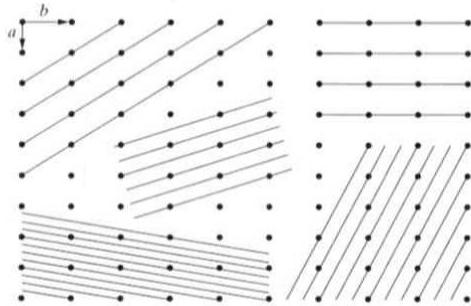
There are 230 possible space groups, unevenly distributed among the seven crystal classes.

36 Cubic, 68 Tetragonal, 27 Hexagonal, 25 Trigonal (7 Rhombohedral, 18 Hexagonal), 59 Orthorhombic, 13 Monoclinic, 2 Triclinic

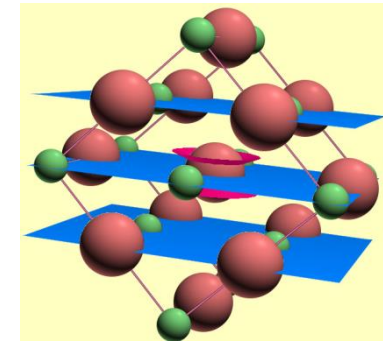
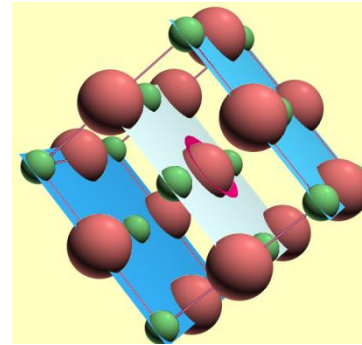
Fundamentals of Crystallography

Inside a crystal lattice, sets of so-called **crystallographic planes** intersecting all lattice points can be identified, which are parallel to each other and equally spaced.

The distance between two adjacent planes is termed **d spacing**.



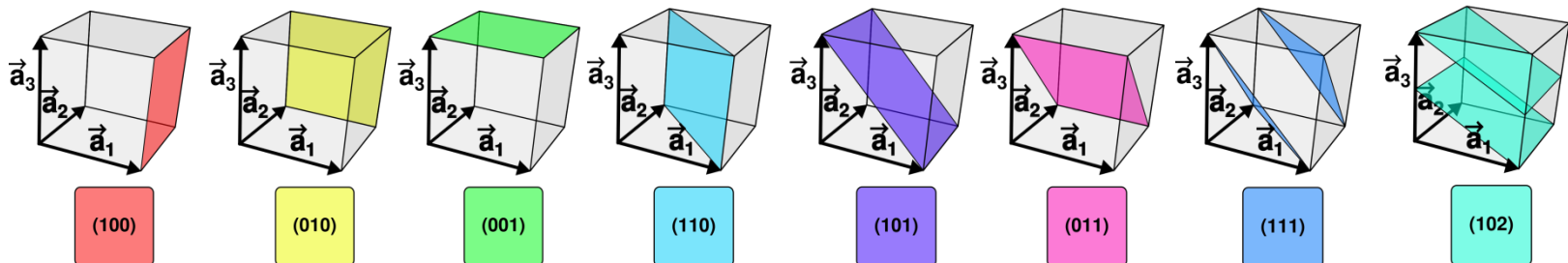
2D lattice



3D lattice

Different sets of crystallographic planes are identified using a set of three integer indices ***h, k, l***, named **Miller indices**. When referring to a particular plane, the three indices are enclosed in parentheses: (hkl) .

Miller indices indicate that the planes that belong to the family (hkl) divide lattice vectors a, b, c into h, k, l equal parts, respectively.

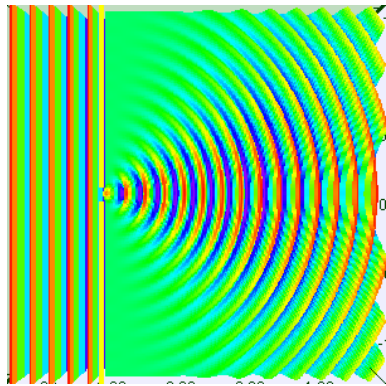
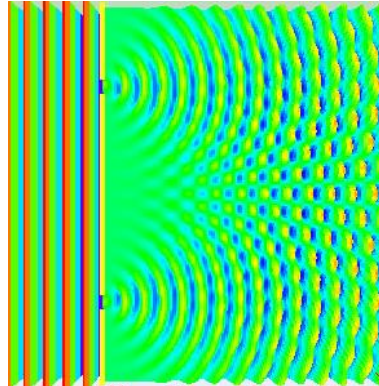
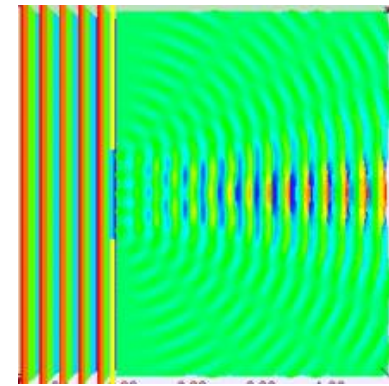


Highlights

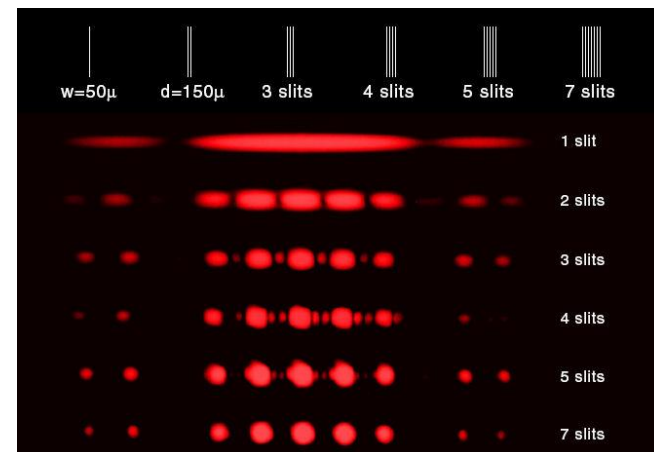
- Crystalline solids are characterized by long-range order
- The structure of a crystal can be represented as a lattice, where the unit cell is the smallest repetitive unit subject to purely translational symmetry
- Inside the unit cell a number of symmetry operations exist, which act on the asymmetric unit generating crystallographically equivalent atoms or molecules
- There are seven crystal classes, each subdivided into various space groups
- The crystal structure can be described by means of sets of lattice planes intersecting all the lattice points, which are identified by Miller indices

Fundamentals of X-Ray Diffraction

Diffraction is an **elastic scattering** phenomenon occurring when a **plane wave** interacts with an obstacle or a slit having size comparable to its wavelength (λ). The scattered **spherical wave** has the same λ of the original one. Varying the size of the obstacle or slit, or their number, the same wave will be diffracted in different ways, as a result of different interference effects.

Slit size = λ Slit size = λ Slit size = 5λ

When a wave encounters an entire array of identical, equally-spaced slits, called a **diffraction grating**, the bright fringes, which come from constructive interference of the light waves from different slits, are found at the same angles they are found if there are only two slits, but the pattern is much sharper.



Fundamentals of X-Ray Diffraction

The periodic lattice found in crystalline structures may act as a diffraction grating for an electromagnetic radiation with wavelength of the same order of magnitude as the repetitive distance between the scattering objects of the lattice, i.e. crystallographic planes.

This means that the wavelength should be in the same range as the d spacing between adjacent planes belonging to the same series, that is, in the order of Å. **X-rays**, having $\lambda = 0.01\text{-}100$ Å, fulfill this criterion.

X-rays interact with the **electron cloud** surrounding an atom and are scattered in all the directions, as a consequence an atom can be considered as a single slit of a diffraction grating. The **electron density** of many atoms constituting a single crystallographic plane can also be considered as a single scattering object.

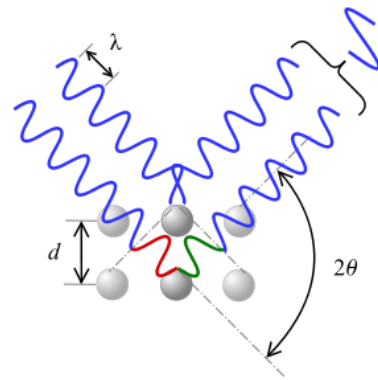
As a consequence, a series of crystallographic planes separated by a constant d spacing can be considered as a diffraction grating. Since a crystal structure features many different series of crystallographic planes, it can be considered as being constituted of many diffraction gratings, each providing its peculiar diffraction effect.

Every set of planes will have its own conditions for producing constructive interference, determined by the **Bragg's law**:

$$n \lambda = 2 d \sin\theta$$

Where n = integer value, λ = X-ray wavelength, d = distance between lattice planes, θ = angle of incidence of the radiation on the lattice plane.

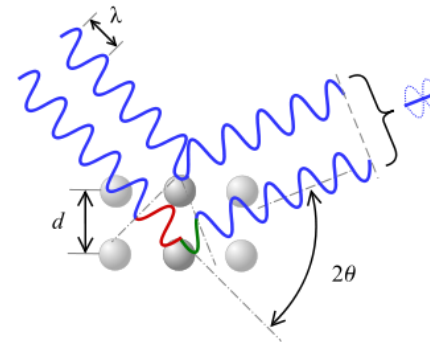
If the wavelength is kept constant, a series of crystallographic planes separated by a given d spacing produces constructive interference only if the incident radiation interacts with it at a particular θ angle.



In phase waves



Constructive interference



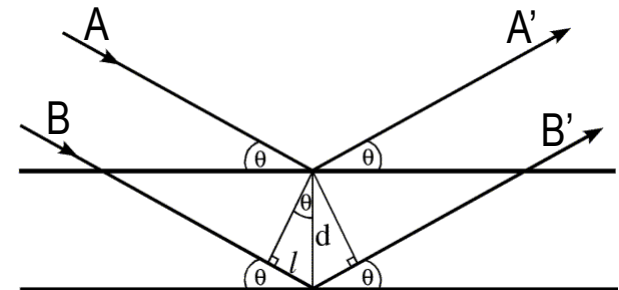
Out of phase waves



Destructive interference

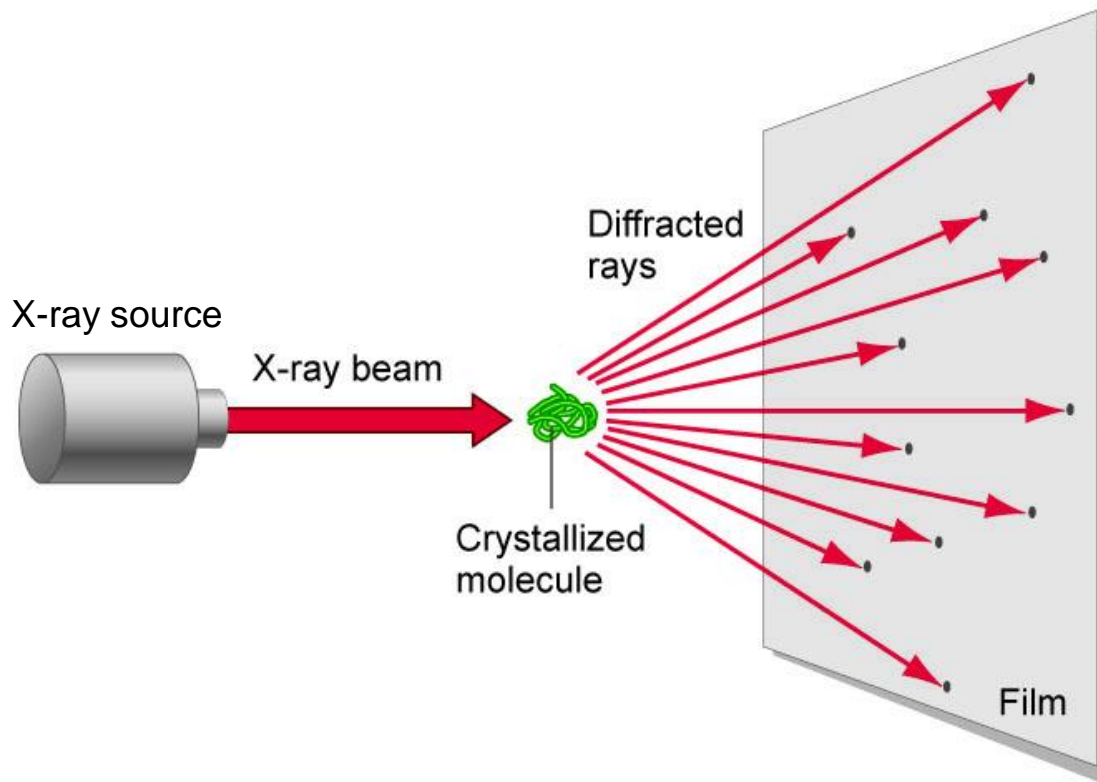
Derivation of Bragg's law

In order to have constructive interference, two incident waves **A** and **B**, hitting at the same angle θ two adjacent lattice planes separated by a distance **d**, must produce two in phase scattered waves **A'** and **B'**. To fulfill this condition, the difference in path length between the waves, **2l**, must be equal to an integer multiple **n** of the wavelength λ . According to trigonometric rules, **l** can be expressed as **d sin θ** .



Fundamentals of X-Ray Diffraction

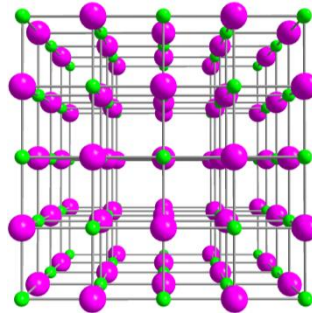
In a diffraction experiment a source of X-rays generates a beam with a particular wavelength (see slides 30 and 31) interacts with the periodic structure of a crystalline sample, generating a number of diffracted rays which are collected by a X-ray detector (see slides 34 and 35).



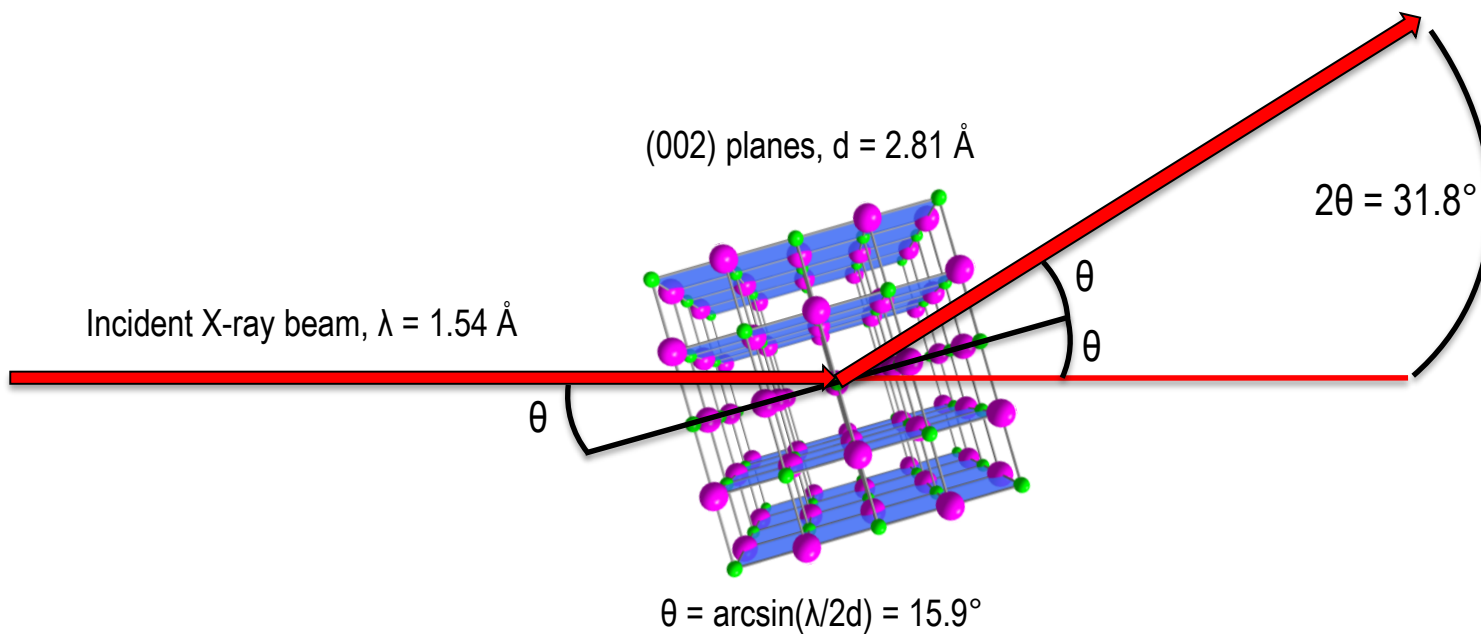
Incident X-ray beam, $\lambda = 1.54 \text{ \AA}$



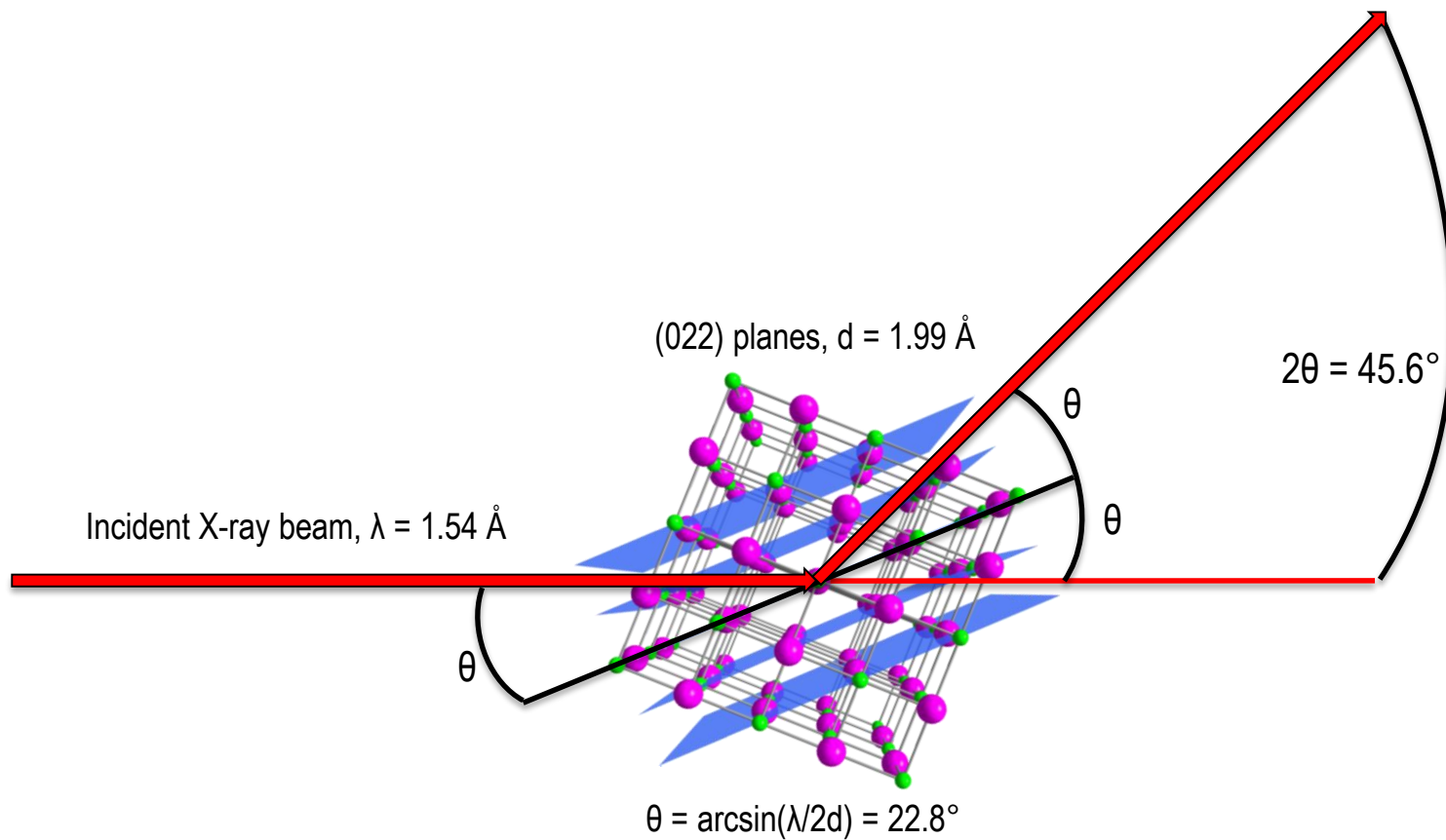
NaCl crystal



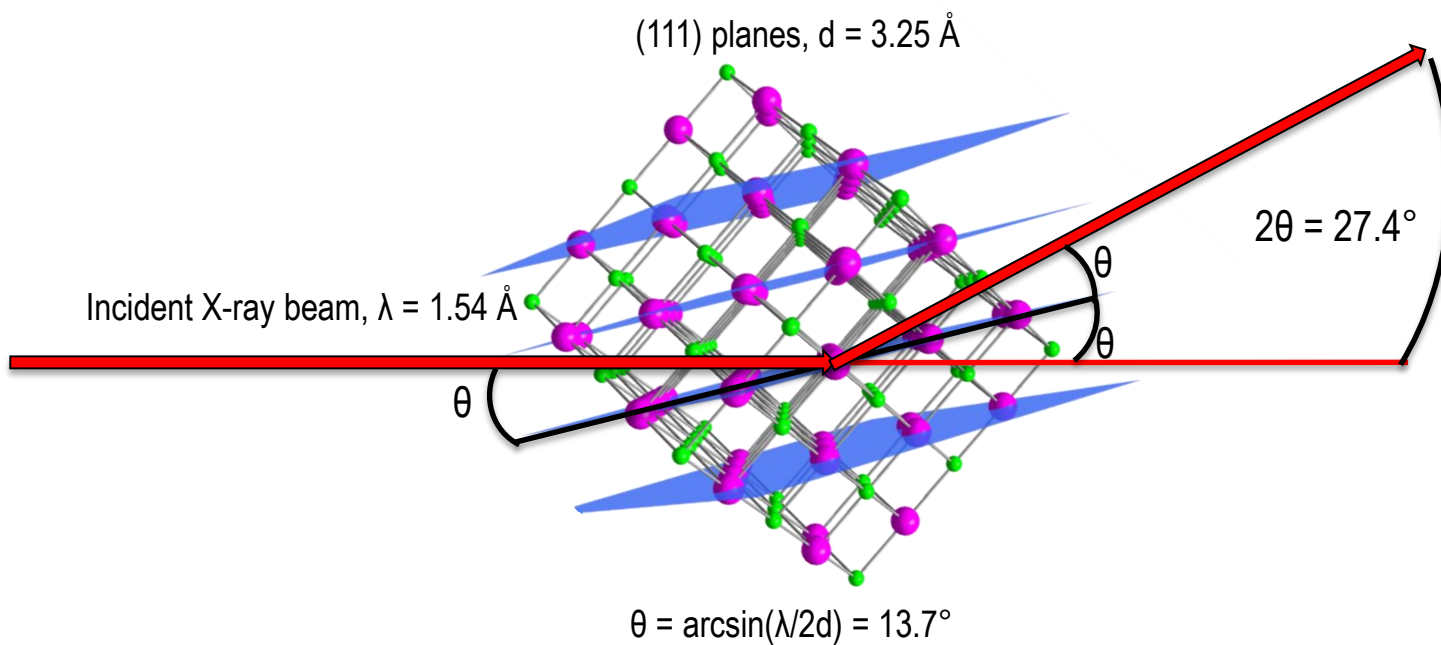
Fundamentals of X-Ray Diffraction



Fundamentals of X-Ray Diffraction

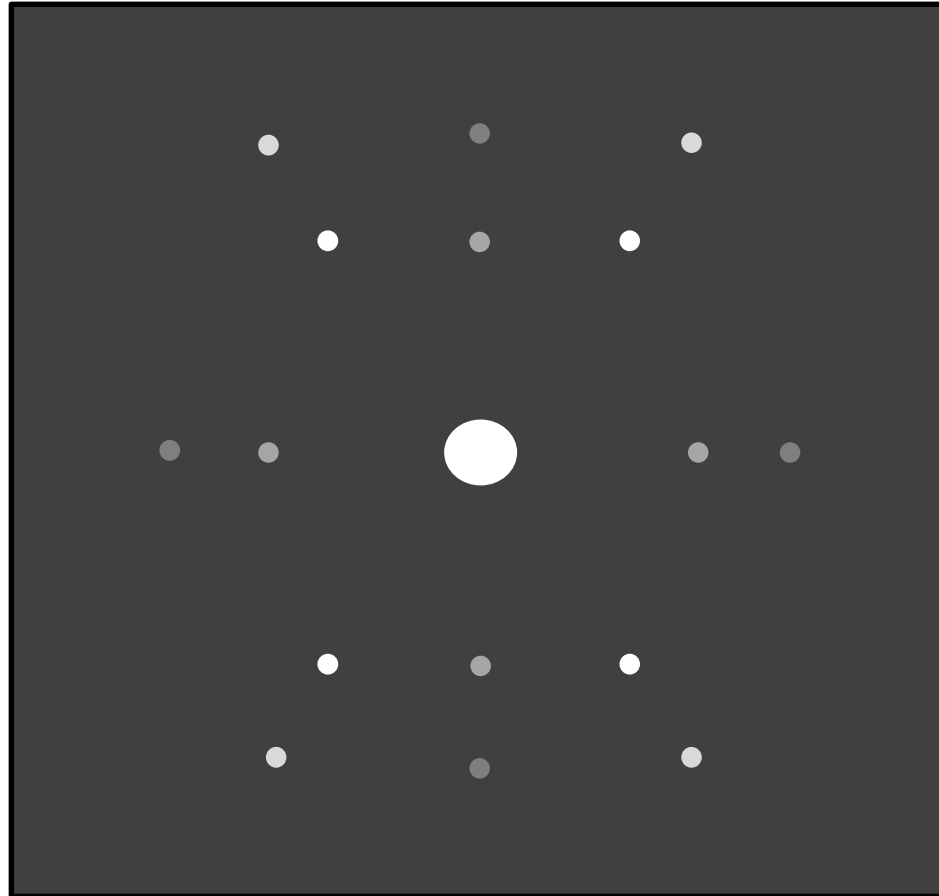
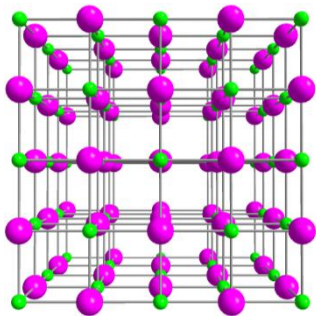


Fundamentals of X-Ray Diffraction



Fundamentals of X-Ray Diffraction

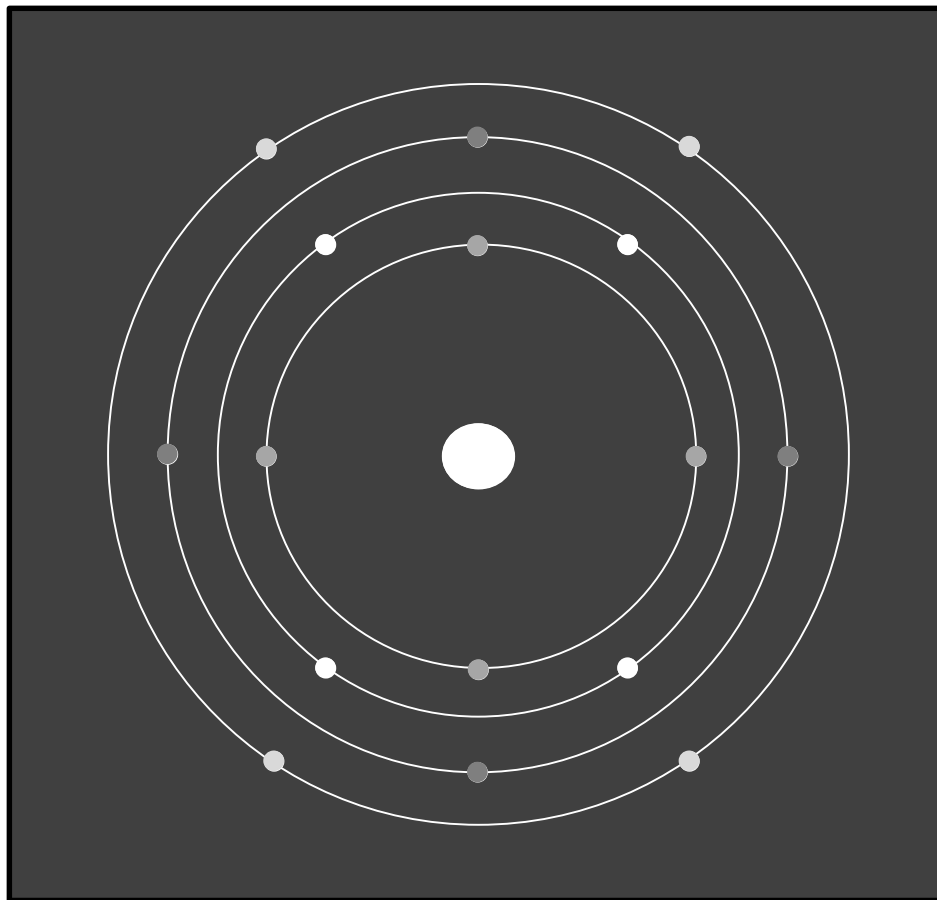
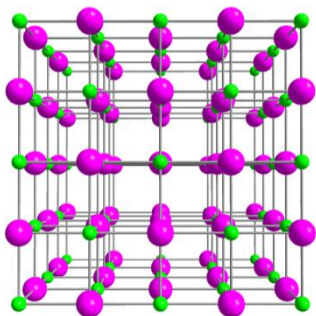
The diffraction pattern of a **single crystal** consists of **spots** whose distance from the center (that is the axis of the incident beam) is a consequence of the d spacing of the crystallographic planes which generated the diffraction effect. The closer the spots to the center, the lower the θ angle at which diffraction occurs, the larger the d spacing.



Fundamentals of X-Ray Diffraction

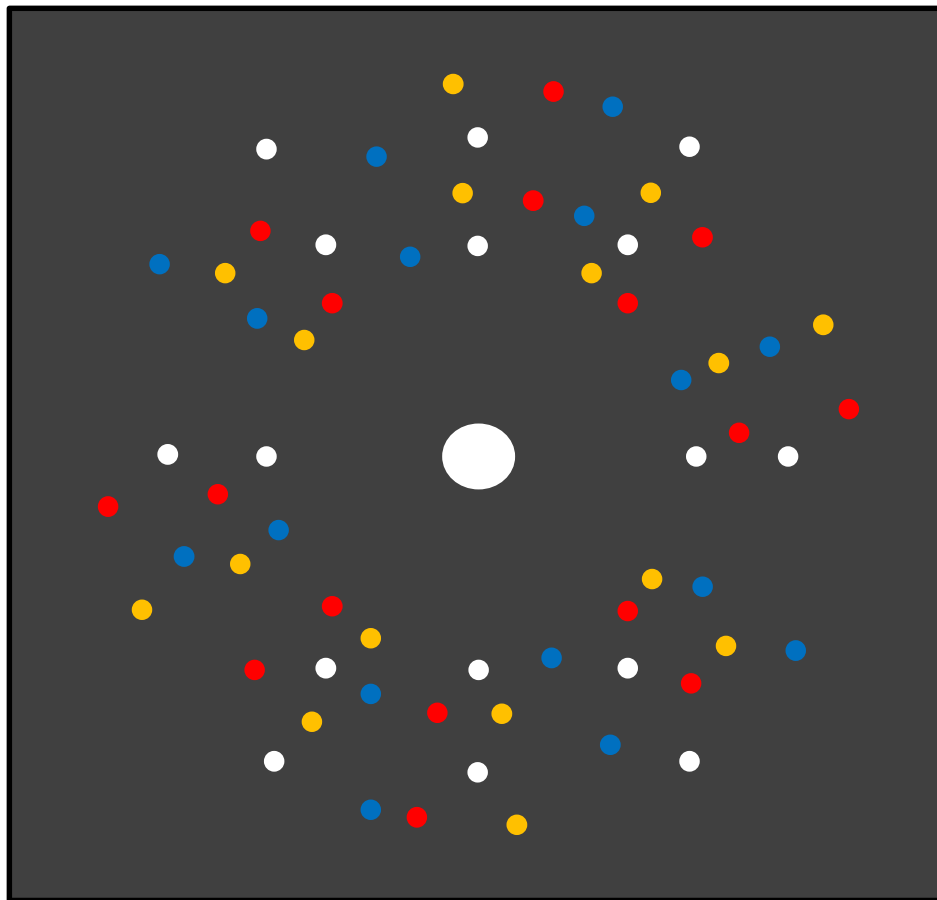
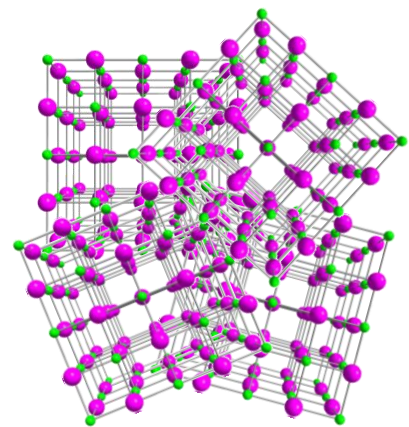
Every family of crystallographic planes generates a group of spots at the same distance from the center. The number of these spots depends on the symmetry of the crystal.

The brightness of the spots (i.e. their **intensity**) is dependent on the **electron density** of the lattice planes scattering the radiation (see slide 48).



Fundamentals of X-Ray Diffraction

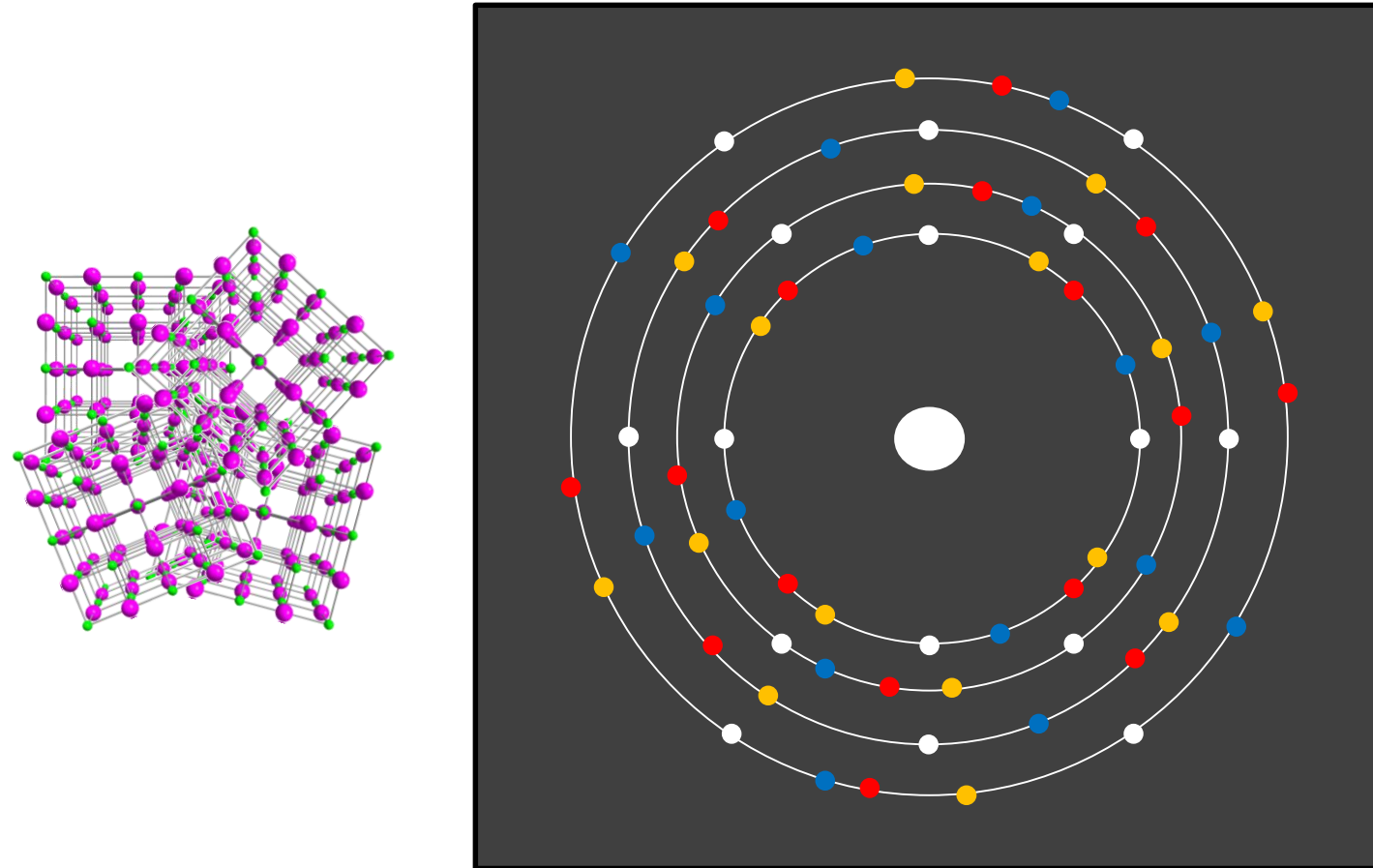
If the sample is constituted of **four single crystals** of the same compound, each oriented in a different way, the diffraction figure produced will be the sum of the diffraction figures representative of the lattice of each crystal.



Fundamentals of X-Ray Diffraction

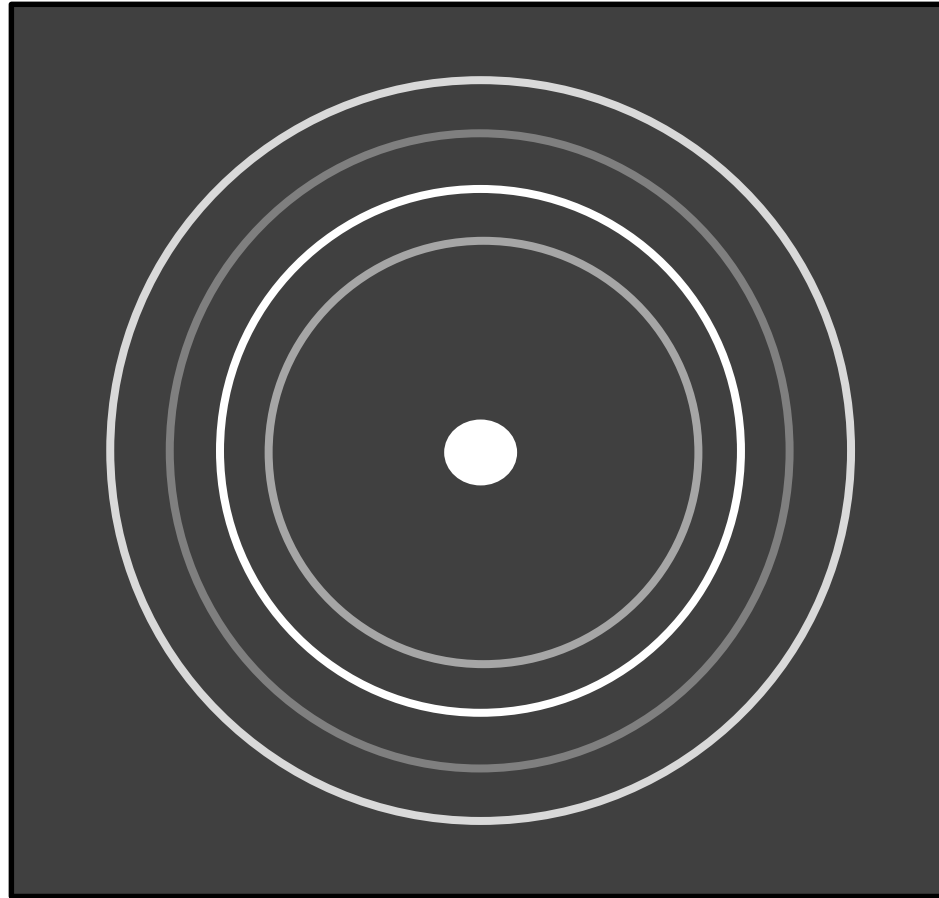
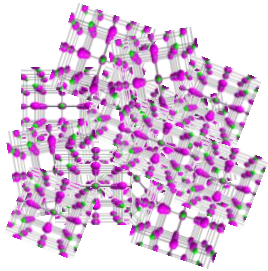
The different orientation of the crystals will generate spots lying at the same distance from the center, but shifted along the circle.

The spots lying on the same circle are due to the same family of crystallographic planes in each crystal of the sample.

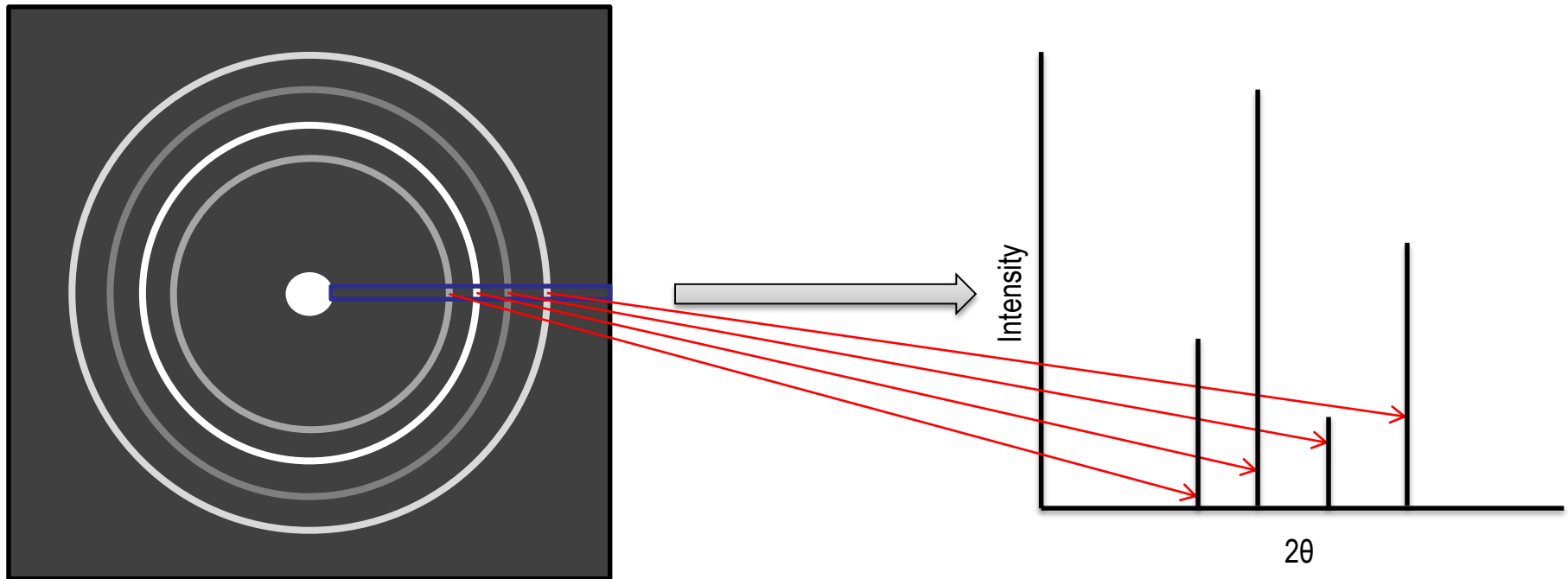


Fundamentals of X-Ray Diffraction

If the sample is constituted of a **large number of crystals oriented in all of the possible directions**, the spots belonging to each crystal will sum up to produce continuous circular lines, **the diffraction rings**. As for a single crystal, the intensity of the lines is dependent on the electron density of the crystallographic planes scattering the radiation.



By «cutting» the diffraction lines in a radial manner and representing this section as a plot of the intensity as a function of the distance from the center (normally expressed as 2θ), we get the typical powder X-ray diffraction (**PXRD**) pattern of a polycrystalline solid.



Highlights

- Diffraction is an elastic scattering phenomenon occurring when a wave interacts with an obstacle of size comparable to its wavelength
- Crystal structures can diffract X-rays because interatomic distances are in the same range of X-rays wavelength
- X-rays interact with the electron cloud of atoms
- The condition for having diffraction effect is determined by Bragg's law $n \lambda = 2 d \sin \theta$
- The diffraction pattern of a polycrystalline material is the result of the contribution of many single crystals constituting the sample

Where do X-rays come from?

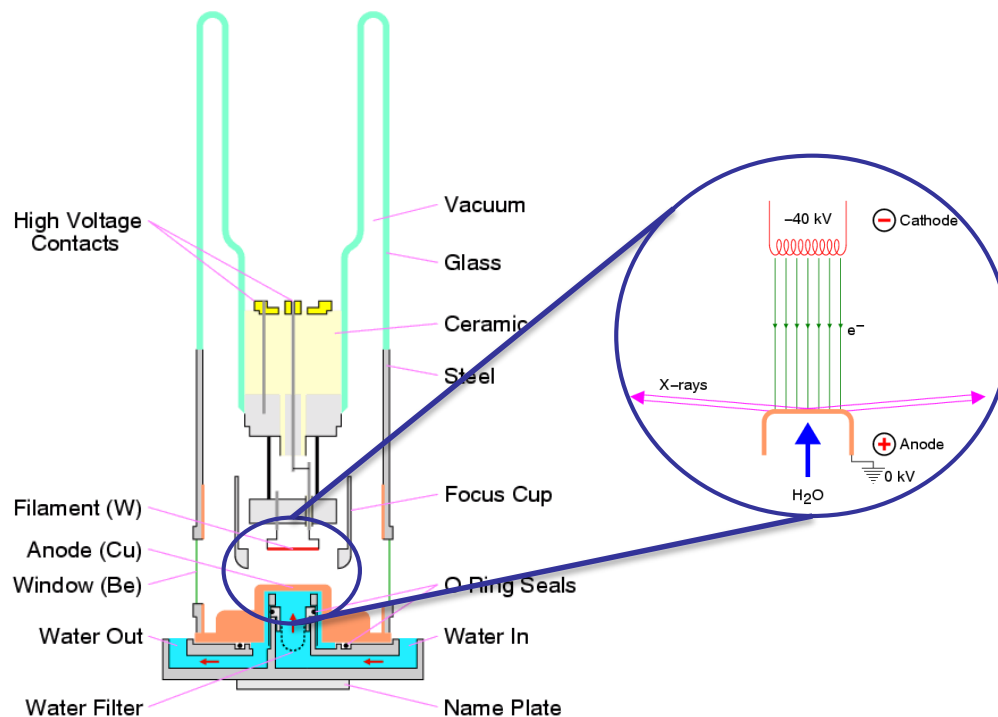
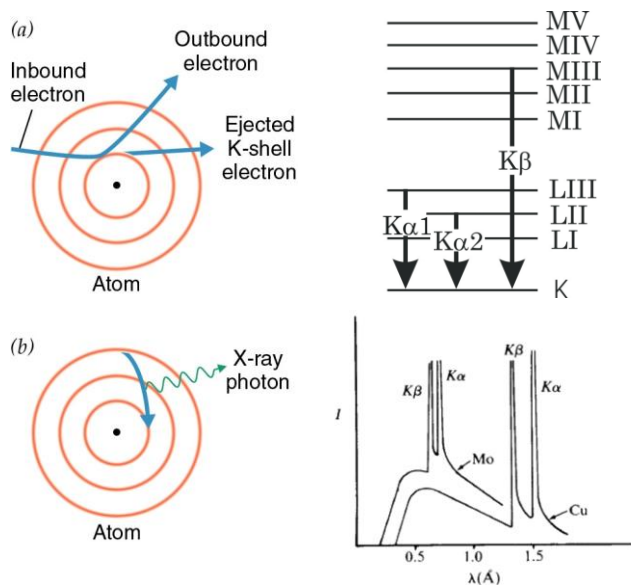
1. Fire beam of electrons at metal target

Ionization of **inner shell electrons** results in formation of an 'electron hole', followed by **relaxation** of electrons from upper shells. The energy difference is released in the form of X-rays of specific wavelengths.

Commonly used radiations are Cu $K\alpha$ ($\lambda = 1.5418 \text{ \AA}$) and Mo $K\alpha$ ($\lambda = 0.71073 \text{ \AA}$).

$K\beta$ can be suppressed using an appropriate filter, while for $K\alpha_2$ a monochromator is needed.

Such sources are normally used in **laboratory diffractometers**.



Where do X-rays come from?

2. Accelerate electrons in a particle accelerator (synchrotron source).

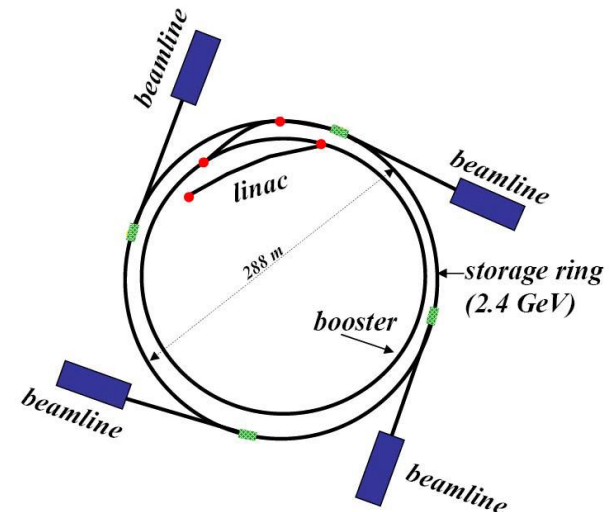
Electrons are accelerated at **relativistic velocities** in circular orbits. As velocities approach the speed of light they emit electromagnetic radiation in the X-ray region.

The X-rays produced have a range of wavelengths, which can be selected depending on the type of application they are needed for.

Synchrotron radiation features **high brilliance**, which takes into account the number of photons produced per second the angular divergence of the photons, the cross-sectional area of the beam and the photons falling within a bandwidth (BW) of 0.1% of the central wavelength or frequency. The greater the brilliance, the more photons of a given wavelength and direction are concentrated on a spot per unit of time.



Swiss Light Source @ Paul Scherrer Institut



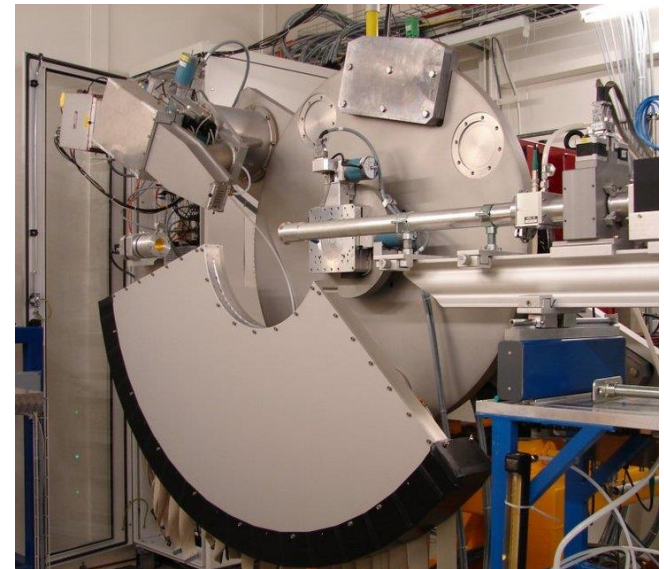
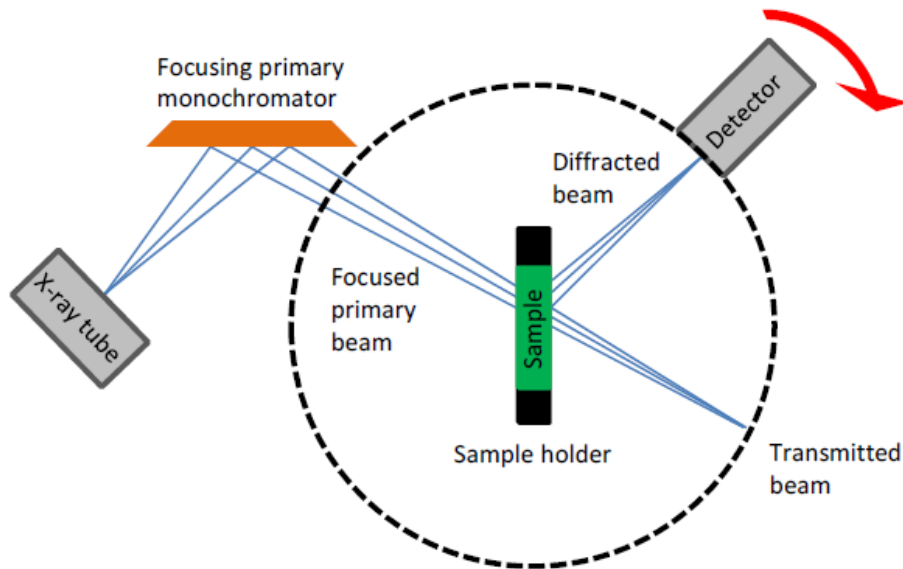
How is a PXRD measurement performed?

1. Debye-Scherrer geometry

Also termed **transmission geometry**, it employs a **capillary** as a sample holder and works best for materials with **low absorption**. No effects of preferred orientation exist in this geometry.

A few mg of sample are required and sensitive materials can be easily analyzed.

It is mostly used at synchrotron beamlines.



MS Beamline @ Swiss Light Source

How is a PXRD measurement performed?

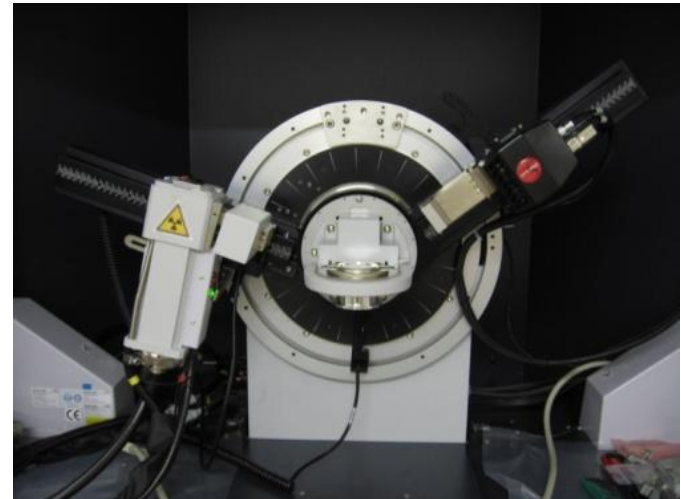
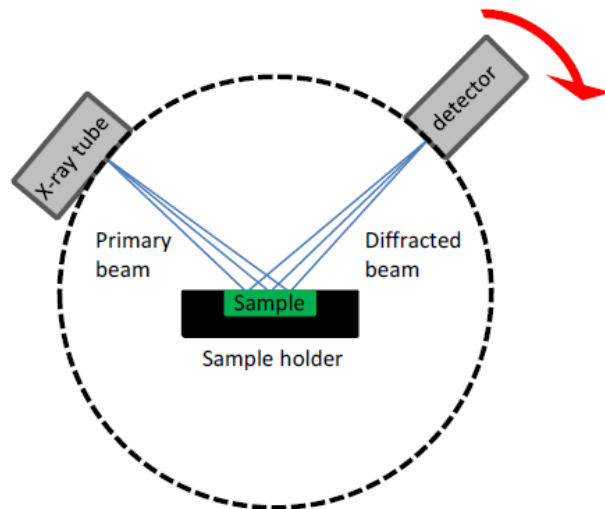
2. Bragg-Brentano geometry

Also termed **reflection geometry**, it requires a **flat sample** of virtually **infinite thickness**, so as to make sure that the radiation is completely reflected to the detector. Effects of preferred orientation can easily occur in this geometry.

Depending on the absorptivity of the sample, the amount needed for a measurement can be in the range of **tens on mg**.

Using non-ambient chambers (high temperature, inert atmosphere, reactive gases), in situ experiments can easily be performed at the laboratory scale.

It is mostly used in laboratory diffractometers.



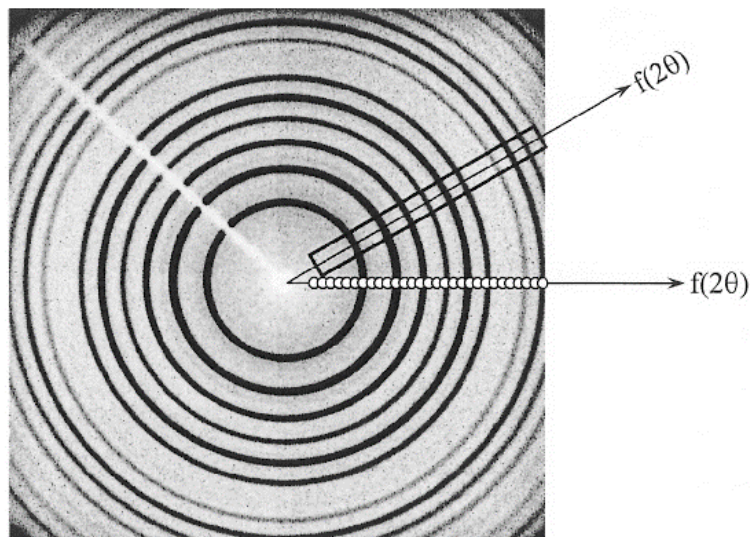
How is the information gathered?

The **detector** is a fundamental part of the diffractometer, and it heavily influences the **quality** and the **speed** of a measurement.

Detection of X-rays is accomplished by **interaction of radiation with matter** and subsequent production of certain effects or signals, for example to generate particles, waves, electrical current, etc., which can be easily registered.

Detector **efficiency** is determined by first, a fraction of X-ray photons that pass through the detector window (the higher, the better) and second, a fraction of photons that are absorbed by the detector and thus result in a series of detectable events (again, the higher, the better).

Detectors can be classified according to the **capability of resolving the location where the photon has been absorbed** and thus, whether they can detect the direction of the beam in addition to counting the number of photons. Three types of detectors can thus be identified: **point detectors (0D)**, **line detectors (1D)**, and **area detectors (2D)**.



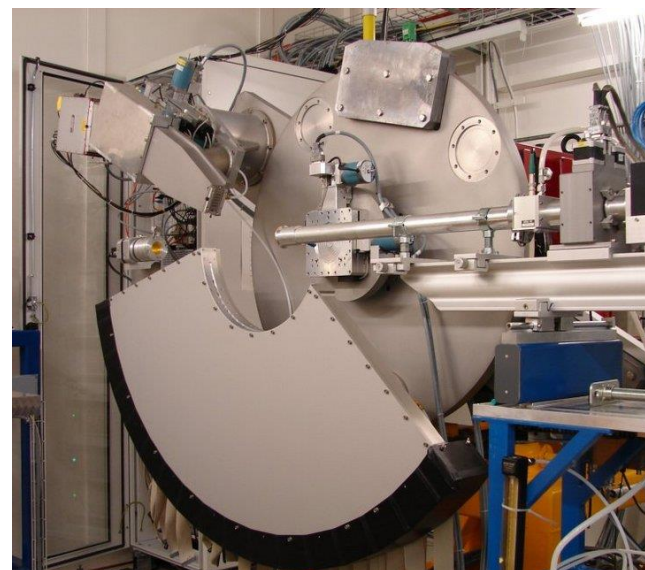
How is the information gathered?

Position Sensitive Detectors (**PSD**) are line detectors. They are the most widespread nowadays, thanks to the short measurement times and the good accuracy that they guarantee.



LYNXEYE XE installed on Bruker D8 Advance at PSI

- Maximum angular range: 2.9°
- Energy dispersive: able to reduce the fluorescence
- No need for secondary monochromators or metal filters



MYTHEN II installed at MS Beamline at SLS

- Maximum angular range: 120°
- Constituted of 30'720 silicon elements, divided up into 24 modules of 1280 elements each
- Allows very fast acquisition of high resolution data

Highlights

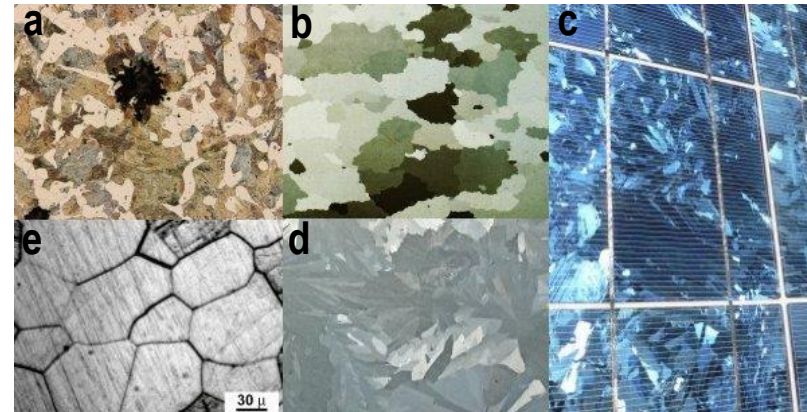
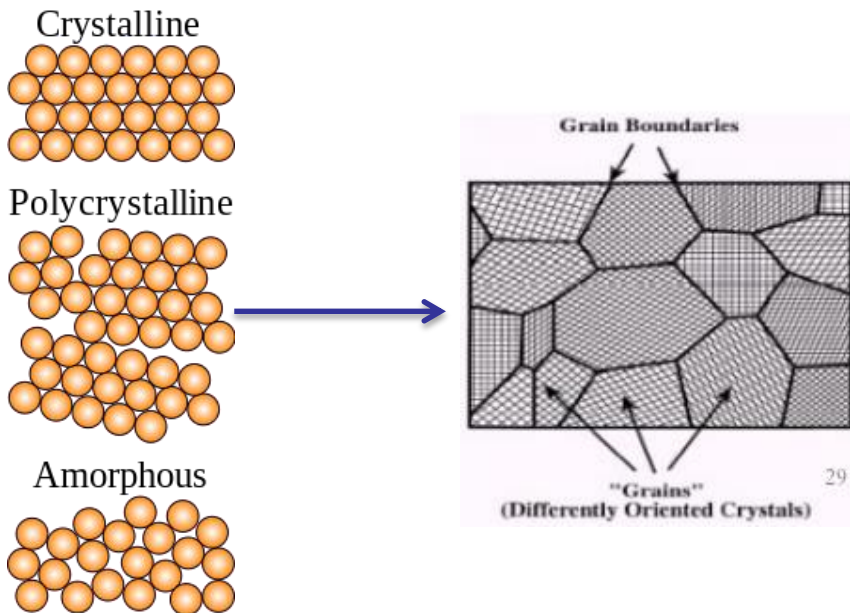
- X-rays can be generated either by firing electrons against a metal target or by accelerating electrons at relativistic velocities in circular orbits
- Powder diffraction measurements can be performed either in Debye-Scherrer transmission geometry or in Bragg-Brentano reflection geometry
- The detector allows to harvest the information and can be designed to operate in different ways, the most common being the PSD

What is a polycrystalline sample?

A polycrystalline solid is an aggregate of a large number of small crystals or grains, called **crystallites**, arranged in a random fashion, each having its own regular structure.

Polycrystalline materials are employed in a very wide range of **practical applications**, and even if a material is obtained in single crystal form it is often reduced to microcrystal form (i.e. powder) prior to use.

As a consequence, PXRd is a very important analytical technique in solid state chemistry, heterogeneous catalysis, materials science, pharmaceutical industry, and so on.



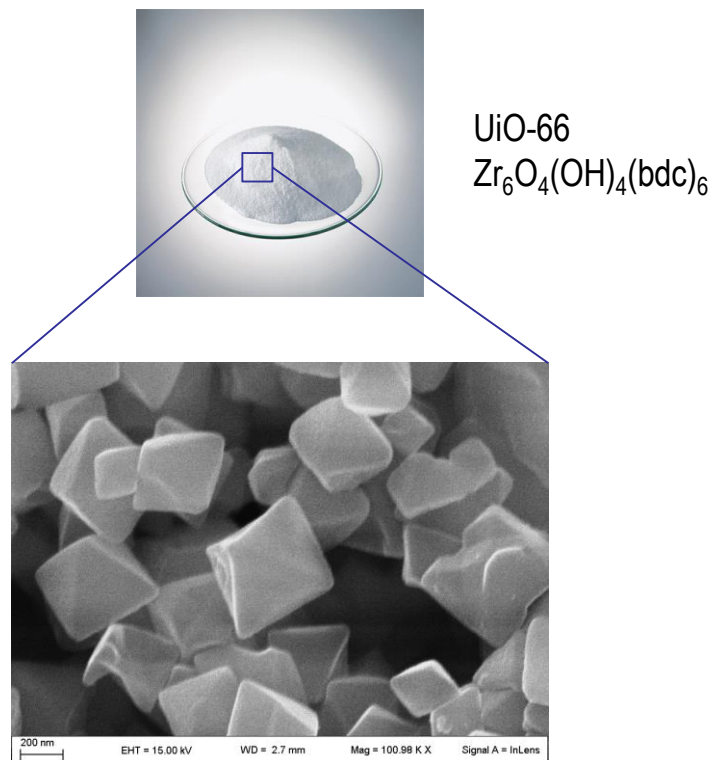
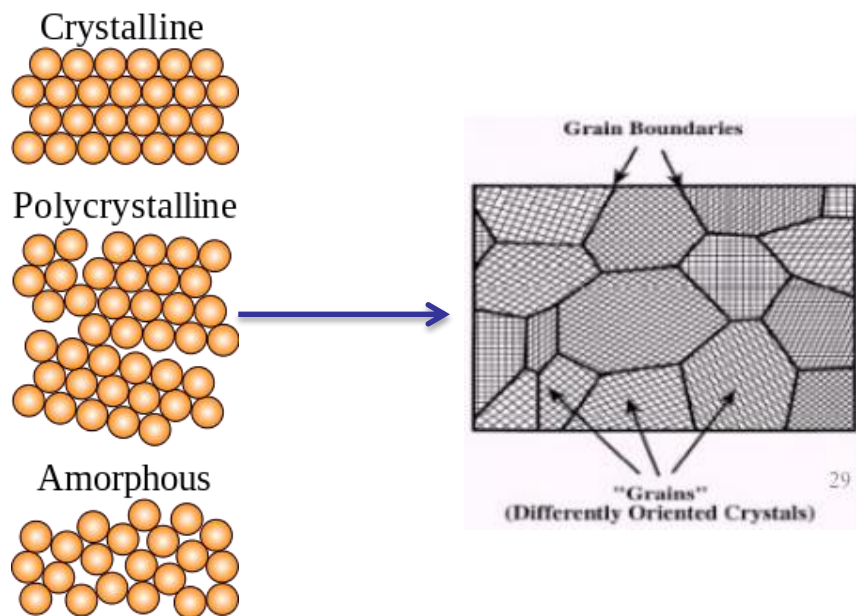
- a) malleable iron
- b) electrical steel without coating
- c) solar cells made of multicrystalline silicon
- d) galvanized surface of zinc
- e) micrograph of acid etched metal highlighting grain boundaries

What is a polycrystalline sample?

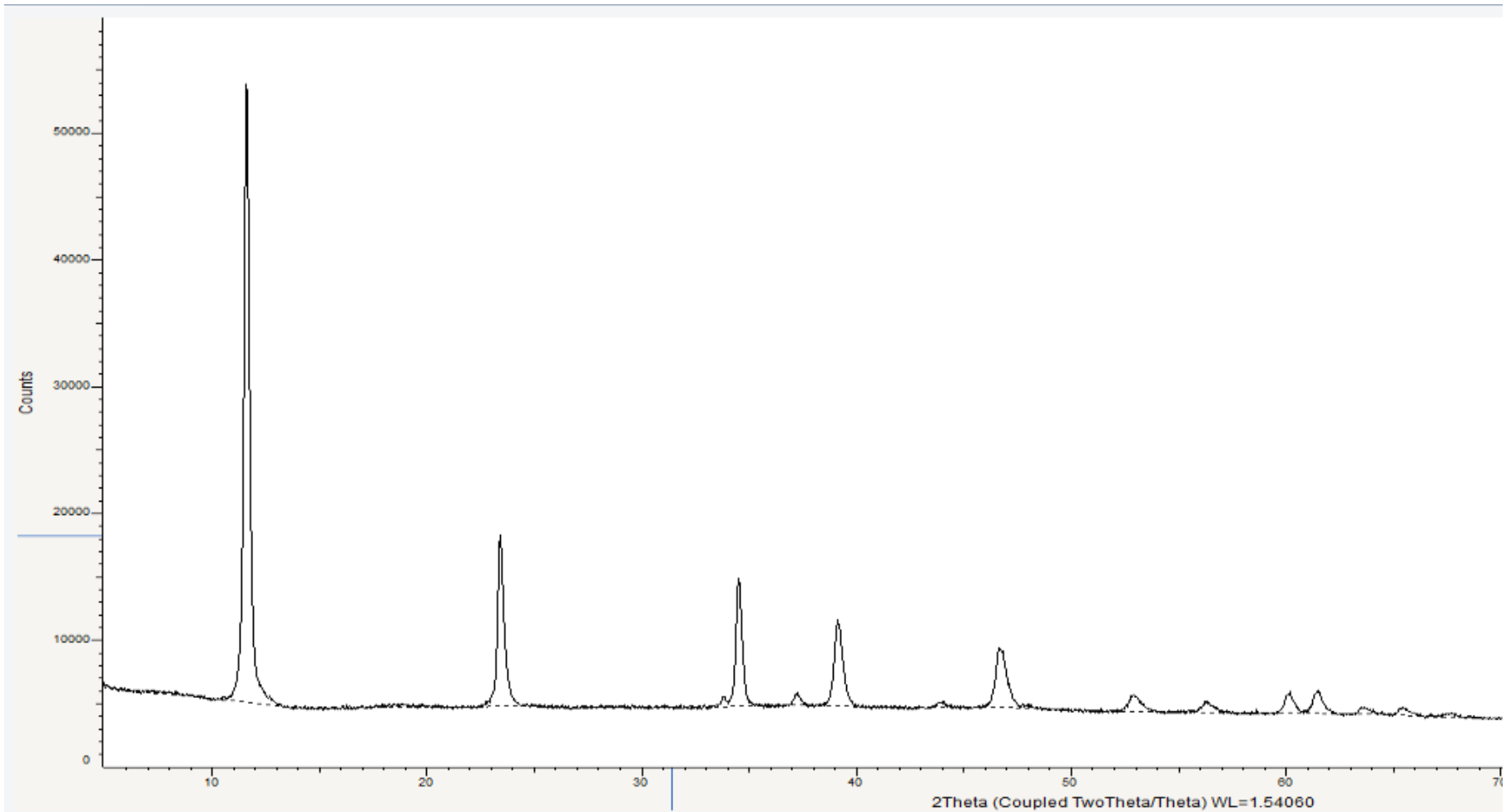
A polycrystalline solid is an aggregate of a large number of small crystals or grains, called **crystallites**, arranged in a random fashion, each having its own regular structure.

Polycrystalline materials are employed in a very wide range of **practical applications**, and even if a material is obtained in single crystal form it is often reduced to microcrystal form prior to use.

As a consequence, PXRD is a very important analytical technique in solid state chemistry, heterogeneous catalysis, materials science, pharmaceutical industry, and so on.

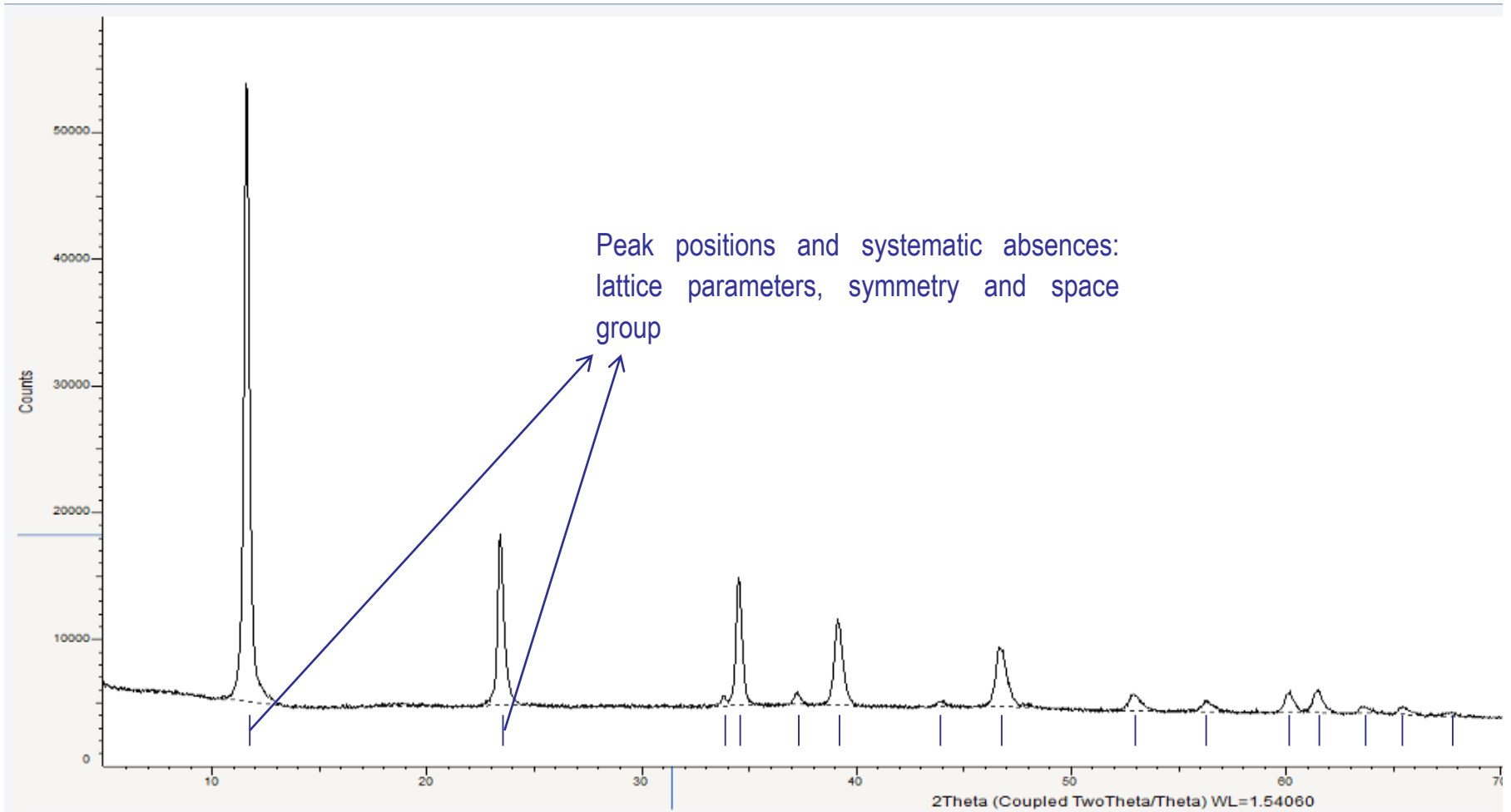


What does a PXRD pattern tell us?



The diffraction pattern reflects the nature of the material under investigation, it is like a **fingerprint**.

What does a PXRD pattern tell us?



Diffraction by Polycrystalline Solids

The process of **indexing** consists in the attribution of Miller indices (hkl) to every observed Bragg peak, i.e. the determination of the lattice parameters.

It is basically a **trial-and-error** computational procedure which requires the position of at least 20 reflections as an input and the definition by the user of some parameters (symmetry, max cell axes length and angles, max volume) to narrow the search for a unit cell that can predict the correct Miller indices.

The goodness of the indexing procedure can be estimated by various **figures of merit**.

```

TOTAL NUMBER OF LINES = 20
A = 14.756830 .015568 A ALFA = 90.000000 .000000 DEG
B = 8.845984 .004741 A BETA = 97.522960 .067834 DEG
C = 8.867941 .005909 A GAMMA = 90.000000 .000000 DEG
UNIT CELL VOLUME = 1147.65 A**3
  
```

H	K	L	SST-OBS	SST-CALC	DELTA	2TH-OBS	2TH-CALC	D-OBS	FREE PARAM.
0	1	0		.007583			9.991		
0	0	1	.007678	.007677	.000001	10.054	10.053	8.7910	5
1	1	0	.010385	.010355	.000030	11.698	11.681	7.5588	14
2	0	0	.010995	.011089	-.000094	12.038	12.090	7.3463	62
0	1	1	.015284	.015260	.000024	14.203	14.192	6.2308	57
-2	0	1	.016346	.016350	-.000004	14.691	14.693	6.0249	33
-1	1	1	.016846	.016824	.000022	14.915	14.905	5.9349	12
2	1	0	.018626	.018672	-.000046	15.688	15.708	5.6442	20
1	1	1	.019244	.019240	.000004	15.948	15.946	5.5528	15
2	0	1	.021124	.021182	-.000058	16.714	16.737	5.3000	2
-2	1	1	.023927	.023933	-.000006	17.797	17.799	4.9798	86
2	1	1	.028644	.028765	-.000120	19.488	19.529	4.5514	35
0	2	0	.030390	.030331	.000059	20.079	20.059	4.4187	44
0	0	2	.030711	.030707	.000004	20.186	20.185	4.3955	53
1	2	0	.033097	.033103	-.000006	20.964	20.966	4.2341	7
-2	0	2	.036966	.036965	.000001	22.170	22.170	4.0064	100
0	2	1	.037993	.038008	-.000014	22.480	22.484	3.9519	12
-1	1	2	.038657	.038647	.000010	22.678	22.675	3.9178	12
1	2	1	.041934	.041988	-.000054	23.633	23.648	3.7616	77
3	1	1	.043979	.043834	.000145	24.211	24.170	3.6731	85
2	0	2	.046504	.046629	-.000125	24.907	24.941	3.5720	22
-2	2	1		.046681			24.955		

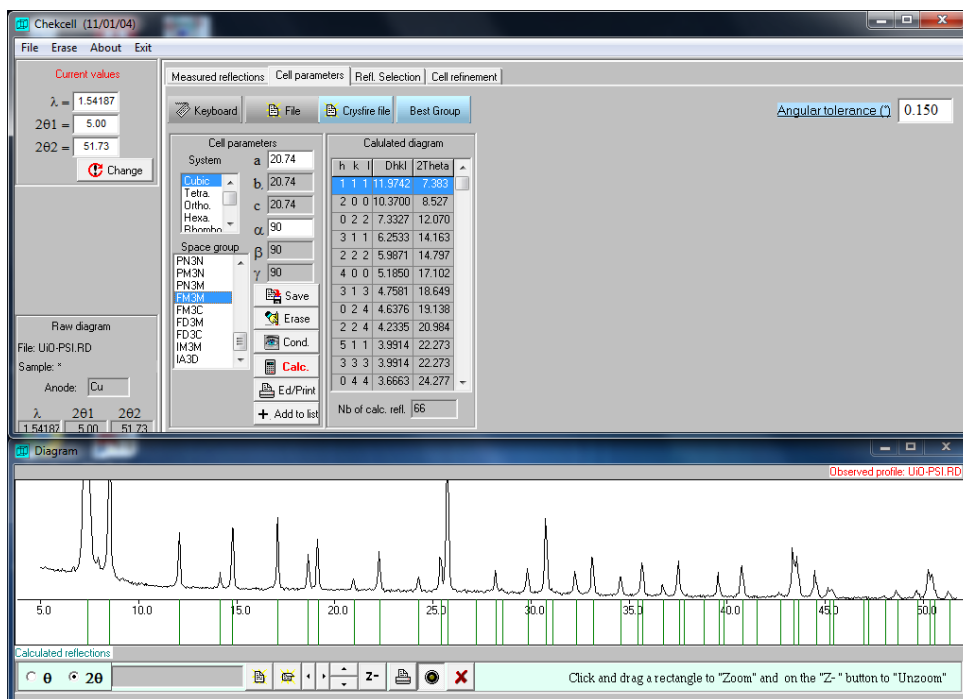
```

NUMBER OF OBS. LINES = 20 NUMBER OF CALC. LINES = 22
M( 20) = 16 AV.EPS. = .0000414 ; F 20 = 37.( .015036, 36)
0 LINES ARE UNINDEXED
  
```

The typical output of the program TREOR.

Once the most probable unit cell has been found, analysis of the **systematic absences** of classes of reflections allows to identify if specific **reflection conditions** apply.

Systematic absences derive from the existence of particular **symmetry operations** inside the cell, which define the **space group**.



$Fm\bar{3}m$

Symmetry Operators

- | | | |
|----|-----------------------|---|
| 1 | x, y, z | 1 |
| 2 | x, \bar{y}, \bar{z} | 2 (x, 0, 0) |
| 3 | \bar{x}, y, \bar{z} | 2 (0, y, 0) |
| 4 | \bar{x}, \bar{y}, z | 2 (0, 0, z) |
| 5 | z, x, y | 3 ⁺ (x, x, x) |
| 6 | \bar{z}, \bar{x}, y | 3 ⁺ (x, \bar{x} , \bar{x}) |
| 7 | z, x, \bar{y} | 3 ⁺ (\bar{x} , x, \bar{x}) |
| 8 | \bar{z}, x, \bar{y} | 3 ⁺ (\bar{x} , \bar{x} , x) |
| 9 | y, z, x | 3 ⁻ (x, x, x) |
| 10 | \bar{y}, z, \bar{x} | 3 ⁻ (x, \bar{x} , \bar{x}) |
| 11 | \bar{y}, z, x | 3 ⁻ (\bar{x} , x, \bar{x}) |
| 12 | y, z, \bar{x} | 3 ⁻ (\bar{x} , \bar{x} , x) |
| 13 | x, z, y | 4 ⁺ (x, 0, 0) |
| 14 | x, z, \bar{y} | 4 ⁻ (x, 0, 0) |
| 15 | \bar{x}, z, \bar{y} | 2 (0, \bar{y} , y) |
| 16 | \bar{x}, z, y | 2 (0, y, y) |

No. 225

Reflection Conditions

- (general)
- hkl : $h + k, h + l, k + l = 2n$
- $0kl$: $k, l = 2n$
- $h0l$: $h, l = 2n$
- $hk0$: $h, k = 2n$
- hhl : $h + l = 2n$
- hkh : $h + k = 2n$
- hkk : $h + k = 2n$
- $h00$: $h = 2n$
- $0k0$: $k = 2n$
- $00l$: $l = 2n$
- $0kk$: $k = 2n$
- $h0h$: $h = 2n$
- $hh0$: $h = 2n$

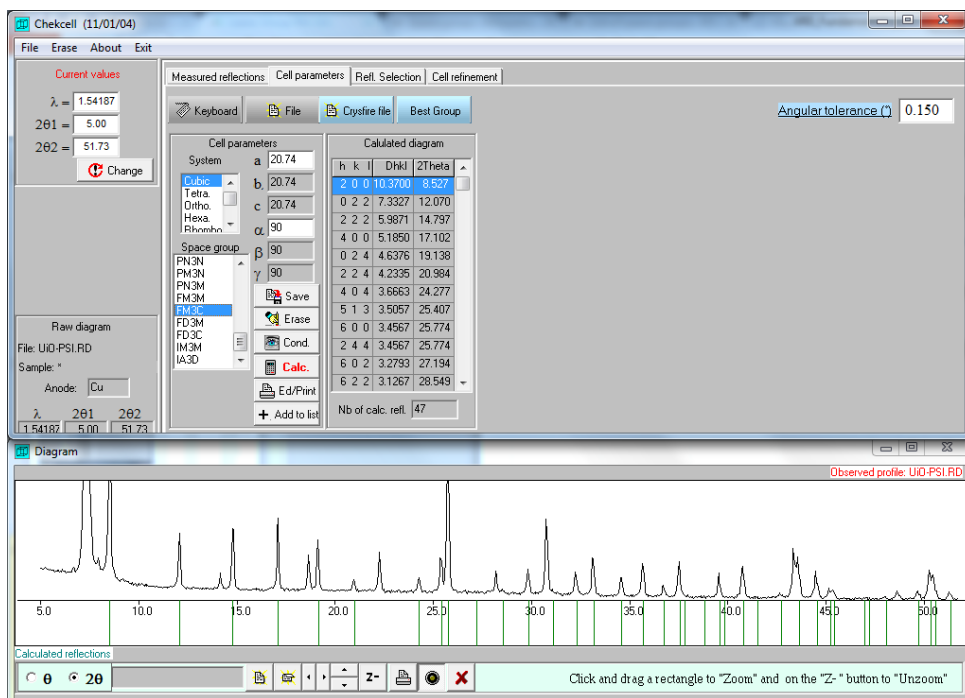
(more)



The pattern of the metal-organic framework UiO-66 is indexed by a cubic cell with $a = 20.74 \text{ \AA}$. Analysis of the systematic absences performed with the program **Chekcell** suggests that the most probable space group is $Fm\bar{3}m$.

Once the most probable unit cell has been found, analysis of the **systematic absences** of classes of reflections allows to identify if specific **reflection conditions** apply.

Systematic absences derive from the existence of particular **symmetry operations** inside the cell, which define the **space group**.



$Fm\bar{3}c$

Symmetry Operators

- | | | |
|----|-------------------------------------|--|
| 1 | x, y, z | 1 |
| 2 | x, \bar{y}, \bar{z} | 2 (x, 0, 0) |
| 3 | \bar{x}, y, \bar{z} | 2 (0, y, 0) |
| 4 | \bar{x}, \bar{y}, z | 2 (0, 0, z) |
| 5 | z, x, y | 3 ⁺ (x, x, x) |
| 6 | \bar{z}, \bar{x}, y | 3 ⁺ (x, \bar{x} , \bar{x}) |
| 7 | z, \bar{x}, \bar{y} | 3 ⁺ (\bar{x} , x, \bar{x}) |
| 8 | \bar{z}, x, \bar{y} | 3 ⁺ (\bar{x} , \bar{x} , x) |
| 9 | y, z, x | 3 ⁻ (x, x, x) |
| 10 | \bar{y}, z, \bar{x} | 3 ⁻ (x, \bar{x} , \bar{x}) |
| 11 | \bar{y}, \bar{z}, x | 3 ⁻ (\bar{x} , x, \bar{x}) |
| 12 | y, \bar{z}, \bar{x} | 3 ⁻ (\bar{x} , \bar{x} , x) |
| 13 | $x, \bar{z}, \frac{1}{2} + y$ | 4 ⁺ ($x, \frac{1}{4}, \frac{1}{4}$) |
| 14 | $x, z, \frac{1}{2} - y$ | 4 ⁻ ($x, \frac{1}{4}, \frac{1}{4}$) |
| 15 | $\bar{x}, \bar{z}, \frac{1}{2} - y$ | 2 ₁ ($0, \frac{1}{4} - y, y$) [$0, \frac{1}{4}, \frac{1}{4}$] |
| 16 | $\bar{x}, z, \frac{1}{2} + y$ | 2 ₁ ($0, \frac{1}{4} + y, y$) [$0, \frac{1}{4}, \frac{1}{4}$] |

No. 226

Reflection Conditions

(general)

- $hkl : h + k, h + l, k + l = 2n$
 $0kl : k, l = 2n$
 $h0l : h, l = 2n$
 $hk0 : h, k = 2n$
 $hhl : h, l = 2n$
 $hkh : h, k = 2n$
 $h00 : h = 2n$
 $0k0 : k = 2n$
 $00l : l = 2n$
 $0kk : k = 2n$
 $h0h : h = 2n$
 $hh0 : h = 2n$

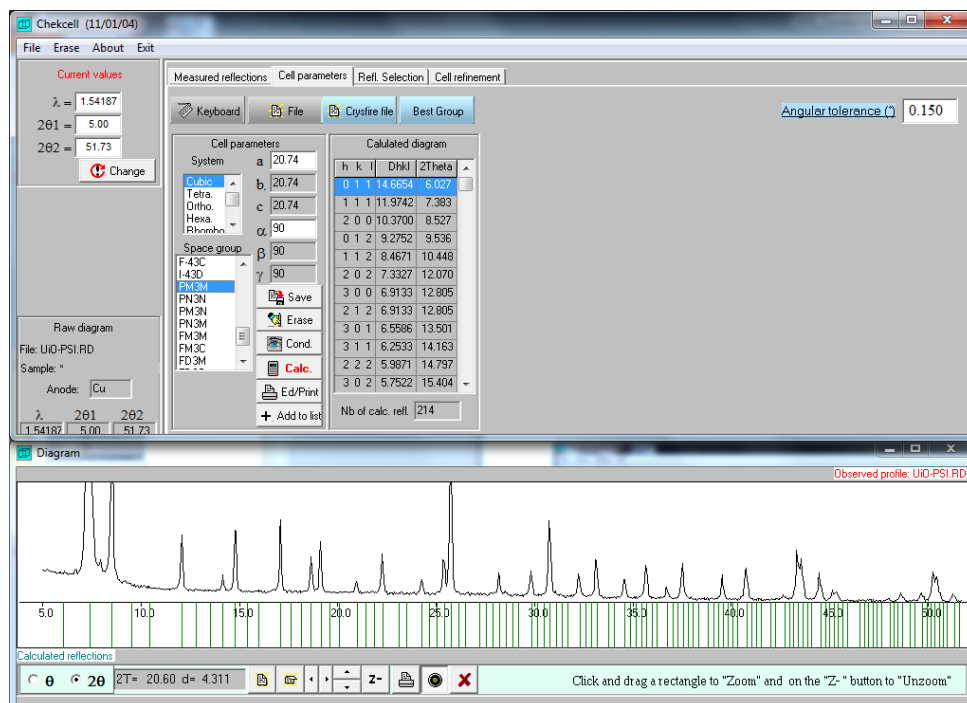
(more)



The pattern of the metal-organic framework UiO-66 is indexed by a cubic cell with $a = 20.74$ Å. Analysis of the systematic absences performed with the program **Chekcell** suggests that the most probable space group is $Fm\bar{3}m$.

Once the most probable unit cell has been found, analysis of the **systematic absences** of classes of reflections allows to identify if specific **reflection conditions** apply.

Systematic absences derive from the existence of particular **symmetry operations** inside the cell, which define the **space group**.



$Pm\bar{3}m$

Symmetry Operators

- | | | |
|----|-----------------------------|------------------------------------|
| 1 | x, y, z | 1 |
| 2 | x, \bar{y}, \bar{z} | 2 (x, 0, 0) |
| 3 | \bar{x}, y, \bar{z} | 2 (0, y, 0) |
| 4 | \bar{x}, \bar{y}, z | 2 (0, 0, z) |
| 5 | z, x, y | 3^+ (x, x, x) |
| 6 | \bar{z}, \bar{x}, y | 3^+ (x, \bar{x} , \bar{x}) |
| 7 | z, \bar{x}, \bar{y} | 3^+ (\bar{x} , x, \bar{x}) |
| 8 | \bar{z}, x, \bar{y} | 3^+ (\bar{x} , \bar{x} , x) |
| 9 | y, z, x | 3^- (x, x, x) |
| 10 | \bar{y}, z, \bar{x} | 3^- (x, \bar{x} , \bar{x}) |
| 11 | \bar{y}, \bar{z}, x | 3^- (\bar{x} , x, \bar{x}) |
| 12 | y, \bar{z}, \bar{x} | 3^- (\bar{x} , \bar{x} , x) |
| 13 | x, \bar{z}, y | 4^+ (x, 0, 0) |
| 14 | x, z, \bar{y} | 4^- (x, 0, 0) |
| 15 | $\bar{x}, \bar{z}, \bar{y}$ | 2 (0, \bar{y} , y) |
| 16 | \bar{x}, z, y | 2 (0, y, y) |

No. 221

Reflection Conditions

(general)

No conditions



(more)

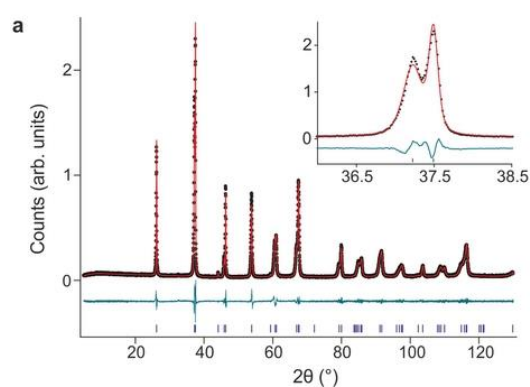


The pattern of the metal-organic framework UiO-66 is indexed by a cubic cell with $a = 20.74$ Å. Analysis of the systematic absences performed with the program **Chekcell** suggests that the most probable space group is $Fm\bar{3}m$.

The correctness of the chosen unit cell and space group can be proved by performing a **whole powder pattern fitting (WPPF)**, a procedure that assumes that the entire powder pattern of a given compound can be modeled on the basis of a single profile function.

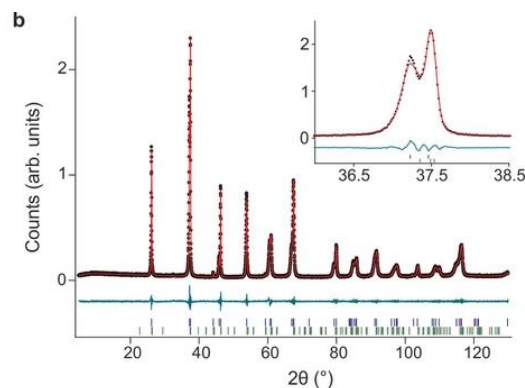
WPPF is an **ab initio procedure** that does not require a priori knowledge of the crystal structure, it just refines lattice parameters, zero error, peak width parameters, background parameters, and calculates the peak intensities in order to obtain a profile function that fits the experimental pattern. If the selected lattice parameters and the space group are wrong, the fitting will be poor.

There are two approaches to perform WPPF: the **Pawley** method and the **Le Bail** method, which mainly differ for the way the intensities are calculated.



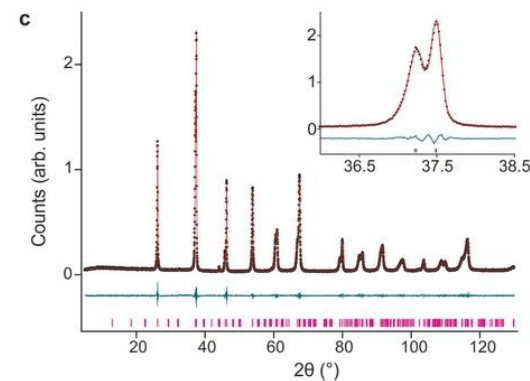
$$R3c$$

$$R_{wp} = 7.421$$



$$R3c + Pna2_1$$

$$R_{wp} = 6.373$$



$$P11a$$

$$R_{wp} = 6.169$$

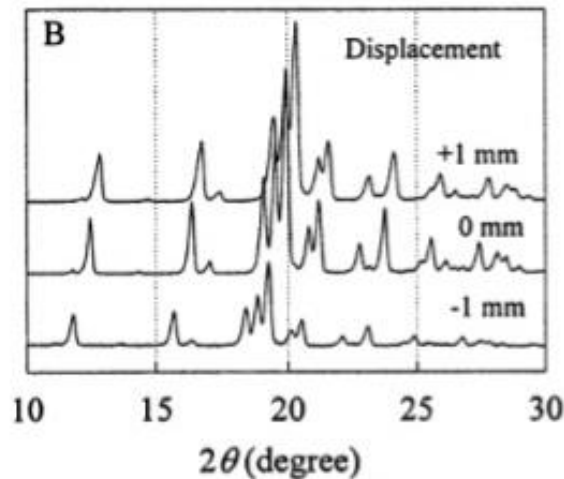
Diffraction by Polycrystalline Solids

Both **zero error** and **sample displacement** cause a **general and constant shift** of the pattern towards higher or lower 2θ angles.

As the relation between d spacing and θ is not linear, the same shift at different 2θ angles will affect more heavily the reflections associated to large d spacings.

To get rid of zero error, the instrument must be appropriately calibrated using a reference material (normally Si).

Sample displacement can be limited by a careful preparation of the sample, but it is hard to completely get rid of it.



Example:

$$\lambda = 1.54056 \text{ \AA}; \text{ Shift} = +0.1^\circ$$

$$2\theta = 5^\circ, \theta = 2.5^\circ, d = \lambda/2\sin\theta = 17.66 \text{ \AA}$$

$$2\theta = 5.1^\circ, \theta = 2.55^\circ, d = \lambda/2\sin\theta = 17.32 \text{ \AA}$$

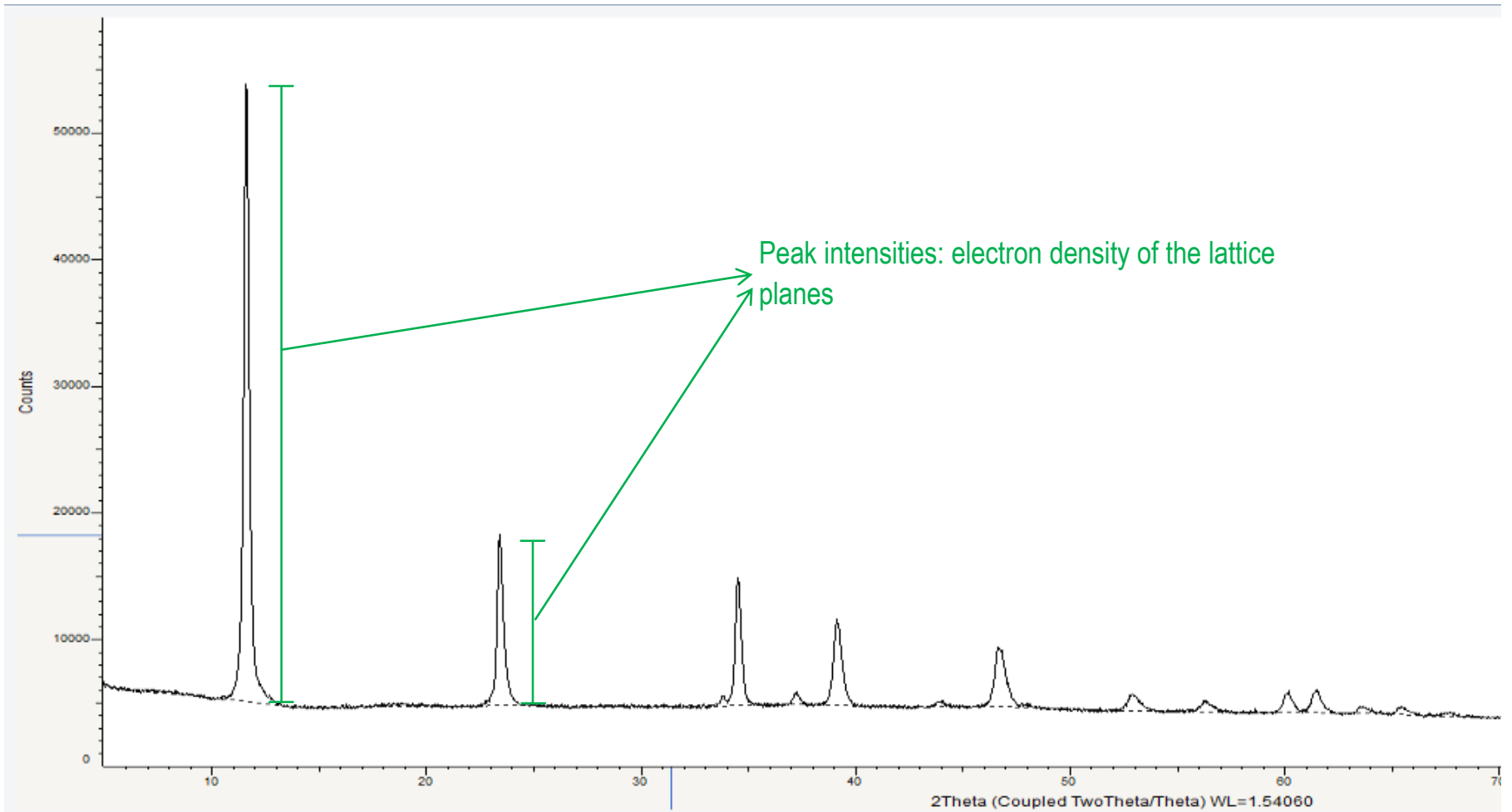
$$\text{Error} = 0.34 \text{ \AA}$$

$$2\theta = 50^\circ, \theta = 25^\circ, d = \lambda/2\sin\theta = 1.823 \text{ \AA}$$

$$2\theta = 50.1^\circ, \theta = 25.05^\circ, d = \lambda/2\sin\theta = 1.819 \text{ \AA}$$

$$\text{Error} = 0.004 \text{ \AA}$$

What does a PXRD pattern tell us?

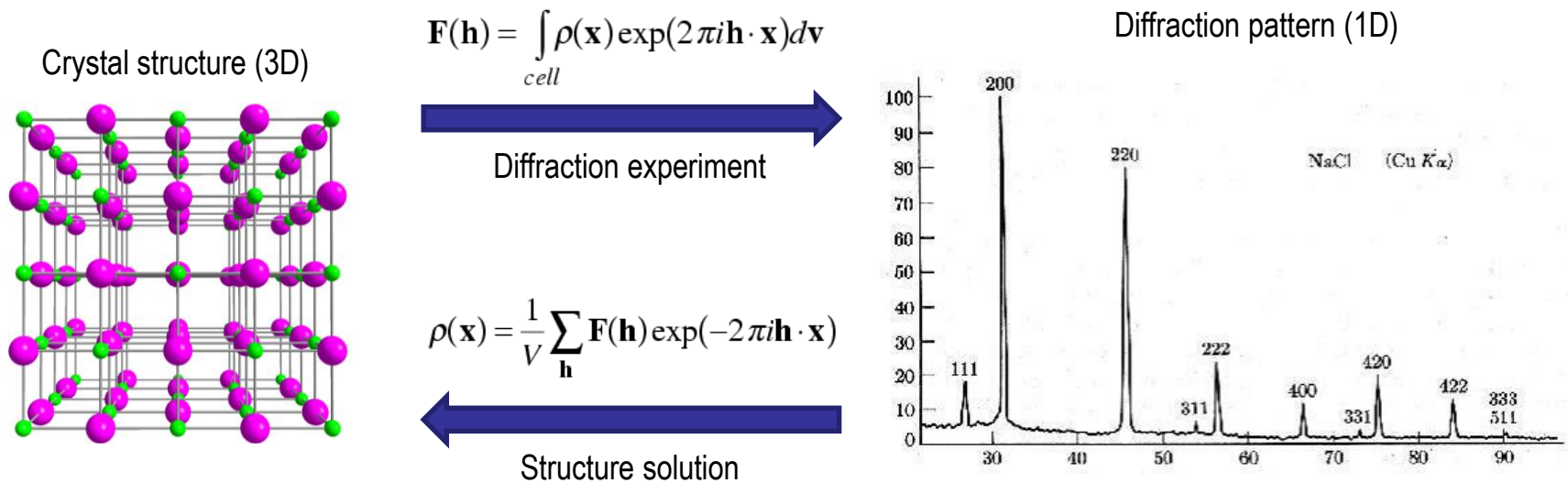


Diffraction by Polycrystalline Solids

The **measured intensity** of Bragg reflections is the result of many contributions, the most important being the **structure factor**, which is a mathematical function describing the **amplitude and phase** of a wave diffracted from crystal lattice planes characterized by Miller indices h,k,l .

The structure factor is the measurable form of the **electron density** of a crystallographic plane, which is the actual physical entity generating the diffraction phenomenon. There are three major factors contributing to the electron density of a plane: the **occupation factor**, the **temperature factor**, and the **atomic scattering factor**.

Structure factor and electron density are mathematically related: they can be converted one into the other by means of a **Fourier transform**.



Solving a crystal structure consists in retrieving the electron density distribution inside the unit cell from the observed structure factors. The information provided by a diffraction experiment is limited to the amplitude of the structure factors, whereas the phase is lost, meaning that we have no spatial information.

There are two main approaches to solve crystal structures: direct methods and real space global optimization methods.

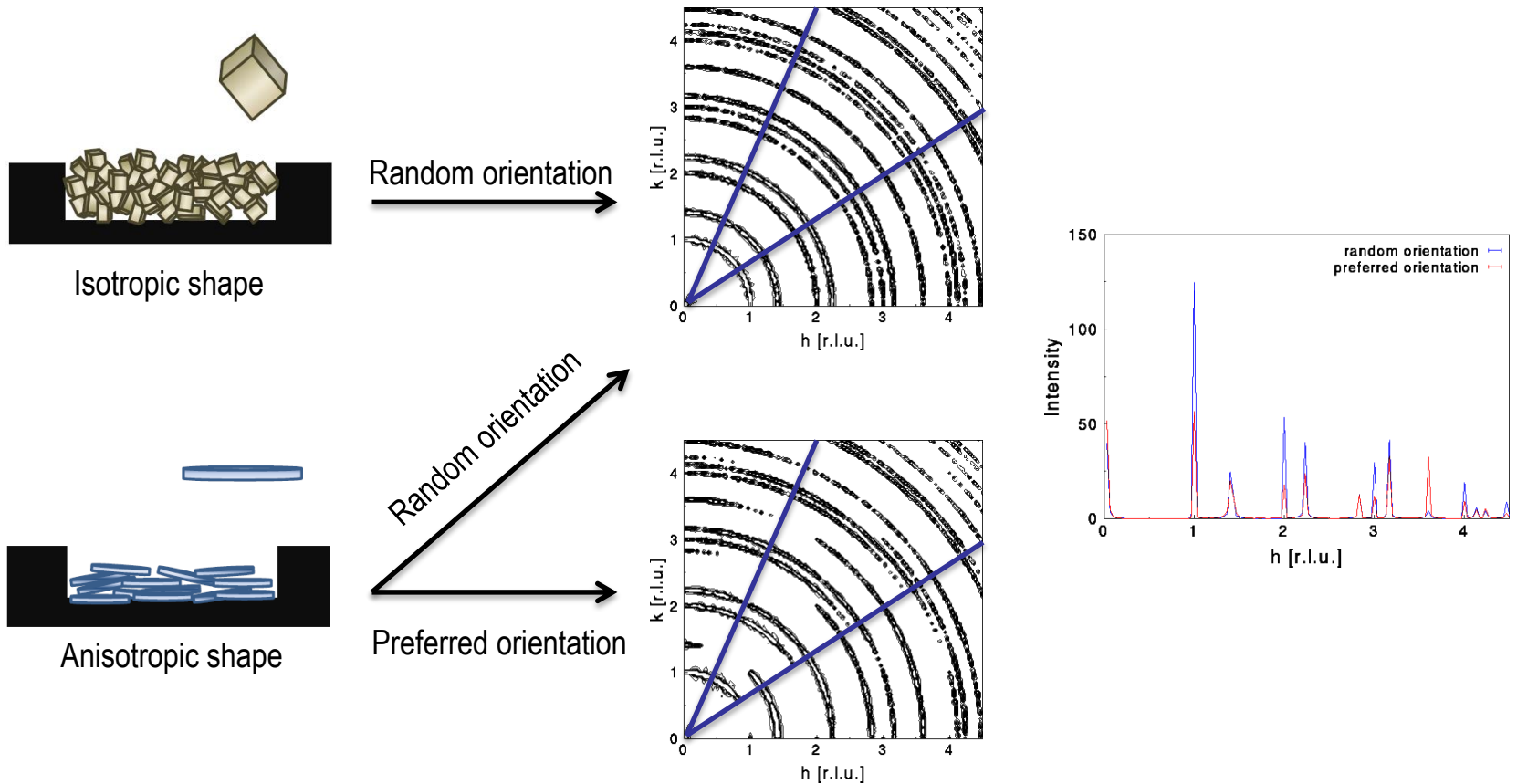
Direct methods (implemented in the program **EXPO**) were initially developed to solve structures from single crystal data and successively adapted to PXRD data. They rely on the intensities extracted by WPPF to retrieve information about the phases of structure factors and are based on two main general assumptions: **the map of electron density is always positive and the atomicity**, that is, the electron density is not uniformly distributed in the unit cell, but is more concentrated nearby the atomic positions. Direct methods work best when the only available information is the observed profile and the unit cell content, and no a priori model can be hypothesized.

Real space global optimization methods (implemented in the program **FOX**) require a priori knowledge of the building blocks constituting the crystal structure, besides the unit cell content. They basically exploit **simulated annealing** algorithms, varying the set of degrees of freedom, both internal (torsion angles) and external (rotational and translational), of the molecular models inside the unit cell, in search of the best configuration, that is the one generating the calculated pattern most similar to the experimental pattern.

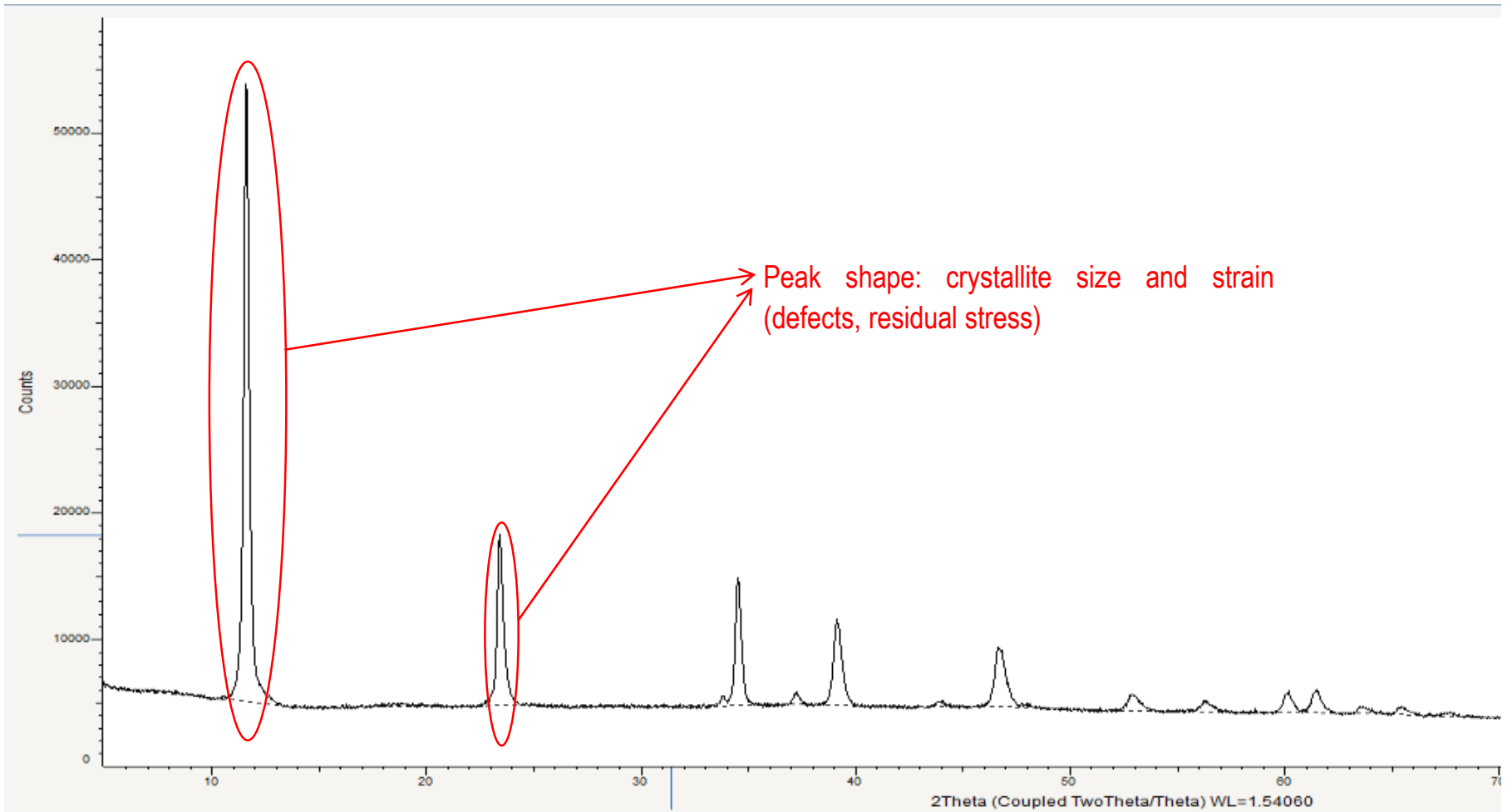
Direct methods and real space global optimization methods can be used in combination, for example when a structure is constituted of heavy metal atoms and organic molecules: direct methods can identify the positions of the metal atoms thanks to their high electron density, while real space global optimization methods can look for the arrangement of the organic molecules around these metal atoms.

Diffraction by Polycrystalline Solids

Preferred orientation of crystallites is one of the main factors generating errors in the measured intensities. Certain anisotropic crystal shapes favor stacking in a particular way (e.g. needles or plate-like). As a consequence, not all crystal orientations will be present in the sample and the intensity distribution will be different from the expected. Preferred orientation can be minimized by carefully preparing the sample.



What does a PXRD pattern tell us?



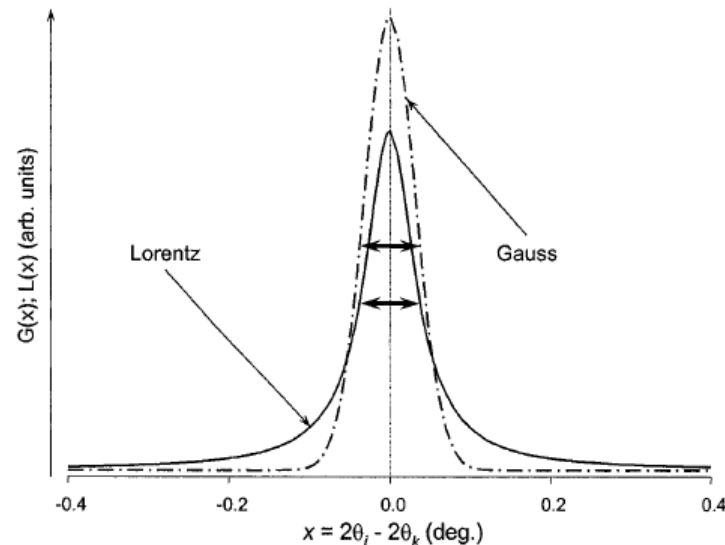
Diffraction by Polycrystalline Solids

In an ideal diffraction experiment carried out on a perfect crystal (incommensurate size and no defects), a reflection would be a sharp line, whose intensity is solely represented by its height, but in a real diffraction experiment it appears as a **broadened peak**.

The shape of bragg peaks can be best described by convolving a **gaussian** function (no tails at the base and has a rounded maximum) and a **lorentzian** function (sharp near its maximum but has long tails on each side near its base).

Both functions are centrosymmetric, but a certain degree of **asymmetry** (mainly due to instrumental factors) is always observed in experimental data and must be taken into account when the profile is fitted.

Peak broadening is the result of both sample and instrumental contributions.



Typical profile functions:

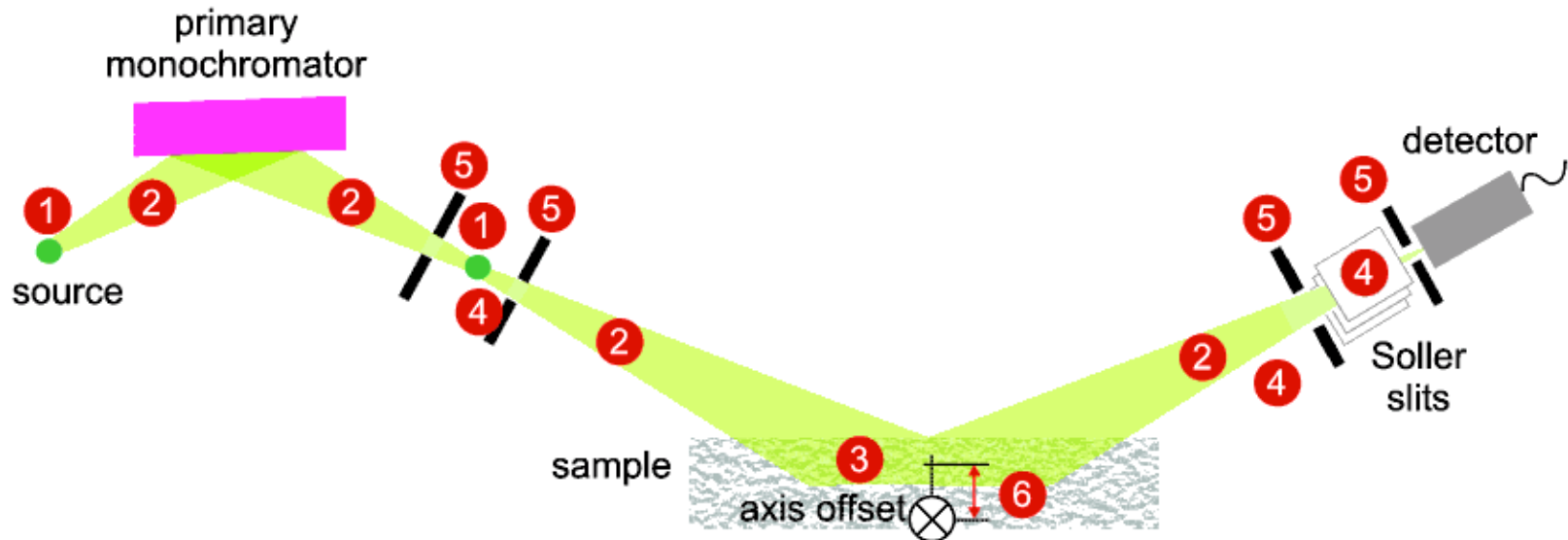
Pseudo-Voigt (linear combination)

Pearson VII (exponential mixing)

Diffraction by Polycrystalline Solids

The **instrumental profile function** can be determined by measuring a **reference material** having ideal structure (normally LaB_6).

Once the instrumental contribution has been identified, the broadening due to the sample can easily be isolated.



Sources of instrumental broadening:

1. the source of radiation (X-rays or neutrons) has a finite physical size (i.e. is not a perfectly sharp spot or line);
2. the radiation is not perfectly monochromatic, but rather consists of a small range, $\delta\lambda$, of wavelengths around the mean, λ
3. the active diffracting volume within the sample is finite and therefore diffraction occurs away from the true centre of the diffractometer
4. axial divergence of the incident/diffracted beams
5. the configuration of defining slits used in the diffractometer
6. any misalignment of the diffractometer

Diffraction by Polycrystalline Solids

Sample contributions to the peak broadening arise from two features: crystallite size and strain.

Crystallite size broadening is due to the limited number of diffracting lattice planes of a real crystal: **the smaller the crystal**, the fewer the lattice planes, **the broader the peak**. Crystallite size is a measure of the size of a coherently diffracting domain. Due to the presence of polycrystalline aggregates, crystallite size is not generally the same thing as particle size.

Strain can be due to different types of structural defects: **extended defects** (such as stacking faults, dislocations, antiphase boundaries) disrupt the atomic arrangement of a crystal, typically along a 2D plane and effectively terminate a crystallographically ordered domain of the crystal; **point defects** (such as site vacancies or interstitial defects) can lead to systematic shifts of atoms from their ideal positions.

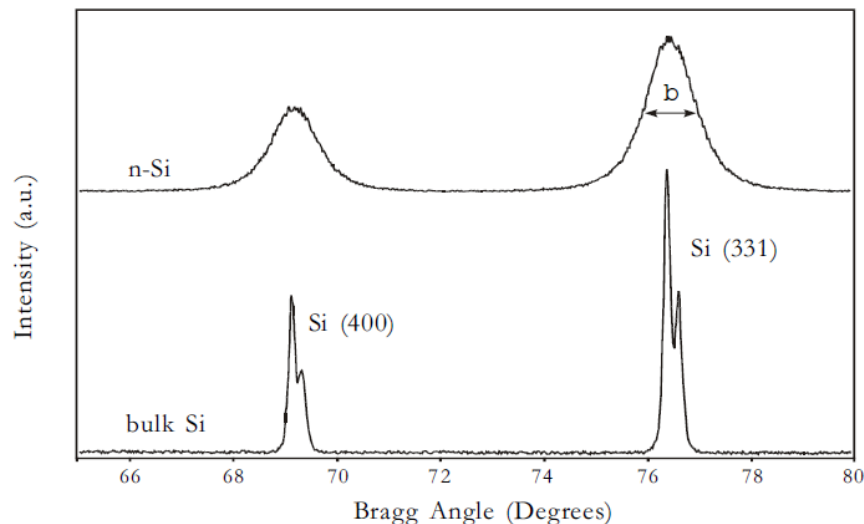


Figure 1 Diffraction patterns of nanocrystalline silicon showing broadening because of particle size.

$$B(2\theta) = \frac{K\lambda}{L \cos \theta}$$

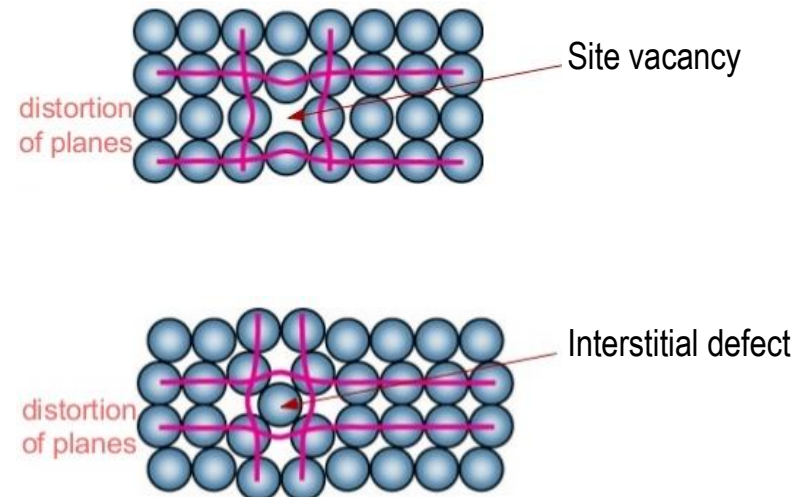
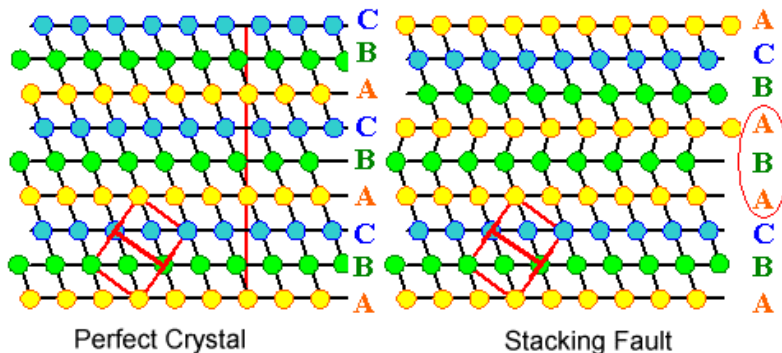
The Scherrer equation defines the inverse proportionality relationship between peak broadening (**B**) and crystal size (**L**).

Diffraction by Polycrystalline Solids

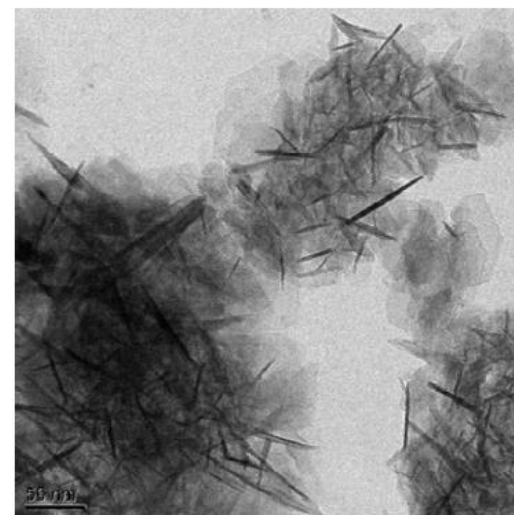
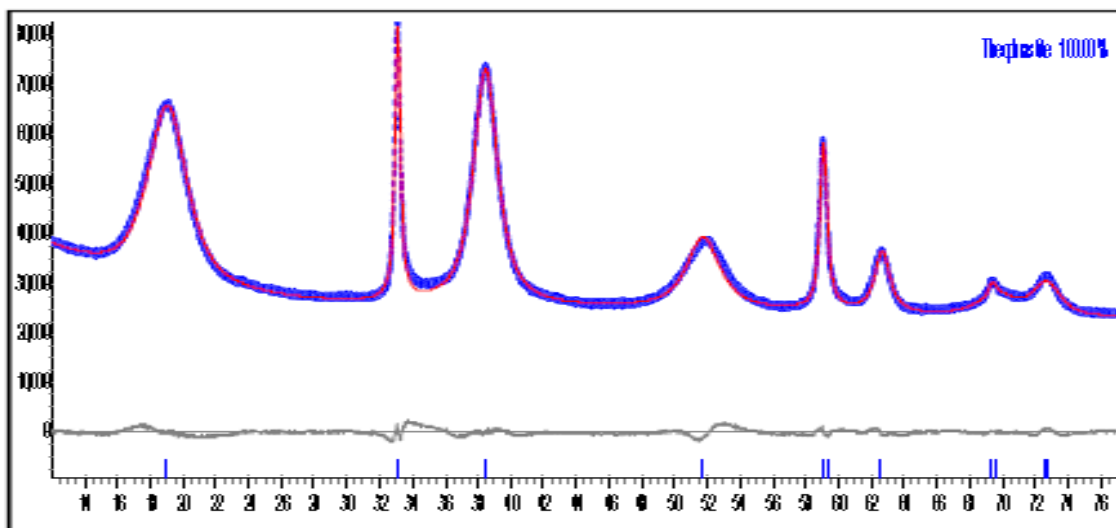
Sample contributions to the peak broadening arise from two features: crystallite size and strain.

Crystallite size broadening is due to the limited number of diffracting lattice planes of a real crystal: **the smaller the crystal**, the fewer the lattice planes, **the broader the peak**. Crystallite size is a measure of the size of a coherently diffracting domain. Due to the presence of polycrystalline aggregates, crystallite size is not generally the same thing as particle size.

Strain can be due to different types of structural defects: **extended defects** (such as stacking faults, dislocations, antiphase boundaries) disrupt the atomic arrangement of a crystal, typically along a 2D plane and effectively terminate a crystallographically ordered domain of the crystal; **point defects** (such as site vacancies or interstitial defects) can lead to systematic shifts of atoms from their ideal positions.

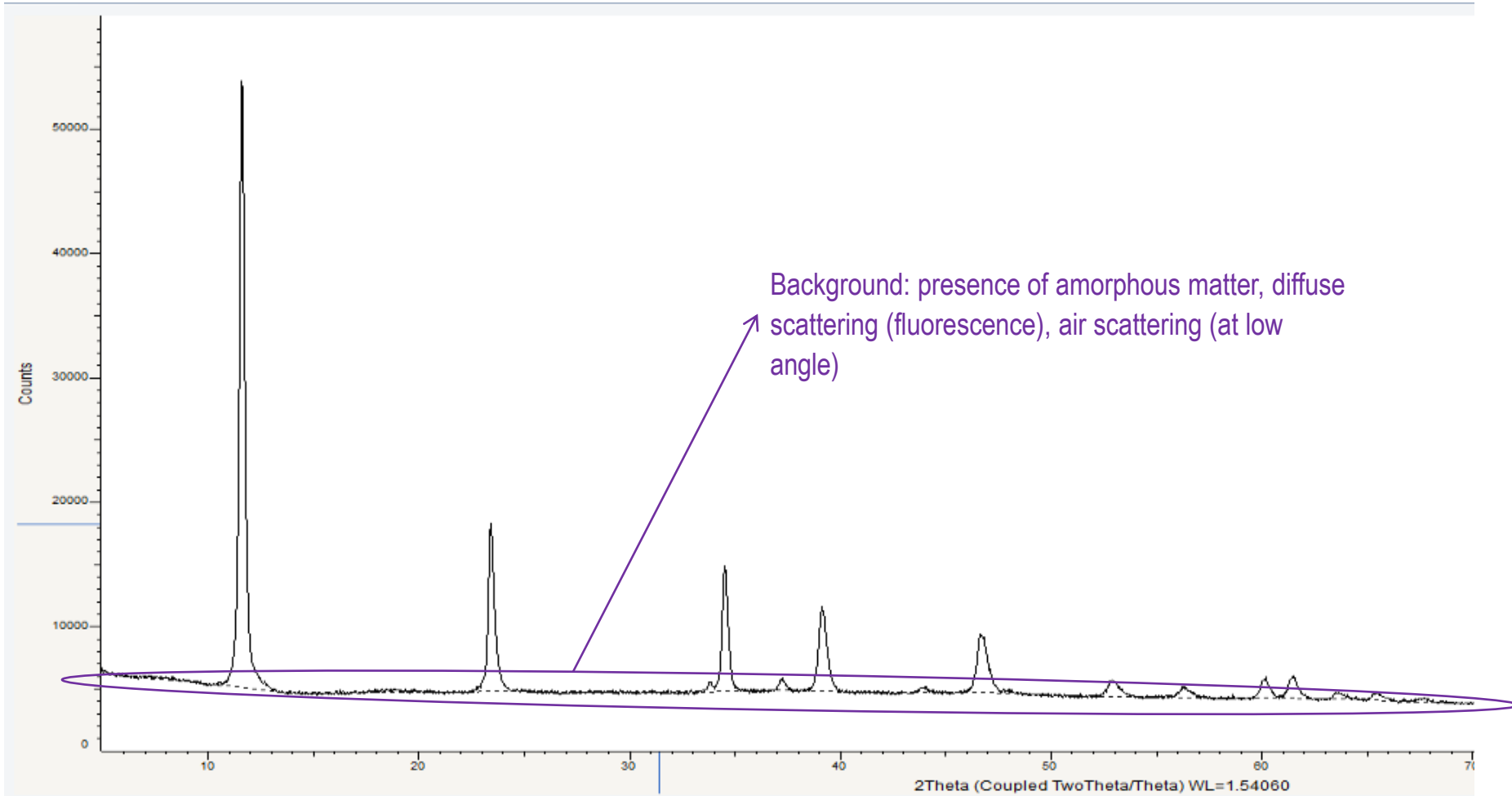


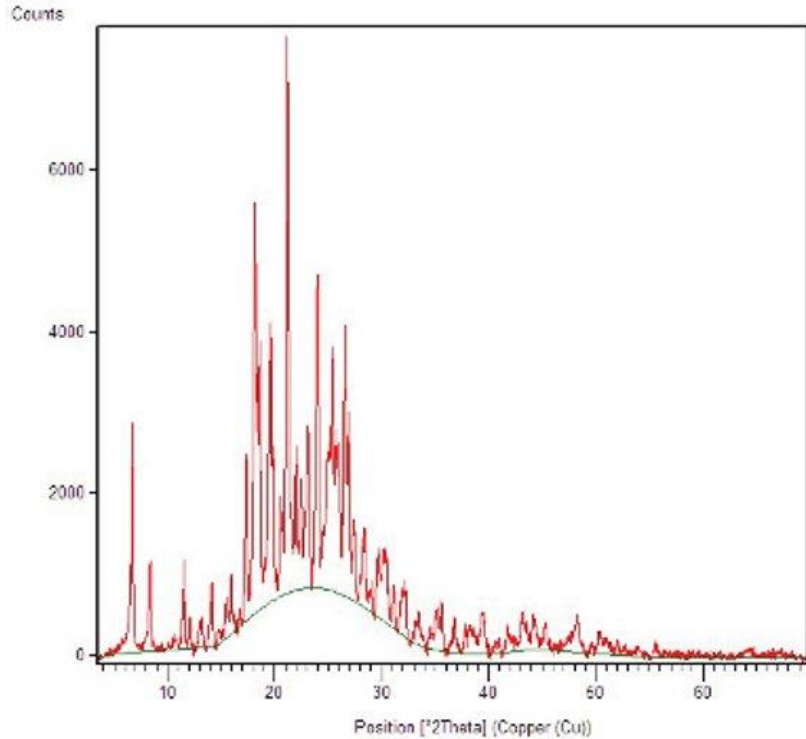
Anisotropic broadening can appear for samples constituted of crystallites having limited size in one or two dimensions. As a consequence, in some directions there will be less diffracting planes than in others. Accordingly, some reflections will be broader than others.



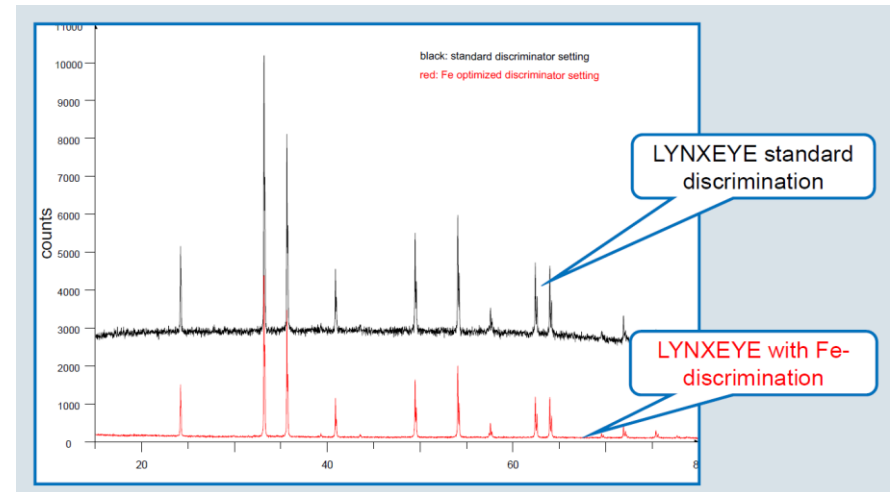
Anisotropic broadening in the PXRD pattern of Ni(OH)₂

What does a PXRD pattern tell us?

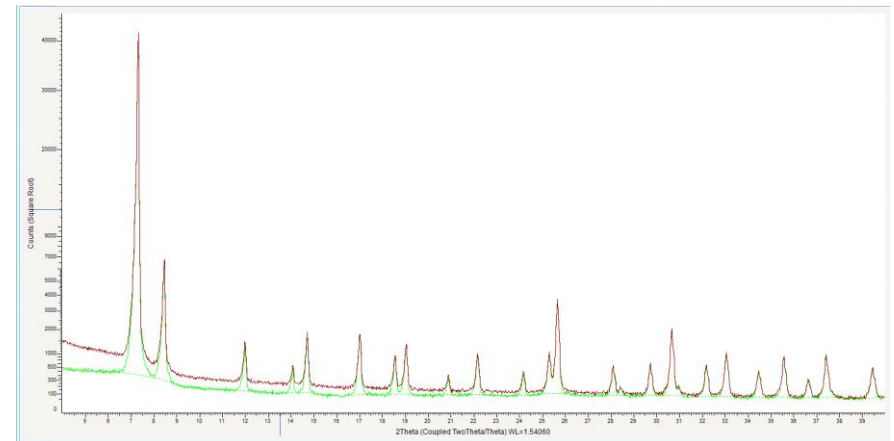




Typical bump in the background due to the presence of amorphous matter



Fluorescence by a Fe-containing hematite sample



Pattern of UiO-66 taken with (green line) and without (brown line) the knife edge to reduce air scattering

Diffraction by Polycrystalline Solids

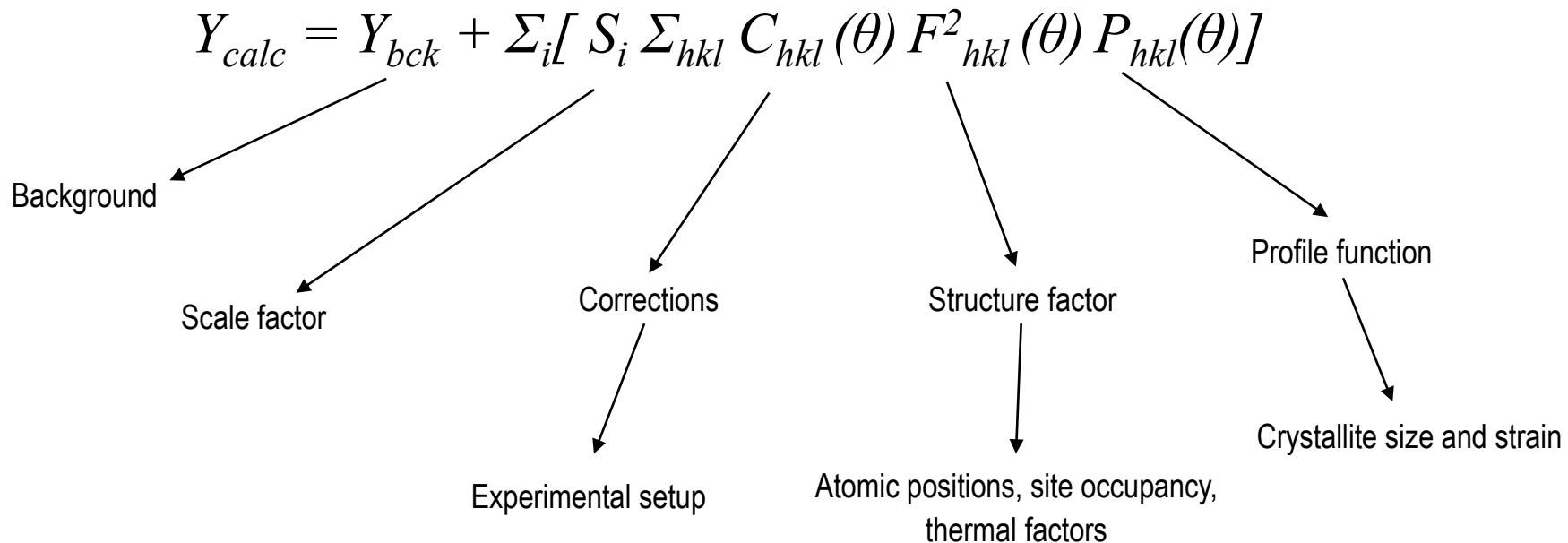
All the features of the diffraction pattern seen before can be simultaneously modeled by means of a full pattern non-linear least squares minimization procedure, known as the **Rietveld method**.

Differently from WPPF methods, the Rietveld method calculates the intensities on the basis of the electron density associated to an atomic structure.

In Rietveld refinement all the measured points of the profile are used as observed parameters and the function minimized during the refinement is the following:

$$S_Y = \sum (w(Y_{obs} - Y_{calc})^2)$$





The calculated intensities are the result of the following contributions:



Diffraction by Polycrystalline Solids

Which information can be extracted from a PXRD pattern?

How?

- Unit cell  Indexing methods – WPPF (Pawley – Le Bail)
 - Qualitative phase analysis  Search/match routines – Structural database
 - Structure solution  Real space global optimization methods (FOX)
– Direct methods (EXPO)
 - Structure refinement
 - Quantitative phase analysis (including amorphous content)
 - Microstructural analysis (size/strain)
- 
- Rietveld method

XRD alone cannot provide all of the information needed to have a satisfactory description of the system under investigation. The best approach is to combine different techniques that can provide complementary information.

XRD

Analysis of long range order.

Limited to crystalline materials.

Not element specific.

Distinguishes different crystallographic sites.

Averages over different elements on the same crystallographic site.

Distinguishes different crystalline phases.

X-Ray Absorption Spectroscopy (XAS)

Analysis of short range order.

Covers both crystalline and amorphous materials.

Element specific.

Averages over different sites (for the same element).

Distinguishes different elements on the same crystallographic site.

Averages over different phases (containing the same element).

Diffraction by Polycrystalline Solids

XRD alone cannot provide all of the information needed to have a satisfactory description of the system under investigation. The best approach is to combine different techniques that can provide complementary information.

XRD

Averaging over the whole sample.

Limited to larger crystallites (reflection broadening).

Amorphous material invisible.

Usually no beam damage.

Electron Microscopy

Relatively local.

Covers both very small crystallites (a few nm, TEM) and large crystallites (up to several μm , SEM)

Amorphous material visible.

Beam damage possible.

Diffraction by Polycrystalline Solids

XRD alone cannot provide all of the information needed to have a satisfactory description of the system under investigation. The best approach is to combine different techniques that can provide complementary information.

XRD

Interaction with electron shell.

Atomic order only.

Scattering power depends on atomic number.

Cannot distinguish isotopes or neighboring elements in the periodic table.

Light elements hard to localize (hydrogen almost invisible).

Neutron diffraction

Interaction with nucleus.

Atomic and magnetic order.

Scattering power depends on nucleus structure.

Distinguishes isotopes and neighboring elements in the periodic table.

No problem with light elements.

Highlights

- Polycrystalline solids are constituted of many crystallites randomly oriented and are ubiquitous
- The powder diffraction pattern contains information about the unit cell and symmetry, the distribution of the electron density inside the unit cell, the crystallite size and strain
- The information contained in the powder pattern can be extracted using a number of mathematical and computational tools
- The Rietveld method for structure refinement is the ultimate tool for treating PXRD data

In the web (open access):

<http://pd.chem.ucl.ac.uk/pdnn/pdindex.htm#powintro>

<http://www.xtal.iqfr.csic.es/Cristalografia/index-en.html>

On paper (or pdf):

“Fundamentals of Powder Diffraction and Structural Characterization of Materials” by Vitalij K. Pecharsky and Peter Y. Zavalij

Part 2: Applications in Heterogeneous Catalysis

Efficient water splitting over $\text{Na}_{1-x}\text{K}_x\text{TaO}_3$ photocatalysts with cubic perovskite structure

Che-Chia Hu, Yuh-Lang Lee and Hsisheng Teng*

Received 13th October 2010, Accepted 29th November 2010

DOI: 10.1039/c0jm03451g

This study improved the photocatalytic activity of NaTaO_3 by replacing some Na ions in the 12-coordinate sites with larger K ions. $\text{Na}_{1-x}\text{K}_x\text{TaO}_3$ photocatalysts of $x = 0-0.2$ were synthesized by the sol-gel method. K-doping at $x = 0.05$ resulted in rectifying the distorted perovskite NaTaO_3 to a pseudo-cubic phase as well as significantly promoting the photocatalytic activity. The 180° bond angle of Ta-O-Ta in the pseudo-cubic phase may facilitate the separation of photogenerated charges for effective water splitting. Photoluminescence spectroscopic analysis confirmed that the flattened Ta-O-Ta linkage with K-doping suppresses the recombination of photogenerated charges. Further K-doping (with $x > 0.05$) leads to impurity formation, which bends the Ta-O-Ta linkage and creates defect states, lowering the photocatalytic activity of the K-doped NaTaO_3 . This study demonstrates that an appropriate ion replacement to tune the crystal structure can significantly promote electron transport in photocatalysts and thus their activity.

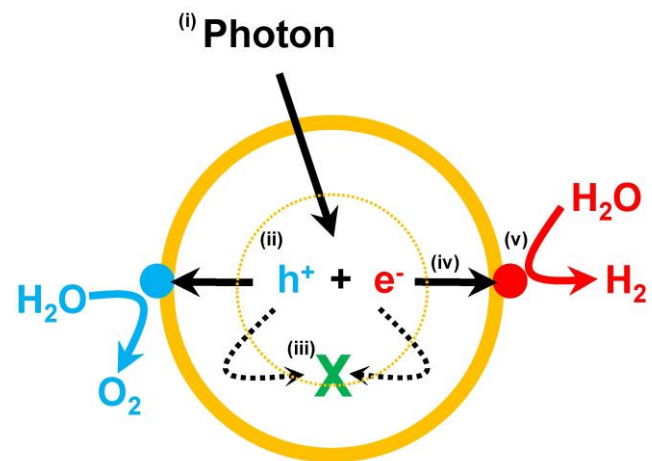
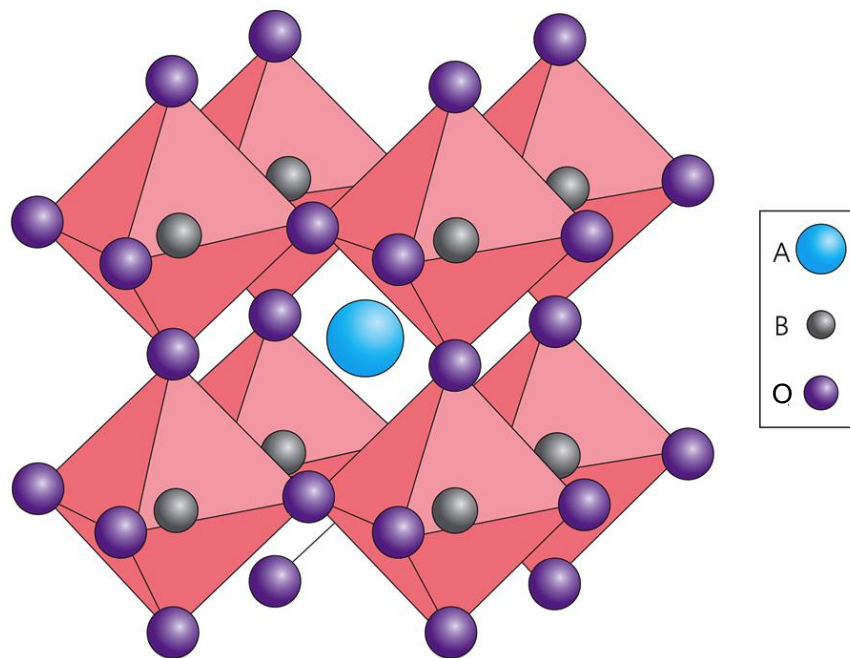
Selected Examples

Perovskites are inorganic solids of general formula ABO_3 , where A is a metal cation having large ionic radius and B is a metal cation having small ionic radius. The crystal structure is constituted of corner-sharing BO_6 octahedra with A ions occupying the interstitial cavities.

$NaTaO_3$ is known to be an active photocatalyst for water splitting under UV illumination, thanks to its ability to efficiently separate photogenerated charges, attributed to the B-O-B angle close to 180° .

The A site in $NaTaO_3$ is larger than required for Na ions, with the consequence that TaO_6 octahedra are slightly tilted to reduce the size of the A site.

Introduction of a larger cation, such as K, can rectify the structure and improve the photocatalytic activity.



Selected Examples

Doped $\text{Na}_{1-x}\text{K}_x\text{TaO}_3$ materials were prepared varying the amount of K from 0 to 0.5. At $x > 0.2$ the $\text{K}_2\text{Ta}_2\text{O}_6$ phase appears, meaning that the perovskite structure can include only a certain amount of K ions before undergoing phase transition.

Rietveld refinements were performed on patterns collected with a laboratory diffractometer.

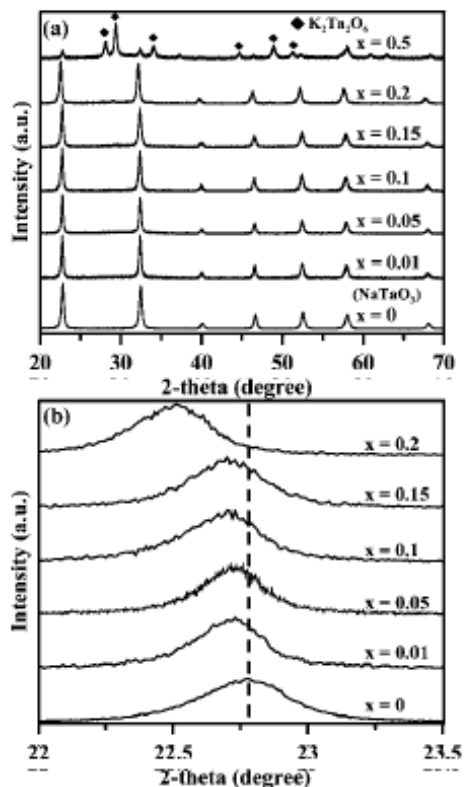


Fig. 1 Powder XRD patterns of the $\text{Na}_{1-x}\text{K}_x\text{TaO}_3$ catalysts with varying K contents: (a) the full range (20–70°) patterns; (b) the magnification of the diffraction peaks around 22.8°.

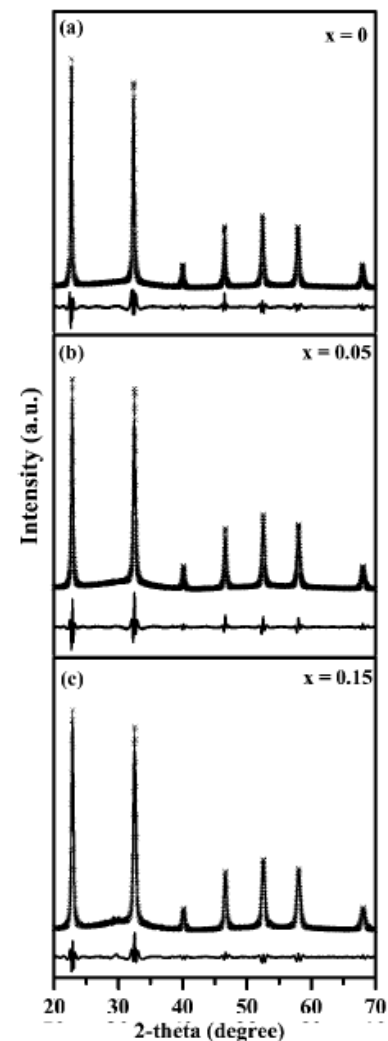


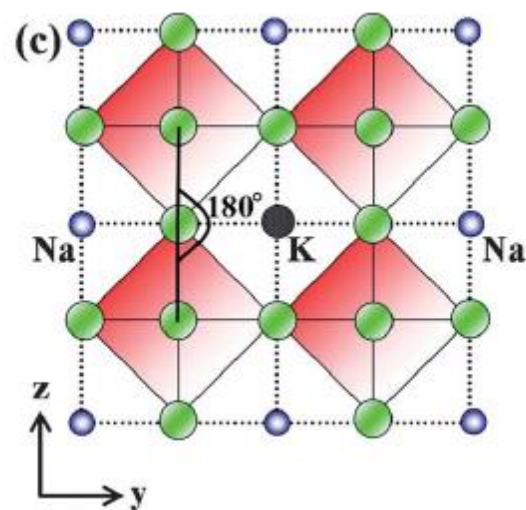
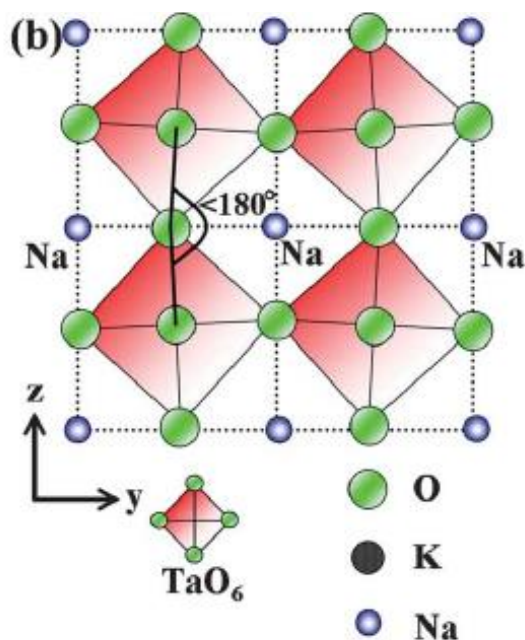
Fig. 3 Observed (×) and Rietveld-refinement simulated (—) XRD profiles for the $\text{Na}_{1-x}\text{K}_x\text{TaO}_3$ catalysts: (a) $x = 0$, with $R_{wp} = 0.087$ and $R_p = 0.074$; (b) $x = 0.05$, with $R_{wp} = 0.106$ and $R_p = 0.091$; (c) $x = 0.15$, with $R_{wp} = 0.066$ and $R_p = 0.057$. The difference between the observed and simulated data is displayed near the bottom of the graphs.

Selected Examples

Table 1 Rietveld refinement results for the $\text{Na}_{1-x}\text{K}_x\text{TaO}_3$ catalysts synthesized with varying x values based on the monoclinic crystal system with the space group $P2_1/m$

x , doping	Occupancy ^a		Coordinates ^b									Ta–O–Ta bond angle
	Na	K	O1			O2			O3			
			x	y	z	x	y	z	x	y	z	
0	0.935	0	0.495	0	0.496	0	0.501	0.502	0.497	0.495	0	179
0.01	0.893	0.008	0.499	0	0.501	0	0.502	0.504	0.499	0.498	0	179
0.05	0.851	0.048	0.500	0	0.502	0	0.502	0.503	0.501	0.500	0	180
0.1	0.805	0.082	0.503	0	0.505	0	0.506	0.508	0.503	0.504	0	178
0.15	0.732	0.124	0.505	0	0.506	0	0.507	0.508	0.506	0.506	0	178
0.2	0.714	0.179	0.508	0	0.509	0	0.508	0.510	0.506	0.507	0	177

^a The occupancy of Ta and O are both set at 1. ^b Na, K ions are set at (0,0,0) randomly, and Ta ions are at $(\frac{1}{2}, \frac{1}{2}, \frac{1}{2})$.



The sample containing 5% of K turns out to be the most active catalyst for the water splitting reaction. This suggests that the Ta-O-Ta angle effectively influences the recombination of the electron-hole pair.

Samples with a higher content of K have an increased amount of vacancy defects, which have a negative impact on the catalytic activity, promoting the recombination.

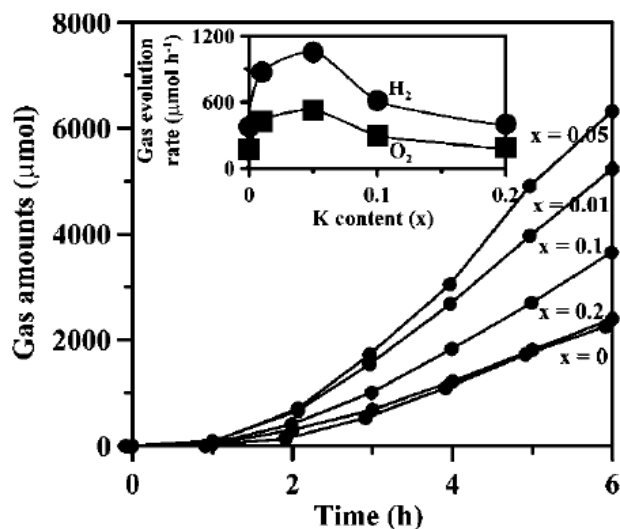


Fig. 6 Time course of photocatalytic H₂ evolution from 1100 mL pure water suspended with 0.1 g of the Na_{1-x}K_xTaO₃ catalysts under mercury lamp irradiation. The inset shows the dependence of the H₂ and O₂ evolution rates on the K content.

J | A | C | S

A | R | T | I | C | L | E | S

Published on Web 12/15/2009

In Situ XAS and XRPD Parametric Rietveld Refinement To Understand Dealumination of Y Zeolite Catalyst

Giovanni Agostini,[†] Carlo Lamberti,^{*,†} Luca Palin,[‡] Marco Milanese,[‡]
Nadiya Danilina,^{||} Bin Xu,^{||} Markus Janousch,[§] and Jeroen A. van Bokhoven^{*,||}

Department of Inorganic, Materials and Physical Chemistry, Torino University, Via P. Giuria 7, 10125 Turin, Italy, INSTM Unità di Torino Università, Turin, Italy, NIS Centre of Excellence, Università di Torino, Italy, Dipartimento di Scienze e Tecnologie Avanzate and Nano-SiSTeMI Interdisciplinary Centre, Università del Piemonte Orientale "A. Avogadro", Via T. Michel 11, 15121 Alessandria, Italy, Swiss Light Source, Paul Scherrer Institut, 5232 Villigen PSI, Switzerland, and ETH Zurich, Institute for Chemical and Bioengineering, HCI E127 8093 Zurich, Switzerland

Received September 10, 2009; E-mail: carlo.lamberti@unito.it; j.a.vanbokhoven@chem.ethz.ch

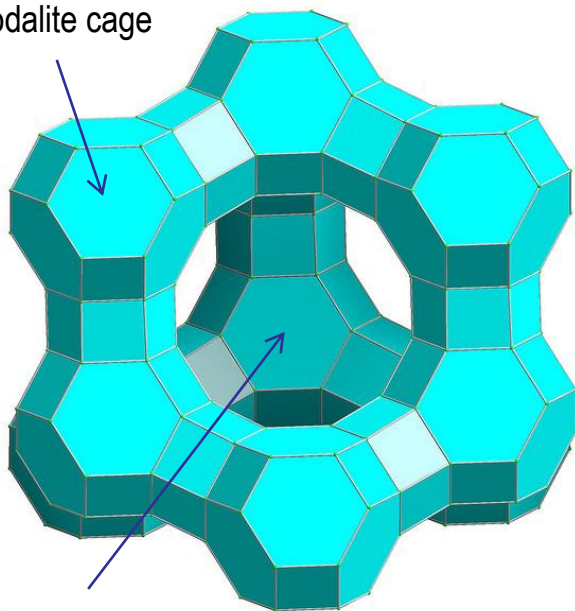
Abstract: Dealumination of NH₄-Y zeolite during steaming to 873 K was investigated with in situ, time-dependent, synchrotron radiation XRPD and in situ Al K-edge XAS. Water desorption is complete at 450 K, and ammonium decomposition occurs between 500 and 550 K. Only a small fraction of Al³⁺ species (5%) leaves the framework during heating from 710 to 873 K; these species occupy site I' inside the sodalite cage. This fraction increases up to 8% in the first 50 min at 873 K and remains constant for the following 70 min isotherm and during the high-temperature part of the cooling experiment. During cooling from 500 to 450 K, the electron density at site I' increases suddenly, corresponding to a fraction of 30–35% of the total Al, confirmed by ex situ ²⁷Al MAS solid-state NMR. At that temperature, in situ Al K-edge XAS indicates a change in Al coordination of a large fraction of Al, and thermogravimetric (TG) data show the first water molecules start to repopulate the pores. Such molecules drive the dislodgment of most of the Al from the zeolitic framework. Our data indicate that considerable structural collapse caused by steaming does not occur at the highest temperature; however, defects form, which lead to significant migration of framework Al³⁺ to extraframework positions, which occurs only as water is able to enter the pores again, that is, at much lower temperature. Contrary to general opinion, these results demonstrate that zeolite dealumination is not primarily a high-temperature process. The standard Rietveld refinement approach failed to identify extraframework Al species. These new results were obtained by adopting the innovative parametric refinement [*J. Appl. Crystallogr.* **2007**, *40*, 87]. Treating all of the XRPD patterns collected during the evolution of temperature as one unique data set significantly reduces the overall number of optimized variables and, thus, their relative correlation, and finally results in a more reliable estimate of the optimized parameters. Our results contribute to a better understanding of the phenomena involved on the atomic scale in the preparation of ultrastable Y zeolites (USY). USY are employed in fluid catalytic cracking (FCC), which is the most important conversion process in petroleum refineries to convert the high-boiling hydrocarbon fractions of petroleum crude oils to more valuable products like gasoline and olefinic gases.

Selected Examples

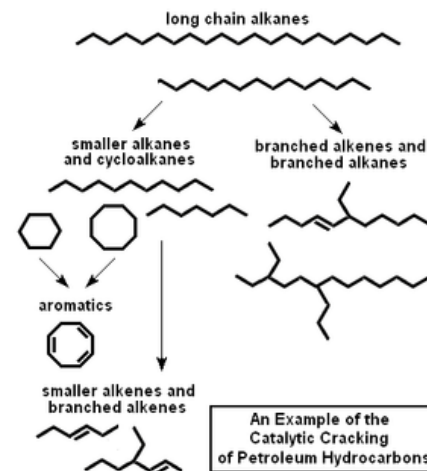
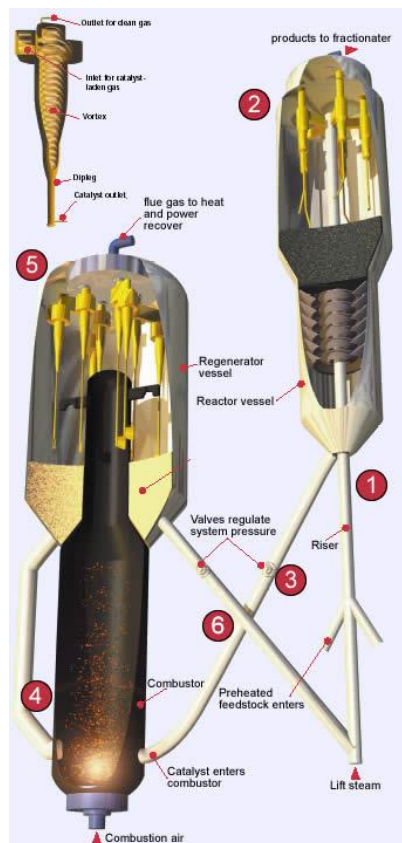
Zeolites are microporous crystalline silica-alumina frameworks widely employed in the chemical industry as acidic catalysts.

Prolonged steaming of zeolite tipe Y leads to partial dealumination of the framework, removing the most unstable Al^{3+} species and creating mesoporosity. The resultant material is termed ultra stable zeolite Y (USY) and is a widely used catalyst in several industrial processes, the most important being fluid catalytic cracking (FCC) of the high-boiling hydrocarbon fraction of petroleum crude oil.

Sodalite cage



Supercage



Selected Examples

PXRD patterns of a sample of zeolite NH_4Y with a 2.6 Si/Al ratio at 300 K, heated at 873 K and subsequently cooled again to 300 K were collected with synchrotron radiation and refined with the Rietveld method. Upon heating, water and ammonium ions are removed and 8% of the Al atoms migrate to the extraframework site I'. Cooling down to 300 K, water is readsorbed and additional 34% of total Al atoms leave the framework.

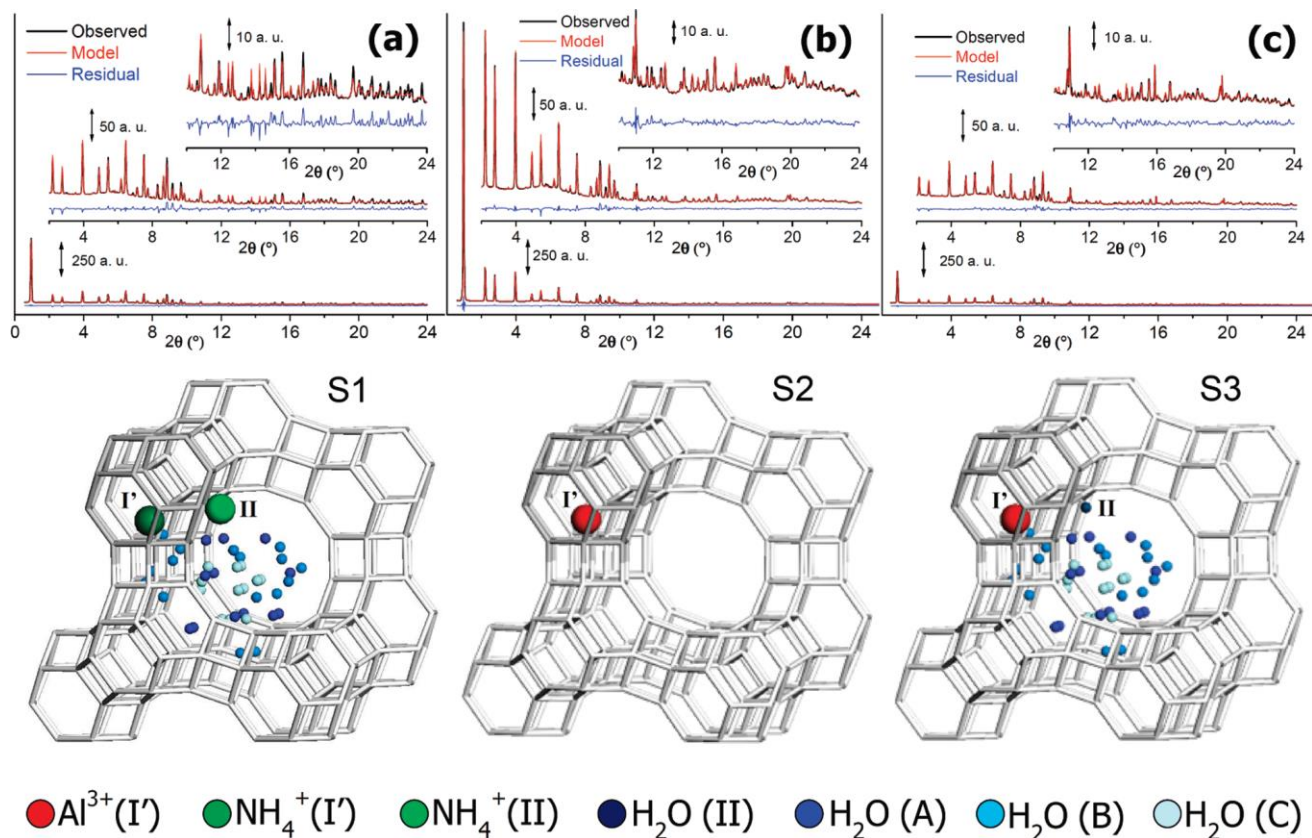


Figure 1. Refinements (top) and relative models (bottom) for the XRPD data, collected at various temperatures: 300 K, S1 (a); 873 K, S2 (b); 300 K, S3 (c). Top: Observed (black), calculated (red), and residual (blue) profiles. The zooms highlight the 2–24° and 10–24° 2θ regions to illustrate the quality of the data and the refinement. Bottom: Sticks representation of the Y zeolite framework showing one supercage and several sodalite cages together with the refined extraframework (I', II) and water (A, B, and C) sites according to the models used in the refinement (Tables S1–S3 of the Supporting Information).

Selected Examples

In situ PXRD analysis was performed while heating the sample from 300 K up to 873 K and subsequently cooling it down to 300 K.

The diffraction patterns collected during heating and cooling were first refined by considering each diffractogram as an independent data set. With this approach, the parameters that behaved in a physically predictable manner during the dynamic experiment were identified: they were the scale factor and the coordinates of the framework atoms. The variation in such parameters was then parametrized according to $P(i) = a*i + P_0$, where i represents the number of diffractograms (from 0 to 61), P_0 the starting value of the parameter, and a the slope that defines the variation in the series. With the standard approach, 62 independent $P(i)$ parameters could be optimized as compared to only two (a , P_0) with parametrization. Successively, a second refinement step was executed by adopting the parametrization for the scale factor and the framework atom coordinates. The remaining parameters (cell parameter, extraframework site occupancy, and background factors) were independent during the refinement.

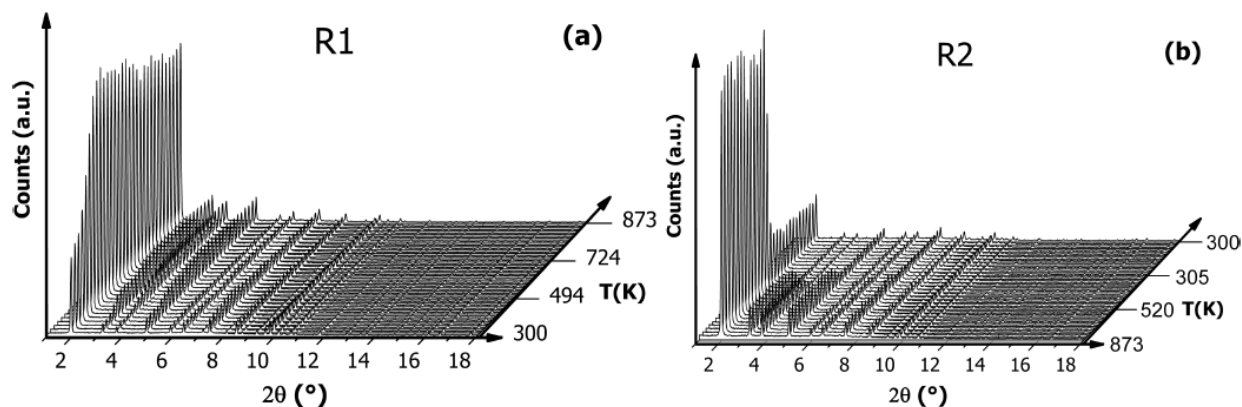
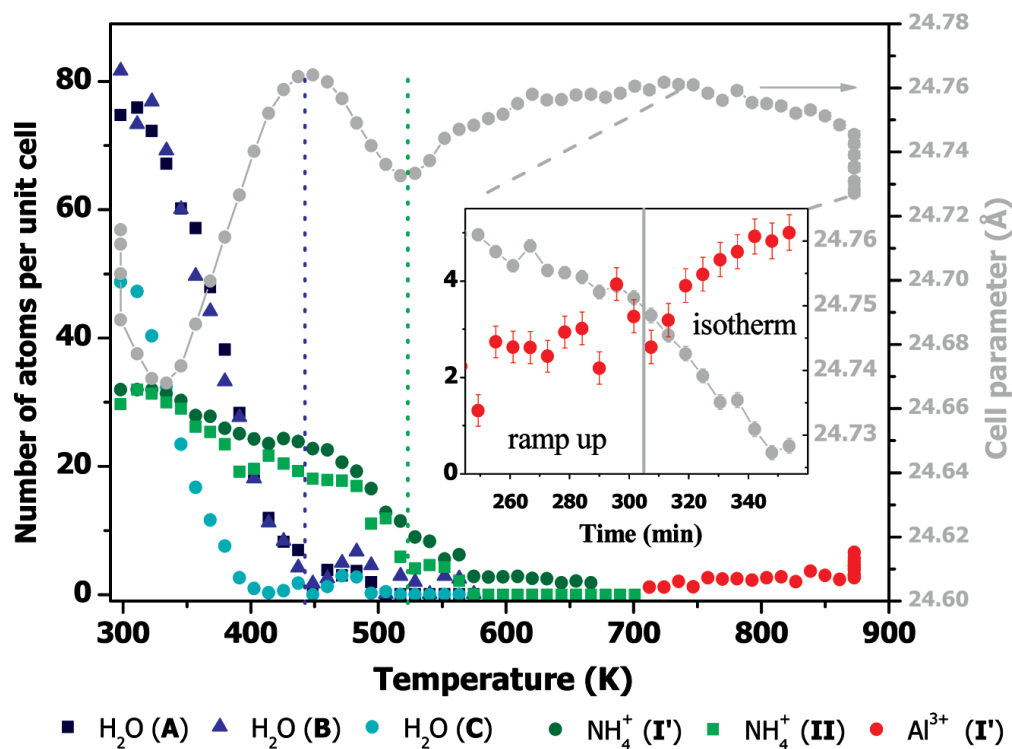


Figure 2. Three-dimensional representation of the XRPD patterns collected during the heating (R1, part a) and cooling (R2, part b) experiments. The decrease in the low θ reflection during R2 (zeolite rehydration) was much more abrupt than the more gradual increase during R1 (zeolite dehydration). R1 was performed with a gradient of $+2 \text{ K/min}^{-1}$, while R2 was performed with a nominal gradient of -4.8 K/min^{-1} : This gradient holds in the high-temperature range only; the sample follows a much smoother, exponential-like temperature decay due to the huge thermal inertia of the gas blower (see text and Supporting Information for more details).

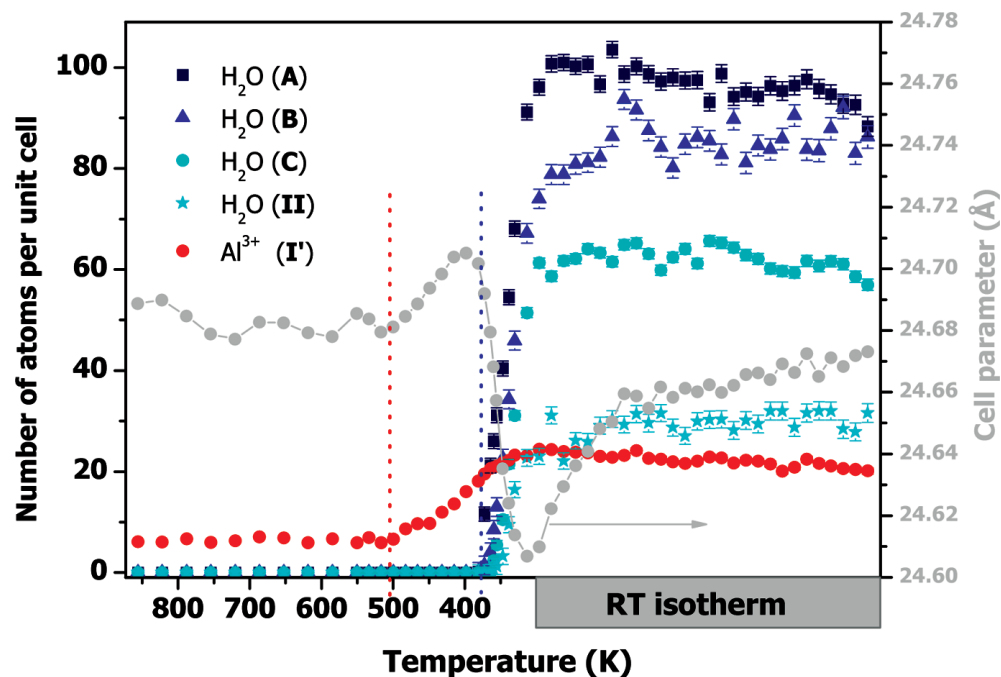
Selected Examples

Water molecules at site C leave the framework first, reaching zero occupancy at around 410 K. Water molecules at sites A and B desorb simultaneously at 450 K. NH_4^+ cations in the supercages are depopulated at 570 K and those in the sodalite cages at 670 K. According to TGA and Rietveld refinement, there is a weight loss of about 30% accompanied by minor changes in the aluminum coordination (evidenced by XAS data). At high temperature, some 3-fold coordinated aluminum probably forms (less than 10%), which populates site I'.



Selected Examples

The main structural changes occur during cooling. XAS shows that down to 393 K about 10% of framework aluminum had changed its coordination and up to 30% during further cooling. Only minor structural changes occur in the presence of moisture at high temperature; a steady state is reached after 40-50 min at 873 K, and the fraction of extraframework Al^{3+} species increases from about 3 to about 6 atoms/unit cell. These defects are probably the starting points of the large structural changes that occur in the cooling experiment after readsorption of water into the pores, with the fraction of extraframework Al^{3+} species increasing to as much as about 30 atoms/unit cell. In other words, Y zeolite has a partially defective phase; its moisture content is very low at high temperature, and it undergoes further and more important dealumination at lower temperature due to the action of water.



Applied Catalysis A: General 479 (2014) 59–69



ELSEVIER

Contents lists available at ScienceDirect

Applied Catalysis A: General

journal homepage: www.elsevier.com/locate/apcata

X-ray absorption, X-ray diffraction and electron microscopy study of spent cobalt based catalyst in semi-commercial scale Fischer–Tropsch synthesis



Nikolaos E. Tsakoumis^{a,*}, Roya Dehghan-Niri^{b,1}, Magnus Rønning^a, John C. Walmsley^{b,d}, Øyvind Borg^c, Erling Rytter^{a,c}, Anders Holmen^a

^a Department of Chemical Engineering, Norwegian University of Science and Technology (NTNU), Sem Sælandsvei 4, NO-7491 Trondheim, Norway

^b Department of Physics, Norwegian University of Science and Technology (NTNU), NO-7491 Trondheim, Norway

^c Statoil RDI, Research Centre Trondheim, Postuttak, NO-7005 Trondheim, Norway

^d SINTEF Materials and Chemistry, NO-7465 Trondheim, Norway

ARTICLE INFO

Article history:

Received 22 January 2014

Received in revised form 17 March 2014

Accepted 27 March 2014

Available online 4 April 2014

Keywords:

Fischer–Tropsch

Cobalt

Deactivation

Sintering

Gas-to-liquid

ABSTRACT

Calcined, reduced and spent Co-Re/ γ -Al₂O₃ catalysts for Fischer–Tropsch synthesis (FTS) were characterized and compared. Co-K-edge and Re-L_{III}-edge X-ray absorption near edge structure (XANES), X-ray powder diffraction (XRPD), transmission electron microscopy (TEM) and H₂ chemisorption were used to provide insight into structural transformations that the catalyst experiences during a month of operation in a semi-commercial FTS plant. Results from the core techniques for nanoparticle size determination suggest that sintering of the cobalt crystallites is an important deactivation mechanism in FTS performed in slurry reactors. In addition, a higher degree of reduction is observed for the spent catalytic material, while Re appears in a partially reduced state before and after reaction. The particle size distribution together with the spread of Co nanoparticles on the γ -Al₂O₃ surface indicates crystallite migration as the prevailing mechanism.

© 2014 Elsevier B.V. All rights reserved.

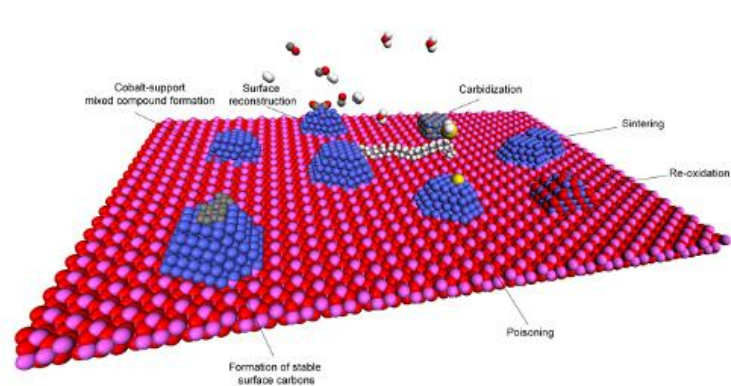
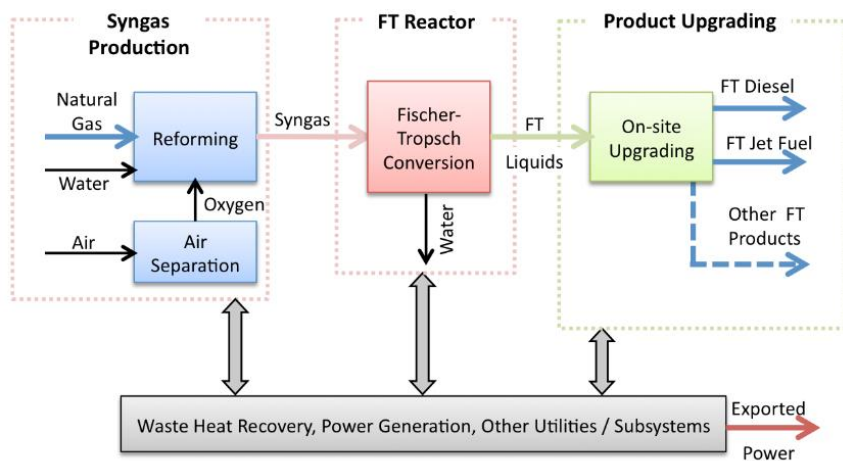
Selected Examples

The gas-to-liquid (GTL) process is the conversion of natural gas derived synthesis gas into hydrocarbons via Fischer–Tropsch synthesis (FTS). The currently commercialized GTL technologies use supported cobalt catalysts for the Fischer–Tropsch synthesis step, in which CO and H₂ are transformed to a wide range of linear long-chain hydrocarbons and water.

One of the challenges in applied Co-based FTS is the lifetime of the catalyst. Due to the relatively high price of cobalt, continuous operation without catalyst replacement for long periods is favourable.

Deactivation of the catalyst has been attributed to various factors: sintering of cobalt particles, formation of inactive cobalt-support mixed phases, and formation of stable carbon species.

A spent Co-Re/ γ -Al₂O₃ catalyst (20 wt% Co, 0.5 wt% Re) operated in a semi-commercial demonstration GTL unit with production capacity of 1000 bpd [16] was analyzed and compared to its fresh analogue.



The fresh catalyst was calcined at 573 K for 16 hours and analyzed by PXRD using synchrotron radiation. Co_3O_4 crystallite size was estimated using the Scherrer formula to be 13.2 nm, which upon loss of oxygen should lead to Co particles of 10.6 nm.

In situ PXRD measurement were performed during a temperature-programmed hydrogenation (TPH) process (heating to 673 K at a 3 K/min rate and 4 h isotherm), showing that Co_3O_4 is initially reduced to CoO, as observed by XAS measurements, and subsequently to Co in face-centered cubic (fcc) arrangement, with evidence of the presence of some Co in hexagonal close-packed (hcp) structure. Crystallite size was estimated to be 7.9 nm.

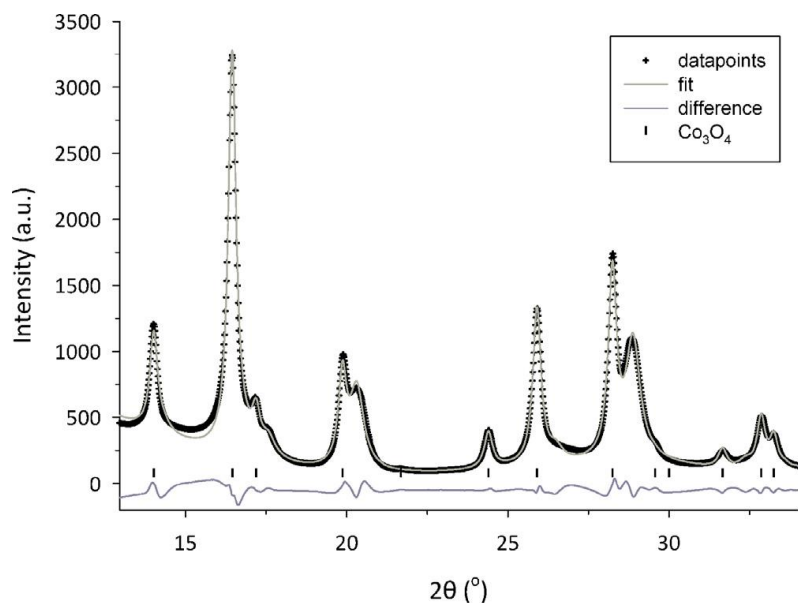


Fig. 4. XRPD pattern of Cat consisting of Co_3O_4 crystallites dispersed on the γ -alumina support, plotted together with the calculated pattern and their difference.

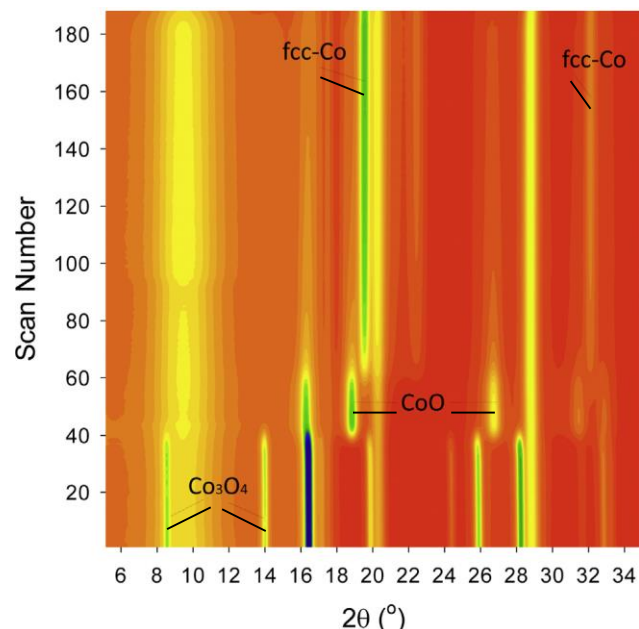
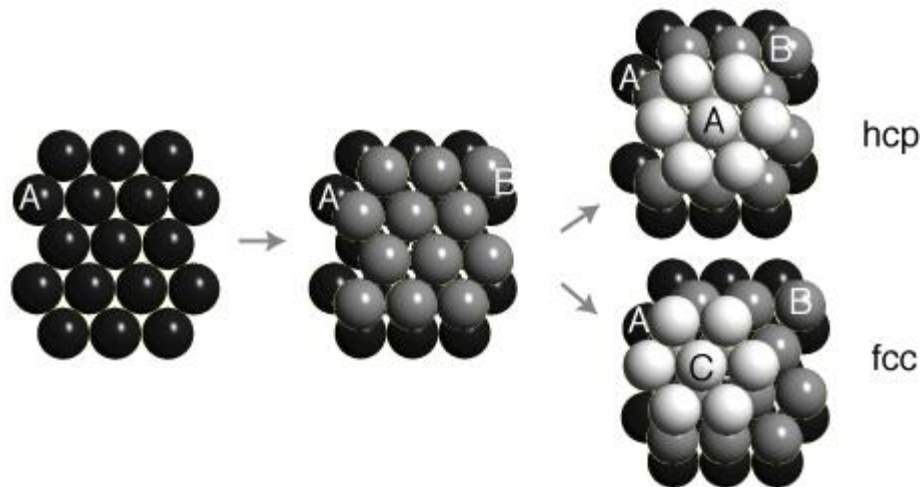


Fig. 5. Intensity monitoring for the reflections (3 1 1) of Co_3O_4 , (2 2 0) of CoO and (1 1 1) from fcc-Co during catalyst reduction.

Selected Examples

The fresh catalyst was calcined at 573 K for 16 hours and analyzed by PXRD using synchrotron radiation. Co_3O_4 crystallite size was estimated using the Scherrer formula to be 13.2 nm, which upon loss of oxygen should lead to Co particles of 10.6 nm.

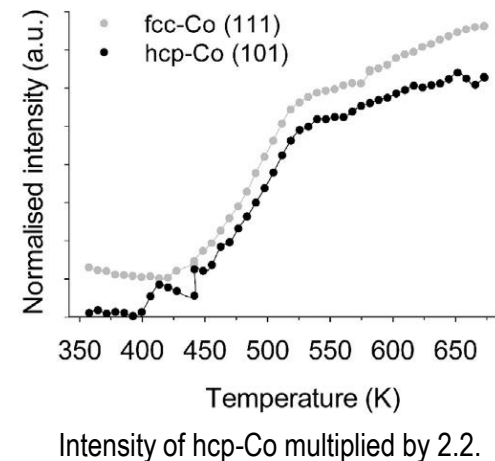
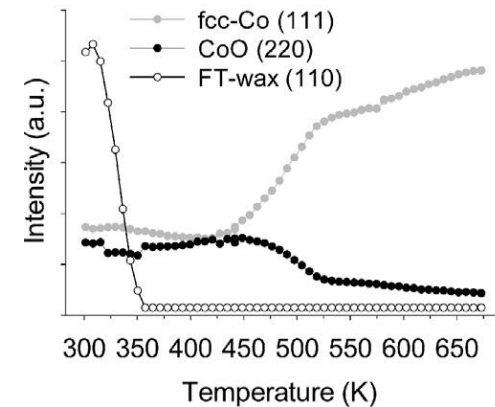
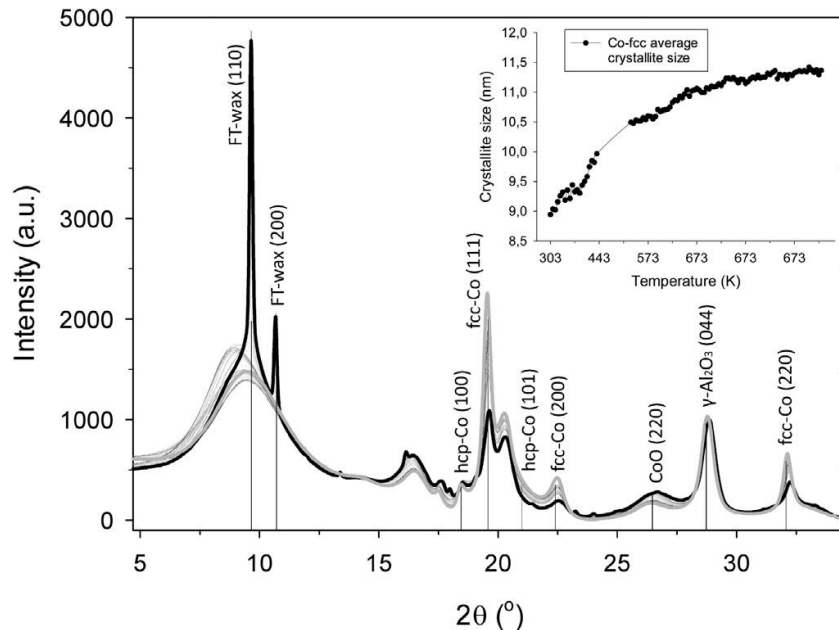
In situ PXRD measurements were performed during a temperature-programmed hydrogenation (TPH) process (heating to 673 K at a 3 K/min rate and 4 h isotherm), showing that Co_3O_4 is initially reduced to CoO , as observed by XAS measurements, and subsequently to Co in face-centered cubic (fcc) arrangement, with evidence of the presence of some Co in hexagonal close-packed (hcp) structure. Crystallite size was estimated to be 7.9 nm.



Selected Examples

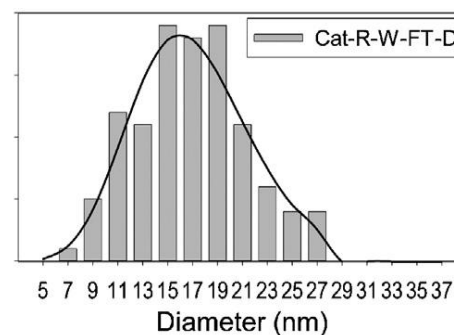
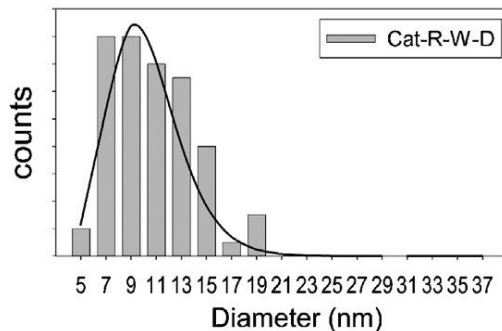
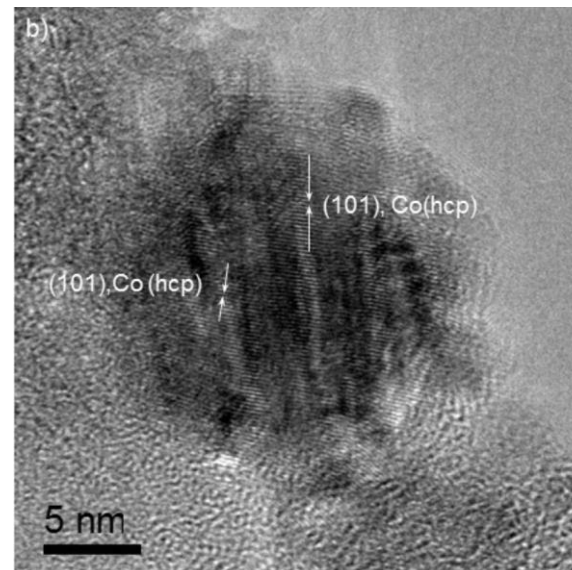
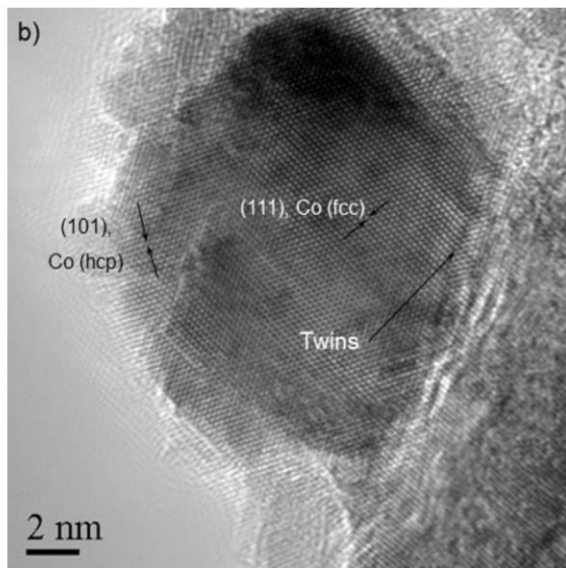
The spent catalyst was first de-waxed and then subjected to the same TPH treatment. Wax is still present in the sample even after de-waxing, but it melts above 313 K and is no more visible. The reflections of fcc-Co start getting sharper at 443 K, at the same time the intensity of the reflections of CoO decreases.

The crystallite size of fcc-Co increases from 8.7 nm to 11.3 nm during the treatment, indicating that sintering happens. Comparing the crystallite size of the fresh and the spent catalyst after the same TPH treatment, a 43% increase is apparent in the spent sample.



Selected Examples

TEM analysis shows that the Co nanoparticles consist of both fcc and hcp regions. Particle size distributions are shifted towards higher diameters than those observed by PXRD (11.5 nm for the fresh catalyst, 16.9 nm for the spent one), but the approximate increase from the fresh to the spent catalyst is 47%, in agreement with that obtained by PXRD.



Journal of Catalysis 305 (2013) 277–289



ELSEVIER

Contents lists available at SciVerse ScienceDirect

Journal of Catalysis

journal homepage: www.elsevier.com/locate/jcat

Molybdenum-based catalysts for the decomposition of ammonia: In situ X-ray diffraction studies, microstructure, and catalytic properties



Valeria Tagliazucca, Klaus Schlichte, Ferdi Schüth, Claudia Weidenthaler*

Max-Planck-Institut für Kohlenforschung, Kaiser-Wilhelm-Platz 1, 45470 Mülheim an der Ruhr, Germany

ARTICLE INFO

Article history:

Received 11 March 2013

Revised 7 May 2013

Accepted 11 May 2013

Available online 29 June 2013

Keywords:

In situ powder diffraction

Ammonia decomposition

Structure analysis

Molybdenum oxides

Molybdenum nitrides

ABSTRACT

The ammonia decomposition reaction over molybdenum-based catalysts is an example for the complex influence of different factors, such as phase composition, size of crystalline domains, or defect concentration, on the catalytic behavior of a material. In situ powder diffraction allows the direct analysis of how catalysts change during a reaction with respect to the atomic structure or microstructure in terms of defects or size changes. In this article, the influence of catalyst treatment such as pre-reduction or ball milling on the catalytic properties is discussed in detail.

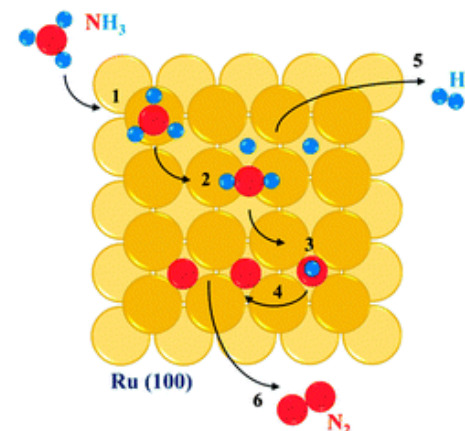
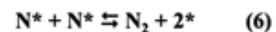
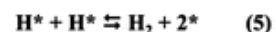
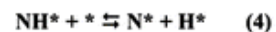
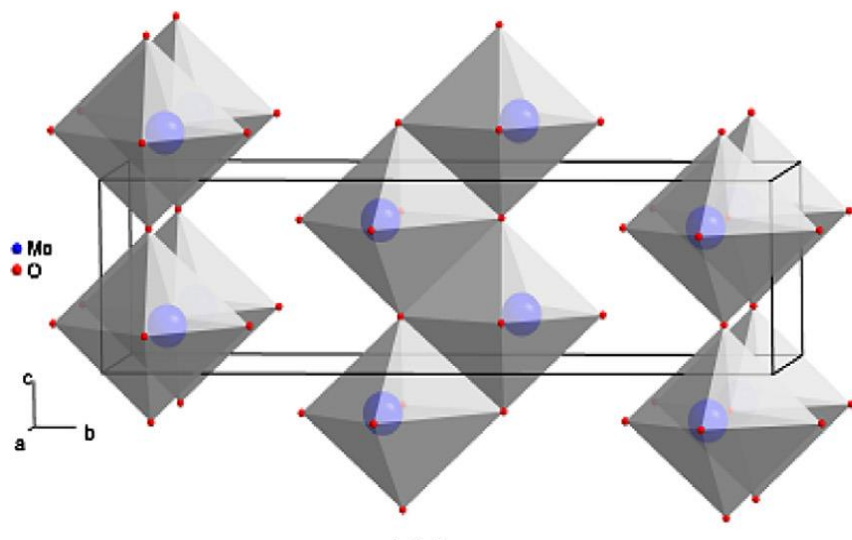
© 2013 Elsevier Inc. All rights reserved.

Selected Examples

Ammonia is an excellent hydrogen carrier (17 wt% H, liquefies at 8-10 bar at RT) and the decomposition of ammonia is considered as a possible method to generate hydrogen for fuel cell applications without formation of CO_x . On the other hand, ammonia can be used directly as feed for solid oxide fuel cells.

The benchmark catalyst for the ammonia decomposition reaction is ruthenium dispersed over carbon nanotubes. Molybdenum-based catalysts are also being studied due to economical advantages.

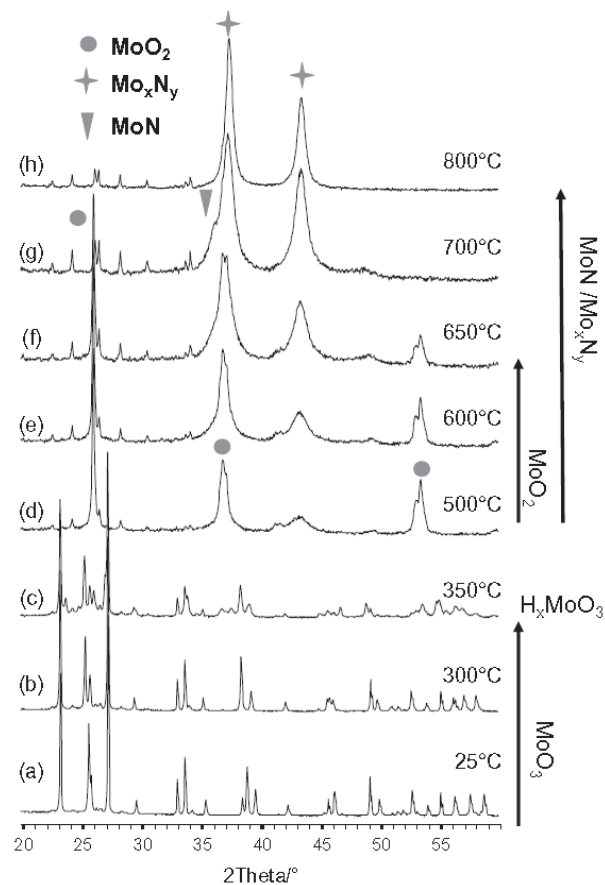
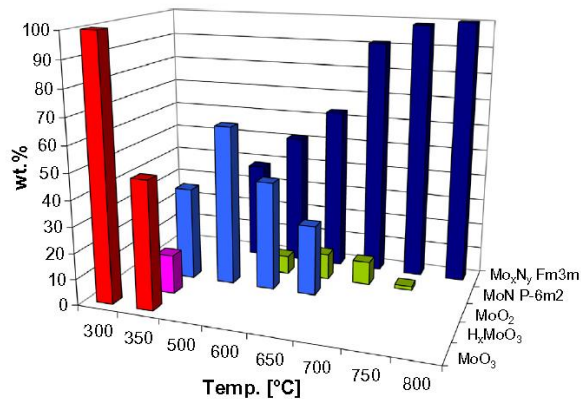
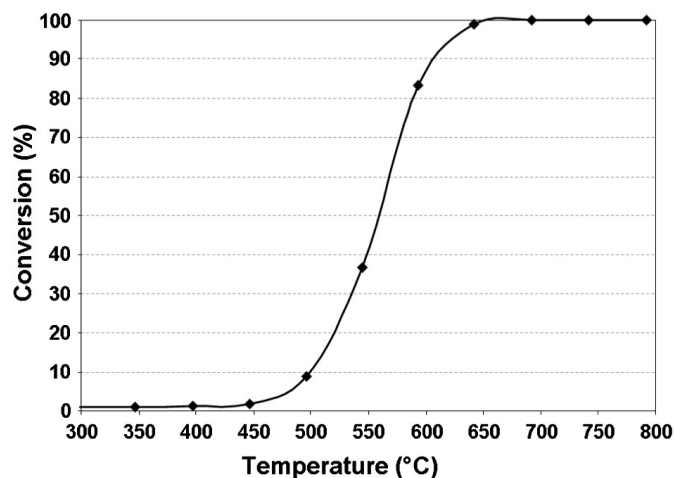
MoO_3 heated in a NH_3 atmosphere can form Mo nitrides, thus triggering the decomposition of ammonia to N_2 and H_2 .



Selected Examples

A catalytic test on a laboratory-prepared sample was run heating up to 800 °C and exposing the catalyst to a stream of ammonia. Complete conversion was achieved at 650 °C.

In situ PXRD showed that the catalyst first undergoes insertion of H₂ with formation of molybdenum bronze (H_xMoO₃), followed by reduction to MoO₂ and concomitant transformation into Mo_xN_y. Quantitative Rietveld refinement was performed, showing that over 650 °C no oxides are present anymore.



Selected Examples

SEM micrographs show that upon nitridation the particle size is strongly reduced and the molybdenum nitride contains a significant amount of porosity. As a consequence, the surface area is significantly increased.

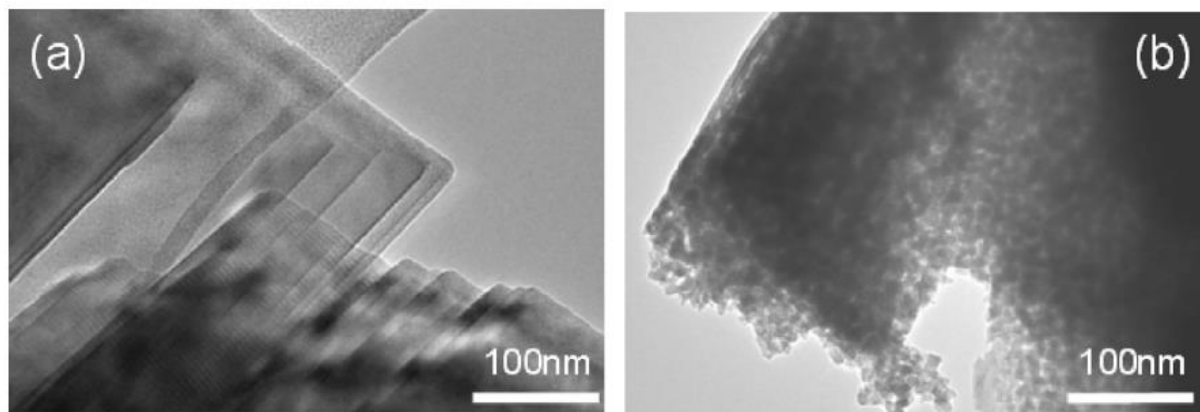


Fig. 10. (a) HTEM images of $\text{MoO}_3\text{-C}$ before catalysis and (b) of Mo_xN_y obtained after catalysis at 800°C .

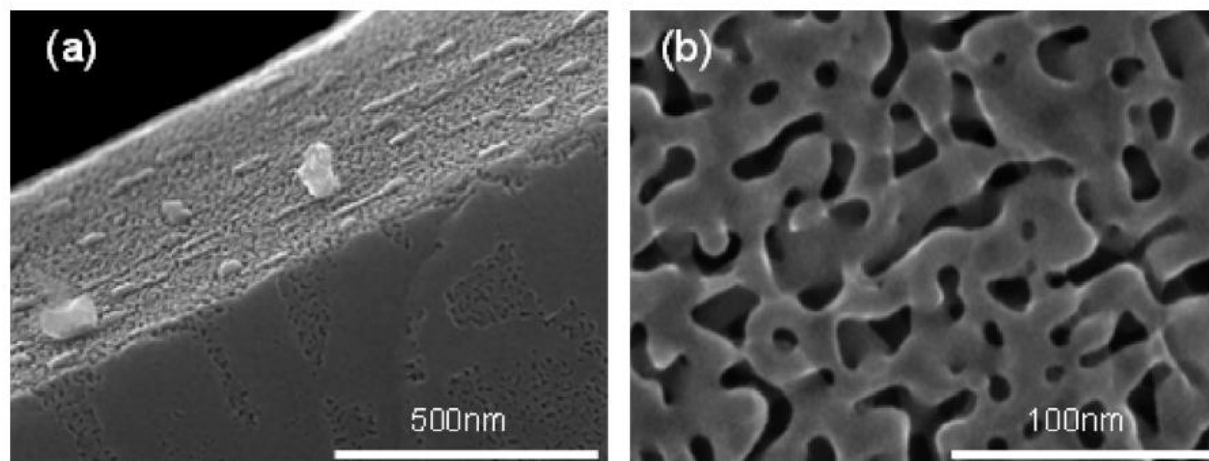
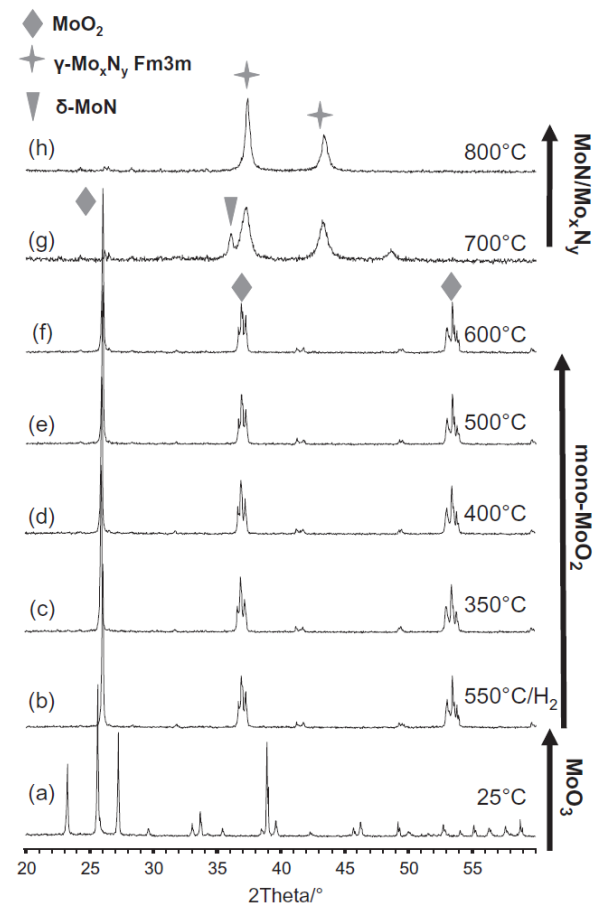
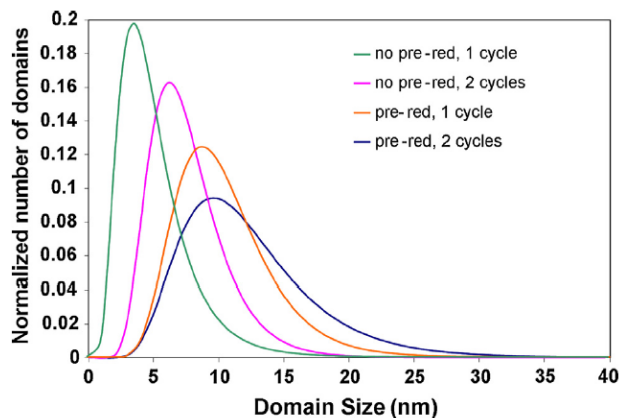
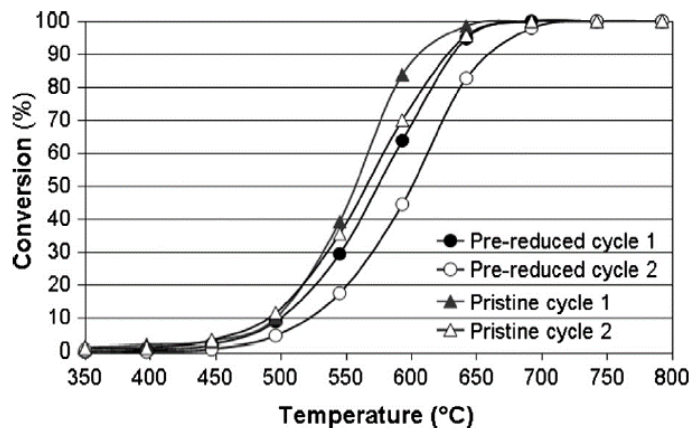


Fig. 11. High-resolution SEM images with different magnifications of molybdenum nitride after catalytic conversion of NH_3 up to 800°C .

Selected Examples

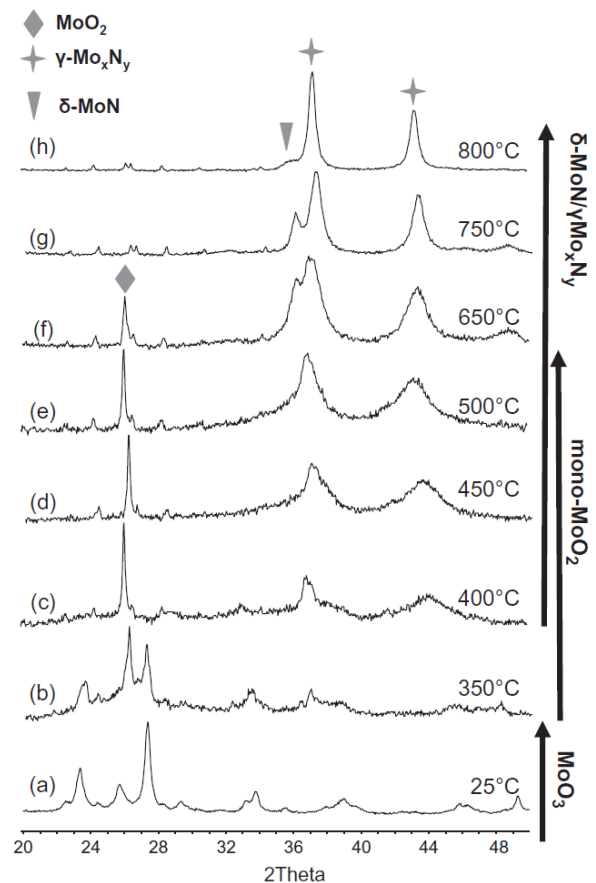
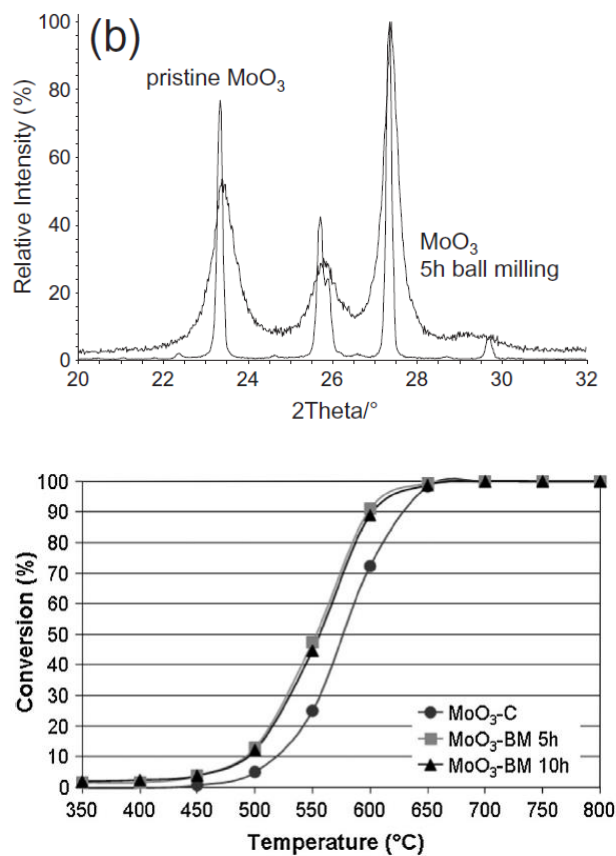
If MoO_3 is pre-reduced to MoO_2 by heating at 550°C under hydrogen, the formation of molybdenum nitrides starts at 700°C . This can be imputed to the larger size of the crystalline domains in this sample than in the pristine one.

The activity of the pre-reduced catalyst was found to be lower than that of the pristine one. Both of them lost activity during a second cycle, probably due to sintering of the crystalline domains.



Selected Examples

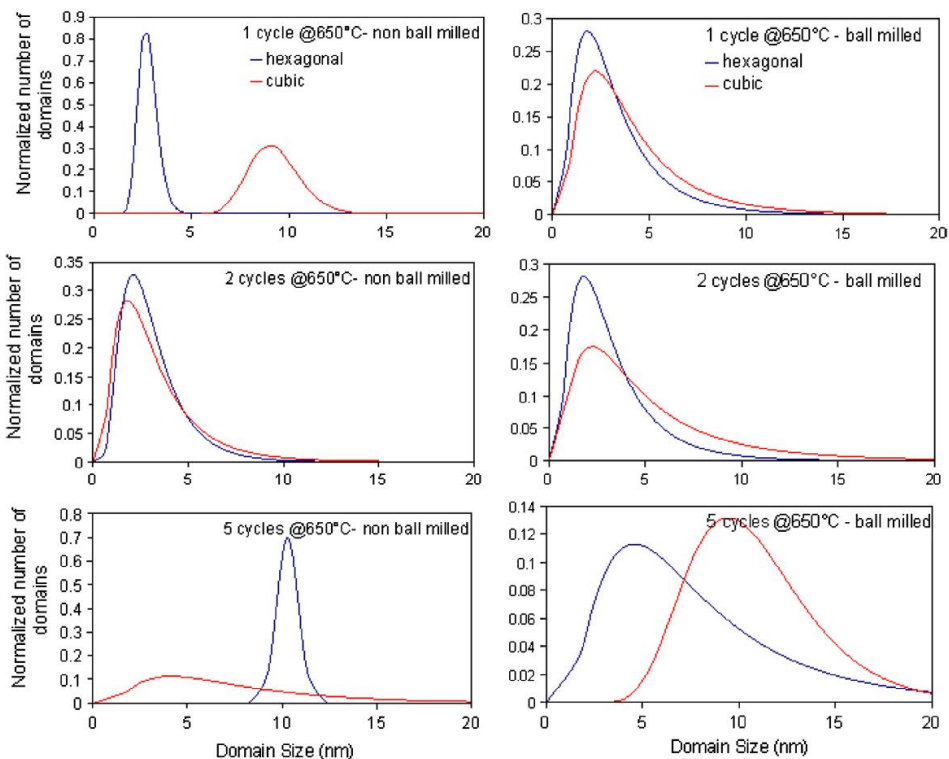
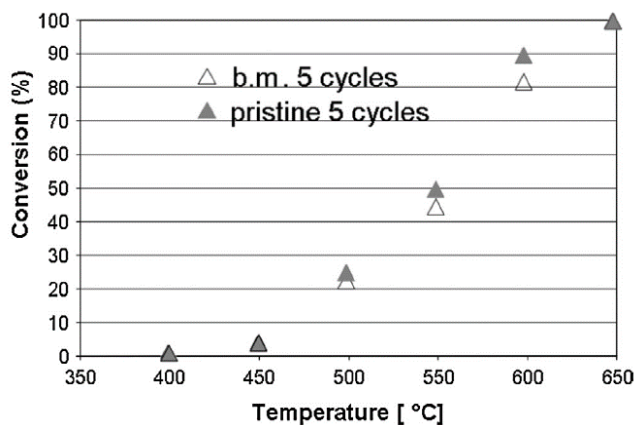
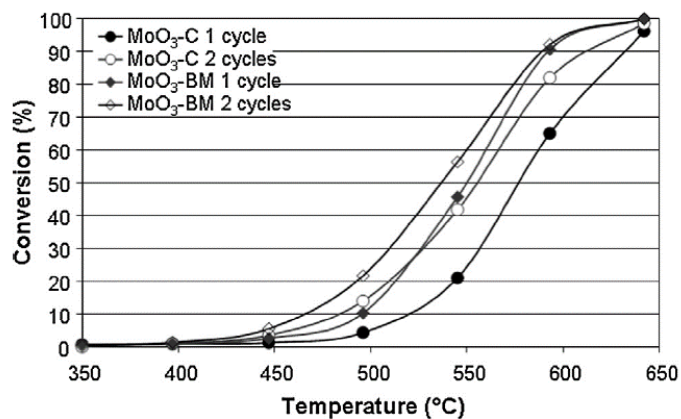
If the catalyst is ball-milled prior to ammonia decomposition, the size of the crystalline domains is decreased and, as a consequence, the catalytic activity is improved.



Selected Examples

Heating up to 650 °C instead that 800 °C, sintering of the particles is reduced and the activity during following cycles is improved. After 5 cycles, the performances of the pristine and the ball-milled catalyst are almost the same.

Analysis of the domain size by means of whole powder pattern modelling (WPPM) shows that sintering slowly occurs when the catalyst works at 650 °C. After 5 cycles, the domain size of the pristine and ball-milled sample are very similar.



Chem. Mater. **2002**, *14*, 2514–2518

Inhibition of the Anatase–Rutile Phase Transformation with Addition of CeO₂ to CuO–TiO₂ System: Raman Spectroscopy, X-ray Diffraction, and Textural Studies

Maria Suzana P. Francisco* and Valmor R. Mastelaro

*Departamento de Física e Ciência dos Materiais, Instituto de Física de São Carlos,
Universidade de São Paulo, P.O. Box 369, 13560-970, São Carlos SP, Brazil*

Received October 29, 2001. Revised Manuscript Received March 5, 2002

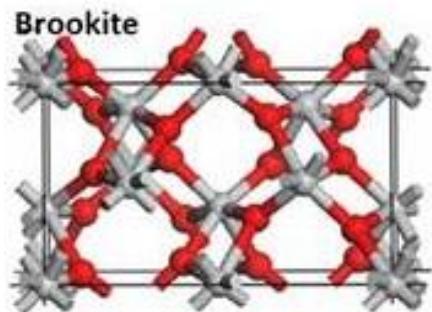
The effect of the addition of CeO₂ on the structural and textural properties of TiO₂ and TiO₂–CuO samples calcined at different temperatures was analyzed. The structural and textural transformation when the temperature of calcination was varied was followed by X-ray diffraction, Raman spectroscopy, and N₂ adsorption techniques. The addition of CeO₂ to the TiO₂ and TiO₂–CuO samples decreases the anatase–rutile phase transformation when compared with the case of pure TiO₂. This decrease observed for the phase transformation prevents the substantial surface loss and pore growth associated with this process.

Selected Examples

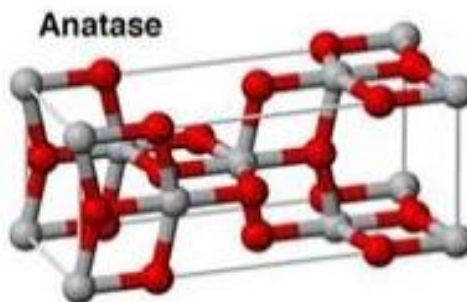
Titania crystallizes in three natural phases: brookite, anatase, and rutile. The brookite and anatase crystalline phases transform into rutile when the sample is calcined at higher temperatures.

It has been demonstrated that some properties of TiO_2 are very sensitive to its structure. Since the anatase phase is chemically and optically active, it is suitable for catalysts and supports. However, it is metastable and tends to transform into the rutile phase, decreasing the surface area and inducing a loss of catalytic activity. The anatase-rutile transformation begins with the nucleation of rutile on anatase and the rutile nuclei grow throughout the anatase particle until completion.

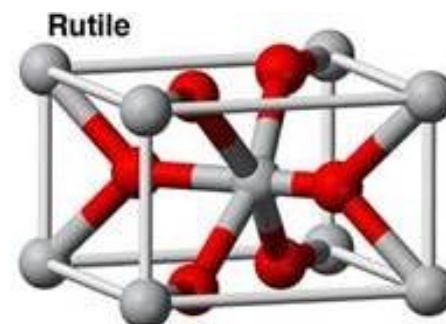
The stabilization of TiO_2 in the anatase phase can usually be achieved by changing its bulk or surface composition, and it is usual to add other atoms to titania in order to improve properties such as structural stability. CeO_2 has the property of stabilizing the active phase in a fine dispersed state and improving the resistance to thermal loss of the supported catalyst surface area and the catalytic activity.



Orthorhombic



Tetragonal



Tetragonal

The behaviour of copper supported on anatase was studied, as it is a widely used catalyst in the industry for selective oxidation of *o*-xylene to phthalic anhydride, steam reforming and methanol dehydrogenation, CO oxidation, NO_x decomposition, and complete mineralization of a variety of volatile organic compounds (VOCs).

After calcination at 450 °C, the Ce-doped catalysts show broadened anatase reflections.

Calcination at 650 °C causes a decrease of 81% and 88% in surface area in the non-ceria doped materials. The ceria-doped materials undergo a decrease of 49%. The presence of Cu promotes the transformation into rutile, whereas in the presence of Ce the anatase structure is preserved.

After calcination at 850 °C all of the materials show surface areas smaller than 8 m²/g. At this temperature, all of the samples contain only rutile.

Table 1. BET Surface Area (S), Pore Size (PS), and the Crystallographic Phases Observed by XRD and Raman Spectroscopy of TiO₂, CuO–TiO₂, and CuO/CeO₂–TiO₂ Samples Calcined at 450 and 650 °C

samples	T = 450 °C			T = 650 °C		
	S/ m ² g ⁻¹	PS/ nm	phase ^a	S/ m ² g ⁻¹	PS/ nm	phase ^a
TiO ₂	79	20.2	a	15		a/r
Ti _{0.91} O _{1.91} Cu _{0.09}	84	35.0	a	10		r, t
Ce _{0.09} Ti _{0.82} O _{1.91} Cu _{0.09}	124	18.4	a, c	61	43.0	a/r, c, t
Ce _{0.27} Ti _{0.64} O _{1.91} Cu _{0.09}	105	18.7	a, c	51	58.1	a/r, c, t

^a (a) anatase and (r) rutile TiO₂ phases; (c) cerianite CeO₂ phase; (t) tenorite CuO phase.

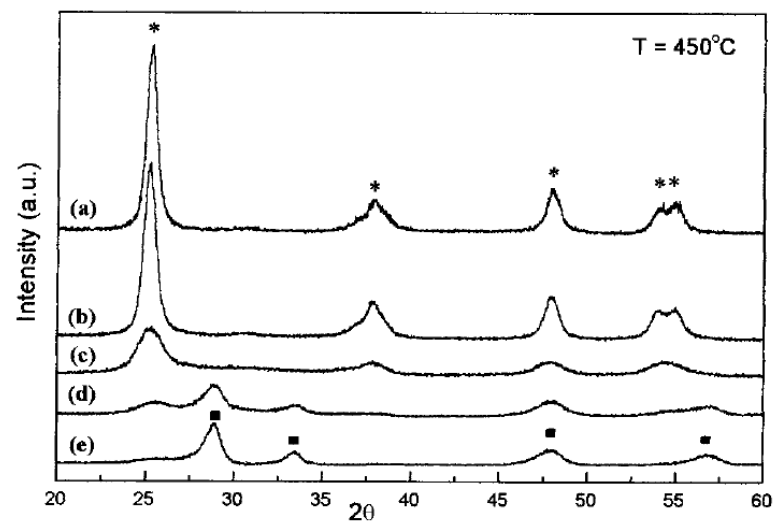


Figure 1. XRD patterns of samples calcined at 450 °C: (a) TiO₂, (b) Ti_{0.91}O_{1.91}Cu_{0.09}, (c) Ce_{0.09}Ti_{0.82}O_{1.91}Cu_{0.09}, and (d) Ce_{0.27}Ti_{0.64}O_{1.91}Cu_{0.09}. (*) fase TiO₂ anatase, (+) fase TiO₂ rutile, (■) fase CeO₂ cerianite.

The behaviour of copper supported on anatase was studied, as it is a widely used catalyst in the industry for selective oxidation of *o*-xylene to phthalic anhydride, steam reforming and methanol dehydrogenation, CO oxidation, NO_x decomposition, and complete mineralization of a variety of volatile organic compounds (VOCs).

After calcination at 450 °C, the Ce-doped catalysts show broadened anatase reflections.

Calcination at 650 °C causes a decrease of 81% and 88% in surface area in the non-ceria doped materials. The ceria-doped materials undergo a decrease of 49%. The presence of Cu promotes the transformation into rutile, whereas in the presence of Ce the anatase structure is preserved.

After calcination at 850 °C all of the materials show surface areas smaller than 8 m²/g. At this temperature, all of the samples contain only rutile.

Table 1. BET Surface Area (S), Pore Size (PS), and the Crystallographic Phases Observed by XRD and Raman Spectroscopy of TiO₂, CuO–TiO₂, and CuO/CeO₂–TiO₂ Samples Calcined at 450 and 650 °C

samples	T = 450 °C			T = 650 °C		
	S/ m ² g ⁻¹	PS/ nm	phase ^a	S/ m ² g ⁻¹	PS/ nm	phase ^a
TiO ₂	79	20.2	a	15		a/r
Ti _{0.91} O _{1.91} Cu _{0.09}	84	35.0	a	10		r, t
Ce _{0.09} Ti _{0.82} O _{1.91} Cu _{0.09}	124	18.4	a, c	61	43.0	a/r, c, t
Ce _{0.27} Ti _{0.64} O _{1.91} Cu _{0.09}	105	18.7	a, c	51	58.1	a/r, c, t

^a (a) anatase and (r) rutile TiO₂ phases; (c) cerianite CeO₂ phase; (t) tenorite CuO phase.

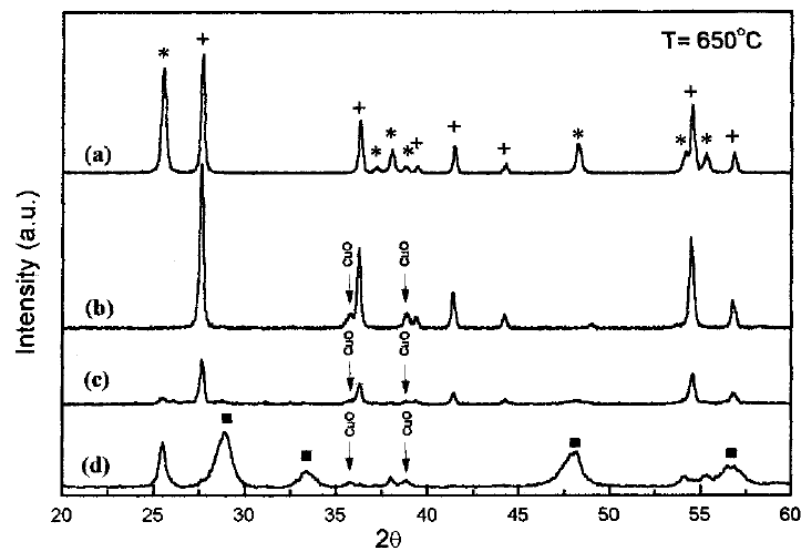


Figure 2. XRD patterns of samples calcined at 650 °C: (a) TiO₂, (b) Ti_{0.91}O_{1.91}Cu_{0.09}, (c) Ce_{0.09}Ti_{0.82}O_{1.91}Cu_{0.09}, and (d) Ce_{0.27}-Ti_{0.64}O_{1.91}Cu_{0.09}. (*) fase TiO₂ anatase, (+) fase TiO₂ rutile, (■) fase CeO₂ cerianite.

The behaviour of copper supported on anatase was studied, as it is a widely used catalyst in the industry for selective oxidation of *o*-xylene to phthalic anhydride, steam reforming and methanol dehydrogenation, CO oxidation, NO_x decomposition, and complete mineralization of a variety of volatile organic compounds (VOCs).

After calcination at 450 °C, the Ce-doped catalysts show broadened anatase reflections.

Calcination at 650 °C causes a decrease of 81% and 88% in surface area in the non-ceria doped materials. The ceria-doped materials undergo a decrease of 49%. The presence of Cu promotes the transformation into rutile, whereas in the presence of Ce the anatase structure is preserved.

After calcination at 850 °C all of the materials show surface areas smaller than 8 m²/g. At this temperature, all of the samples contain only rutile.

Table 1. BET Surface Area (S), Pore Size (PS), and the Crystallographic Phases Observed by XRD and Raman Spectroscopy of TiO₂, CuO–TiO₂, and CuO/CeO₂–TiO₂ Samples Calcined at 450 and 650 °C

samples	T = 450 °C			T = 650 °C		
	S/ m ² g ⁻¹	PS/ nm	phase ^a	S/ m ² g ⁻¹	PS/ nm	phase ^a
TiO ₂	79	20.2	a	15		a/r
Ti _{0.91} O _{1.91} Cu _{0.09}	84	35.0	a	10		r, t
Ce _{0.09} Ti _{0.82} O _{1.91} Cu _{0.09}	124	18.4	a, c	61	43.0	a/r, c, t
Ce _{0.27} Ti _{0.64} O _{1.91} Cu _{0.09}	105	18.7	a, c	51	58.1	a/r, c, t

^a (a) anatase and (r) rutile TiO₂ phases; (c) cerianite CeO₂ phase; (t) tenorite CuO phase.

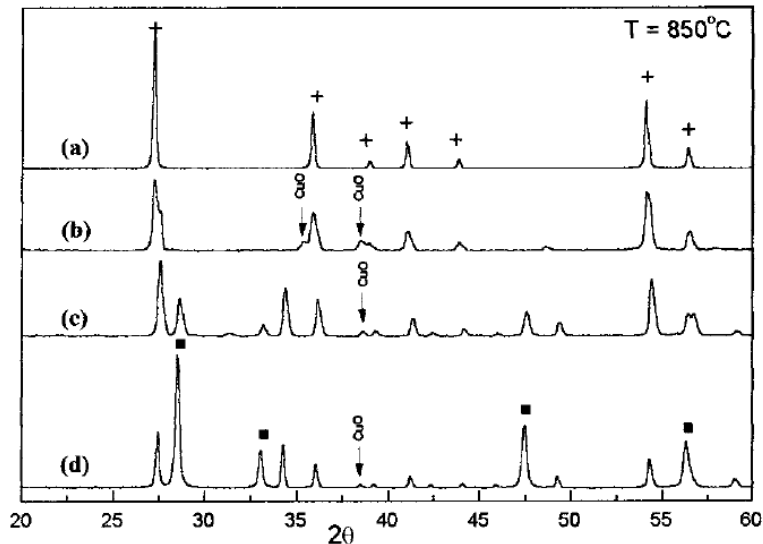


Figure 3. XRD patterns of samples calcined at 850 °C: (a) TiO₂, (b) Ti_{0.91}O_{1.91}Cu_{0.09}, (c) Ce_{0.09}Ti_{0.82}O_{1.91}Cu_{0.09}, and (d) Ce_{0.27}-Ti_{0.64}O_{1.91}Cu_{0.09}. (+) fase TiO₂ rutile, (■) fase CeO₂ cerianite.